Development of fluorescent protein-based indicators
for neuronal activity imaging

by

Ahmed Abdelfattah

A thesis submitted in partial fulfillment of the requirements for the
degree of

Doctor of Philosophy

Department of Chemistry
University of Alberta

Abstract

Fluorescence microscopy is currently the most powerful imaging technique for interrogation of neural circuits. Accordingly, tremendous efforts have been invested in engineering fluorescent proteins (FPs) to act as indicators for various biochemical processes in neural circuits, resulting in a plethora of genetically encoded FP-based indicators for neural imaging. In this thesis, we report the development of various FP-based indicators for neuronal imaging. Specifically, we describe our efforts to expand the current repertoire of neuronal activity indicators to include a voltage indicator with red-shifted fluorescence, a highlightable voltage indicator, and a green fluorescent indicator for the neurotransmitter γ-aminobutyric acid (GABA).

First, we added to the spectral palette of practically useful voltage indicators by developing a bright red-shifted FP-based voltage indicator (FlicR1). Using protein engineering and directed evolution, we engineered FlicR1 to have sufficient speed and sensitivity to report single action potentials in single-trial recordings. Because it is excitable with yellow light, FlicR1 is the first FP-based voltage indicator that can be used in conjunction with blue-light-activated optogenetic actuators to report optically driven action potentials.

Using FlicR1 as a template, we further engineered voltage indicators that utilize two copies of voltage sensitive domains linked in tandem by a circularly permutated FP. This design allowed us to create two new

voltage indicators: a red intensiometric voltage indicator (tdFlicR Δ110AR) and a green/red ratiometric voltage indicator (tdFlicR-VK-ASAP). We demonstrate their utility by imaging membrane potential changes in cultured human cell lines and primary neuron cultures. Furthermore, we engineered a highlightable voltage indicator (FlicGR0.7). FlicGR0.7 can be photoconverted from a green to a red fluorescent form using blue light illumination. We demonstrate that both the green and red fluorescent forms of FlicGR0.7 are sensitive to membrane potential changes in mammalian cells.

Finally, we developed a green FP-based GABA indicator (GABA-G1). Upon binding to GABA, GABA-G1 decreases its green fluorescence. Through rational design and directed protein evolution we engineered GABA-G1 to have a 1-fold dynamic range in vitro. Although we attempted several strategies to target GABA-G1 to the surface of mammalian cells, it remained trapped in the endoplasmic reticulum.

Preface

Chapter 2 has been published as: A. S. Abdelfattah, S. L. Farhi, Y. Zhao, D. Brinks, P. Zou, A. Ruangkittisakul, J. Platisa, V.A. Pieribone, K. Ballanyi, A. E. Cohen, and R. E. Campbell, A bright and fast red fluorescent protein voltage indicator that reports neuronal activity in organotypic brain slices, *J. Neurosci.* **36**, 2458–2472 (2016). I performed rational design, directed evolution, imaging in HeLa cells, dissociated neurons and organotypic slices. Samouil L. Farhi performed patch clamp measurements in HEK cells and cultured neurons. Yongxin Zhao designed the dual expression vector and set up the HeLa cell screening system. Daan Brinks performed two-photon measurements. Peng Zou helped characterize the photophysics of ArcLight. Araya Ruangkittisakul performed rat hippocampus dissection. Jelena Platisa preformed patch clamp measurements in HEK cells of early indicator variants. Robert E. Campbell, Adam E. Cohen, Klaus Ballanyi, and Vincent A. Pieribone directed research. Samouil L. Farhi, Adam E. Cohen, Robert E. Campbell and I wrote the manuscript.

A version of Chapter 3 and Chapter 4 are being prepared to be submitted for publication as: A. S. Abdelfattah, V. Rancic, K. Ballanyi, and R. E. Campbell, Engineering photoconvertible and ratiometric fluorescent protein-based voltage indicators. I performed rational design, directed evolution, and imaging in HeLa cells and dissociated neurons. Vladimir

Rancic and I performed patch clamp measurements in HEK cells. Robert E. Campbell and Klaus Ballanyi directed research.

Undergraduate researchers Yiqun Wang and Fahim Rahman helped perform several directed evolution rounds and screening for the GABA indicator described in Chapter 5.

During my PhD I was involved in several other projects not described in this thesis that culminated in the following publications:

1) Y. Zhao, S. Araki, J. Wu, T. Teramoto, Y-F. Chang, M. Nakano, A. S. Abdelfattah, M. Fujiwara, T. Ishihara, T. Nagai, and R. E. Campbell, An expanded palette of genetically encoded Ca^{2+} indicators. *Science 333*, 1888–1891 (2011). I performed the structural models for the GECO variants using Rosetta molecular modeling software.

2) S. C. Alford, A. S. Abdelfattah, Y. Ding, and R. E. Campbell, A fluorogenic red fluorescent protein heterodimer. *Chem Biol 19*, 353–360 (2012). I performed the homology model for ddRFP using Rosetta molecular modeling software.

3) Y. Zhao, A. S. Abdelfattah, Y. Zhao, A. Ruangkittisakul, K. Ballanyi, R. E. Campbell, and D. J. Harrison DJ, Microfluidic cell sorter-aided directed evolution of a protein-based calcium ion indicator with an inverted fluorescent response. *Integr Biol (Camb) 6,* 714–725 (2014). I performed culture, electroporation, field stimulation and confocal imaging of organotypic brain slices.

4) J. Wu, A. S. Abdelfattah, L. S. Miraucourt, E. Kutsarova, A. Ruangkittisakul, H. Zhou, K. Ballanyi, G. Wicks, M. Drobizhev, A. Rebane, E. S. Ruthazer, and R. E. Campbell, A long Stokes shift red fluorescent Ca^{2+} indicator protein for two-photon and ratiometric imaging. *Nat Commun* **5**, 5262 (2014). I performed culture, electroporation, field stimulation, one-photon and two-photon imaging of organotypic brain slices.

Table of Contents

List of Figures

List of Tables

List of Abbreviations

Å	Angstrom
Asp	Aspartate
ATP	Adenosine triphosphate
Arg	Arginine
BFP	Blue fluorescent protein
BiFC	Bimolecular fluorescence complementation
CiVSD	*Ciona intestinalis* voltage sensing domain
CMV	Cytomegalovirus
cpFP	Circularly permutated fluorescent protein
DMEM	Dulbecco's modified eagle media
DNA	Deoxyribonucleic acid
dNTPs	Deoxynucleotide triphosphates
DsRed	*Discosoma sp*. Red fluorescent protein
EBFP	Enhanced blue fluorescent protein
ECFP	Enhanced cyan fluorescent protein
EGFP	Enhanced green fluorescent protein
E. coli	*Escherichia coli*
FlicR	Fluorescent indicator for voltage imaging red
FlicGR	Fluorescent indicator for voltage imaging green to red
FP	Fluorescent protein
FRET	Förster resonance energy transfer

GABA	γ-Aminobutyric acid
GgVSD	*Gallus gallus* voltage sensing domain
GFP	Green fluorescent protein
GECO	Genetically encoded Ca^{2+} indicators for optical imaging
Gly	Glycine
Gln	Glutamine
Glu	Glutamate
His	Histidine
ITV	Induced transmembrane voltage
kDa	Kilodalton
Leu	Leucine
μg	Microgram
μM	Micromolar
ml	Milliliter
ms	Millisecond
nm	Nanometer
nM	Nanomolar
PBP	Periplasmic binding protein
PCR	Polymerase chain reaction
Phe	Phenylalanine
RFP	Red fluorescent protein
RNA	Ribonucleic acid
rmsd	Root mean square deviation

SASA	Solvent accessible surface area
sec	second
Ser	Serine
StEP	Staggered extension process
Thr	Threonine
Tyr	Tyrosine
VSD	Voltage sensing domain
λ_{ex}	Wavelength of maximal excitation

Chapter 1 Introduction

1.1 Overview

The human brain has approximately 80 billion neurons (*1*) that are organized into elaborate circuits that form the basis of sensory integration, motor coordination, and higher brain functions. As these neuronal circuits are made up of numerous spatially dispersed neurons, simultaneous recording of activity from many locations is key to understanding how brain function emerges from these circuits (*2*, *3*). At the cellular level, brain activity can be recorded by measuring membrane potential, calcium ion (Ca^{2+}) concentration, or neurotransmitter release. Towards the goal of recording brain activity, small-molecule organic dyes with fluorescent signals that change in response to changes in the membrane potential (*4*) or Ca^{2+} concentration (*5*, *6*), have been used over the past four decades to image neuronal activity. A drawback of organic dyes is that bath application typically leads to a summed signal from many stained cells and spatial resolution is lost. Neurotransmitter release has been historically determined by *in situ* microdialysis (*7–10*), however, spatial and temporal resolution is low with this conventional method.

Fluorescence imaging of fluorescent protein (FP)-based indicators provides improved spatial and temporal resolution relative to traditional methods. FPs are unique amongst all proteins as they possess the remarkable ability to form a visible wavelength fluorophore from their own

amino acid sequence. Moreover FPs can be engineered to act as readouts for specific biochemical process through process-dependent changes in their optical signal. Because they are fully genetically encoded, they can be easily targeted to specific cellular populations and subcellular compartments and can be delivered to cells of interest by relatively non-invasive methods like viral infection or transgenesis. This feature of FP-based indicators enables them to be used for *in vivo* monitoring of dynamic brain activity by fluorescence microscopy. Many examples of FP-based indicators have been engineered, including FP-based indicators for Ca^{2+} (*11–13*), voltage (*14*, *15*), and glutamate (*16*, *17*).

In the remainder of this introductory chapter, I will provide a general overview of FPs and their use to engineer genetically encoded fluorescent indicators for live cell imaging. We will briefly examine the properties of several members of the FP family that are commonly used for live cell imaging. This will be followed by an introduction to the general design principles used to construct FP-based indicators for studying dynamic signaling processes in living cells and the challenges of using them to study neuronal activity.

1.2 Fluorescent proteins

1.2.1 Discovery and colour variants

Green FP (GFP) was isolated from tissue extracts of the jellyfish *Aequorea victoria* by Osamu Shimomura in 1962 (*18*). At the time, GFP

was isolated as a by-product during the purification of the luminescent protein, aequorin. Initially, Dr. Shimomura was interested to study and understand the bioluminescence of jellyfish and therefore was more interested in aequorin. It was three decades later, in 1992, that the GFP gene was first cloned and the amino acid sequence determined by Douglas Prasher (*19*). This breakthrough enabled the recombinant expression of GFP in *E. coli* and *C. elegans* by Chalfie *et al.* (*20*) which was a stepping stone to prove that no other component of *Aequorea victoria* is needed to convert the GFP polypeptide chain into a functional FP. Later the same year, Roger Y. Tsien and coworkers were able to show that the strongly fluorescent chromophore, 4-(*p*-hydroxybenzylidene)-5-imidazolinone, forms autocatalytically from the tripeptide Ser-Tyr-Gly that is part of the GFP amino acid sequence (*21*). This was a remarkable finding because this meant that GFP could be used as a genetically encoded fluorescence marker requiring no additional cofactors in essentially all organisms.

These findings prompted researchers across many scientific disciplines to search for GFP homologues with new properties in other organisms. These efforts led to the identification of FP variants from non-bioluminescent reef coral and anemone (*22*). This discovery revealed that FPs do not have to be linked with bioluminescence in nature. Since then, many different GFP homologues have been identified with novel properties and colours ranging from blue to red. As a result of decades of

work, we now have a toolbox of FPs, with a wide range of spectroscopic properties, that have revolutionized the field of fluorescence imaging.

1.2.2 Amino acid sequence and the three dimensional structure of FPs

The sequencing of the *Aequorea victoria* GFP gene showed that the protein consists of 238 amino acids (Figure 1-1) and has a calculated molecular mass of ~26.9 kDa (*19*). A key feature in the sequence is the tripeptide Ser65-Tyr66-Gly67 that, in the presence of oxygen, autocatalytically forms the intrinsic chromophore of GFP. Because the chromophore is formed autocatalytically from the protein sequence that is transcribed and translated from the DNA (via mRNA), the FP gene can be easily manipulated using molecular biology tools to genetically label recombinant fusion proteins. In contrast to the more traditional labeling of proteins with synthetic fluorophores, which would typically need to be performed in vitro and then injected back into cells, GFP and its homologues enable relatively non-invasive fluorescent labeling of almost any protein in a living organism.

Four highly conserved residues that are essential for chromophore formation are Tyr66, Gly67, Arg96 and Glu222 (*23*). Although substitutions can be tolerated at most of those positions and lead to different colour variants, Gly67 is strictly conserved (*24*, *25*). GFP structural homologues, specifically red-shifted variants from reef coral and anemone, share little sequence homology with GFP. For example, one of the well-known red

colour homologues of GFP, DsRed from *Discosoma* coral (*22*), forms a red-shifted chromophore from the Glu65-Tyr66-Gly67 tripeptide and overall only shares ~20% sequence similarity with GFP (Figure 1-1).

```
GFP    MSKGEELFTGVVPILVELDGDVNGHKFSVSGEGEGDATYG  40
DsRed  MRSSKNVIKEFMRFKVRMEGTVNGHEFEIEGEGEGRPYEG  40

GFP    KLTLKFIC-TTGKLPVPWPTLVTTFSYGVQCFSRYPDHMK  79
DsRed  HNTVKLKVTKGGPLPFAWDILSPQFQYGSKVYVKHPADI-  79

GFP    QHDFFKSAMPEGYVQERTIFFKDDGNYKTRAEVKFEGDTL  119
DsRed  -PDYKKLSFPEGFKWERVMNFEDGGVVTVTQDSSLQDGCF  118

GFP    VNRIELKGIDFKEDGNILGHKL-EYNYNSHNVYIMADKQK  158
DsRed  IYKVKFIGVNFPSDGPVMQKKTMGWEASTERLYPRDGVLK  158

GFP    NGIKVNFKIRHNIEDGSVQLADHYQQNTPIGDGPVLLPDN  198
DsRed  GEIHKALK----LKDGGHYLVEF--KSIYMAKKPVQLPGY  192

GFP    HYLSTQSALSKDPNEKRDHMVLLEFVTAAGITHGMDELYK  238
DsRed  YYVDSKLDITS---HNEDYTIVEQYERTEGRHH----LFL  225
```

Figure 1-1 Alignment of the sequence of GFP and DsRed. Conserved amino acids are highlighted in black and similar amino acids are shaded in grey. Chromophore forming residues are boxed. Dashes indicate gaps in the alignment. Amino acid sequences aligned using Clustal Omega (*26, 27*)

The three dimensional structure of FPs is key to understanding their unique fluorogenic property. All FPs fold into a cylinder structure, also known as a β-barrel (*28*) or β-can (*29*) (Figure 1-2A). The β-barrel consists of 11 β-strands, with a central α-helix that runs through the centre of the cylinder (Figure 1-2A and B). The α-helix contains the tripeptide that forms the chromophore in the mature FP. The chromophore is buried almost

perfectly in the center of the β-barrel (Figure 1-2A and B). The surrounding protein structure protects the chromophore from the environment and is essential for the chromophore to fluoresce. If the chromophore is exposed to the external environment, non-radiative relaxation becomes predominant and the chromophore is essentially non-fluorescent. Rigidly held inside the protein, the chromophore instead relaxes radiatively with the emission of a lower energy photon. Even though different FPs from different organisms (e.g., *Aequorea victoria* GFP and *Discosoma sp*. DsRed) only share 20%-30% sequence similarity, they share very similar three dimensional structures with their backbone α-carbons superimposing to 1.0 Å rmsd (*30*) (Figure 1-2C).
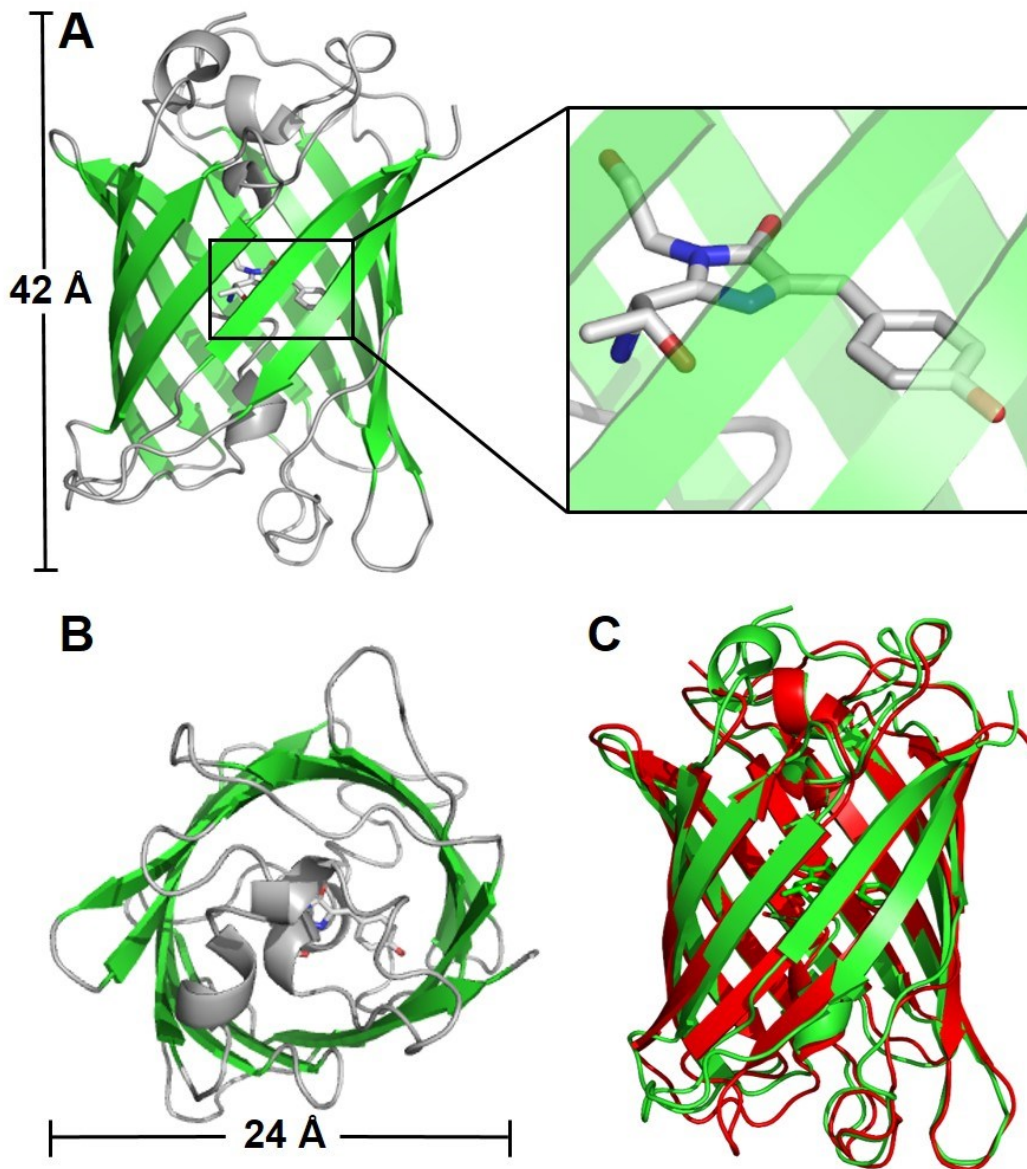
Figure 1-2 Structure of FPs. (A) Right: Cartoon representation of the crystal structure of Ser65Thr variant of GFP (PDB ID: 1EMA). The chromophore is shown as sticks. The protein forms a cylinder (β-barrel) consisting of 11 β-strands and a central α-helix. The cylinder is 42 Å long and has a diameter of 24 Å. Left: Zoom in on the chromophore, the β-barrel is rendered transparent green. (B) Top view of the same cartoon representation in (A). (C) Superimposition of GFP (PDB ID: 1EMA) and

DsRed (PDB ID: 1GGX) crystal structures. All representations are prepared using PyMol (*31*).

1.2.3 Chromophores of FPs and their formation

The myriad of FP variants, both naturally occurring and engineered in laboratories, have fluorescence emission profiles that span almost the entire visible spectrum of light (*32–34*). The key component that is responsible for the fascinating autofluorescent property of FPs is its chromophore. The two most important spectral properties of the chromophore, its absorption and emission profiles, are controlled by two factors. The first factor is the cumulative influence of the residues forming the local environment around the chromophore. Mutations of these residues can result in changing the local charge, hydrogen bond networks or hydrophobic interactions. This sort of change generally results in relatively small spectral shifts in the absorption and emission of the chromophore. The second and more important factor is the covalent structure of the chromophore and the corresponding extent of π-orbital conjugation contained within the chromophore.

All naturally occurring FPs discovered so far have an X65-Tyr66-Gly67 sequence as the tripeptide that forms the chromophore, where X65 can be almost any amino acid. Gly67 is strictly conserved probably because of its higher degree of conformational freedom is essential during chromophore formation (*24*). On the other hand, Tyr66 is not essential as

substitution with other aromatic residues still leads to mature chromophore biosynthesis and results in different colour variants.

The process of GFP chromophore (and GFP-like chromophore) formation from the tripeptide sequence is spontaneous only inside a folded β-barrel protein structure where it is protected from the external environment and positioned in the proper conformation (*35*). With the exception of molecular oxygen, the FP sequence contains all the functionalities needed to form the chromophore. The four key steps needed are: (1) Proper orientation of the chromophore forming residues, (2) Cyclization, (3) Oxidation, and (4) Dehydration. Historically, the precise order of steps (3) and (4) has been an open question due to conflicting results (*36–41*). A fairly recent comprehensive mechanistic study of the mechanism of red chromophore formation in DsRed FP (*42*), and kinetic isotope effect studies on GFP (*43*), provide strong support for a mechanism in which oxidation precedes dehydration (Figure 1-3).
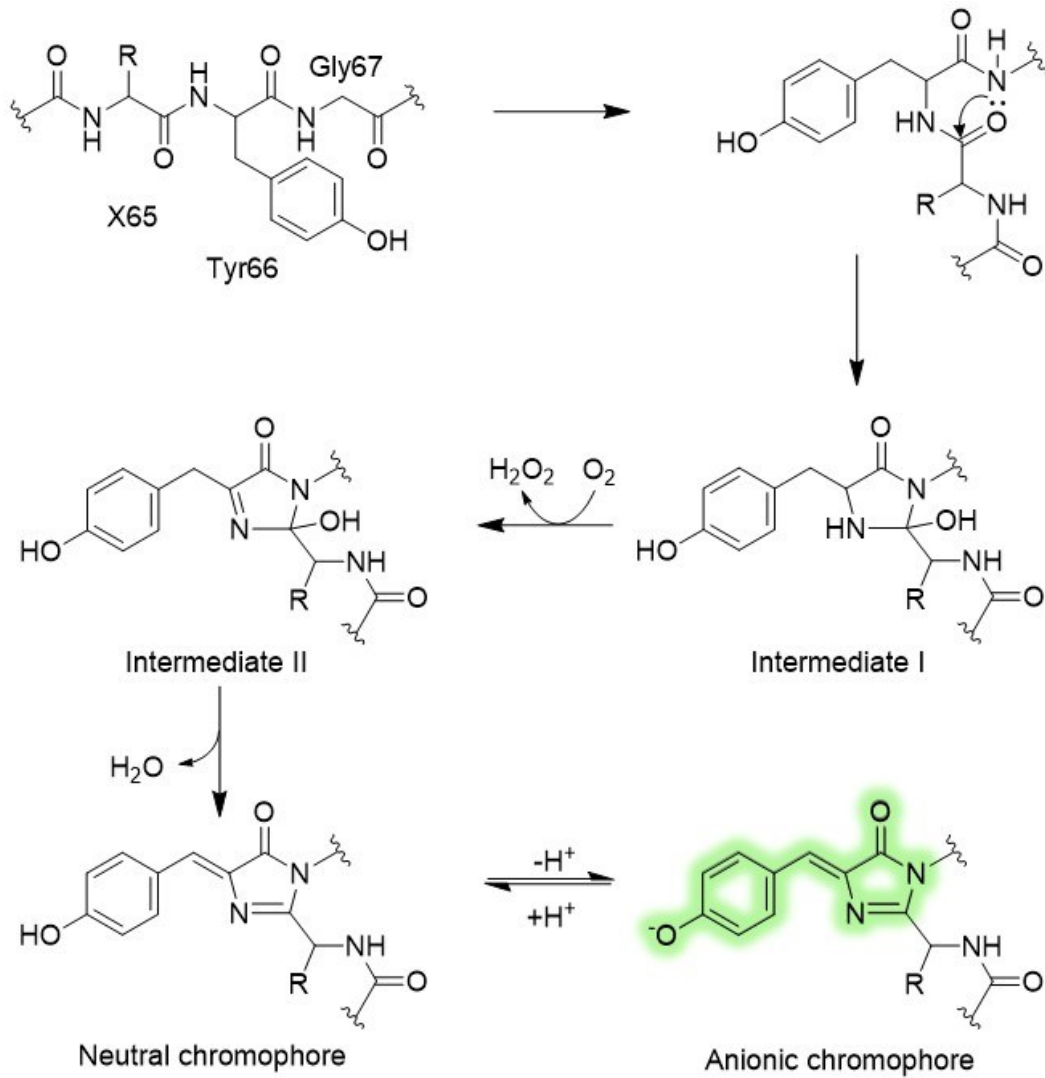
Figure 1-3 Mechanism for chromophore formation in GFP. The four steps needed are proper protein folding followed by cyclization then oxidation and finally dehydration. Wavy lines are points of attachment to the rest of the protein.

The first step to form the GFP chromophore is the proper orientation of the backbone. For this, there is a dramatic ~80° bend in the central helix at Gly67 (*44*), which orients the amide nitrogen and Ser65 carbonyl oxygen within van der Waals contact (*44*). In addition, this α-helix bend

abolishes potential backbone hydrogen bonds that would raise the energy barrier for cyclization (*44*). Subsequently the amide nitrogen of Gly67 attacks the Ser65 carbonyl carbon forming a five membered ring (intermediate I). This cyclization is reversible (*39, 44*) but is trapped by oxidation into a hydroxylated cyclic imine (intermediate II). Dehydration of intermediate II puts the imidazolinone ring in conjugation with the phenol ring from Tyr66 and forms the mature chromophore. Reversible deprotonation forms the fluorescent anionic form (*42*).

Red FPs (RFPs) are naturally found in corals and have a GFP-like chromophore that undergoes an additional oxidation to form an acylimine. This modification extends the π conjugation and results in red-shifted fluorescence. Initially, it was proposed that the mature green chromophore was the precursor to form the red chromophore (*45–47*). This was supported by monitoring the fluorescence of DsRed during maturation which showed the disappearance of a green peak as the red peak increased (*45*). Later reports however showed that intramolecular Förster resonance energy transfer (FRET) was responsible (*48*) because of the tetrameric nature of DsRed. Studying the absorption spectra during the maturation of DsRed, green chromophore formation was found to increase and not decrease as thought earlier (*48*). Another blue species was observed in the absorption spectra study that did decrease during maturation of DsRed and was later identified to be an acylimine conjugated to the heterocycle ring of the chromophore (*49*) (Figure 1-4).

11
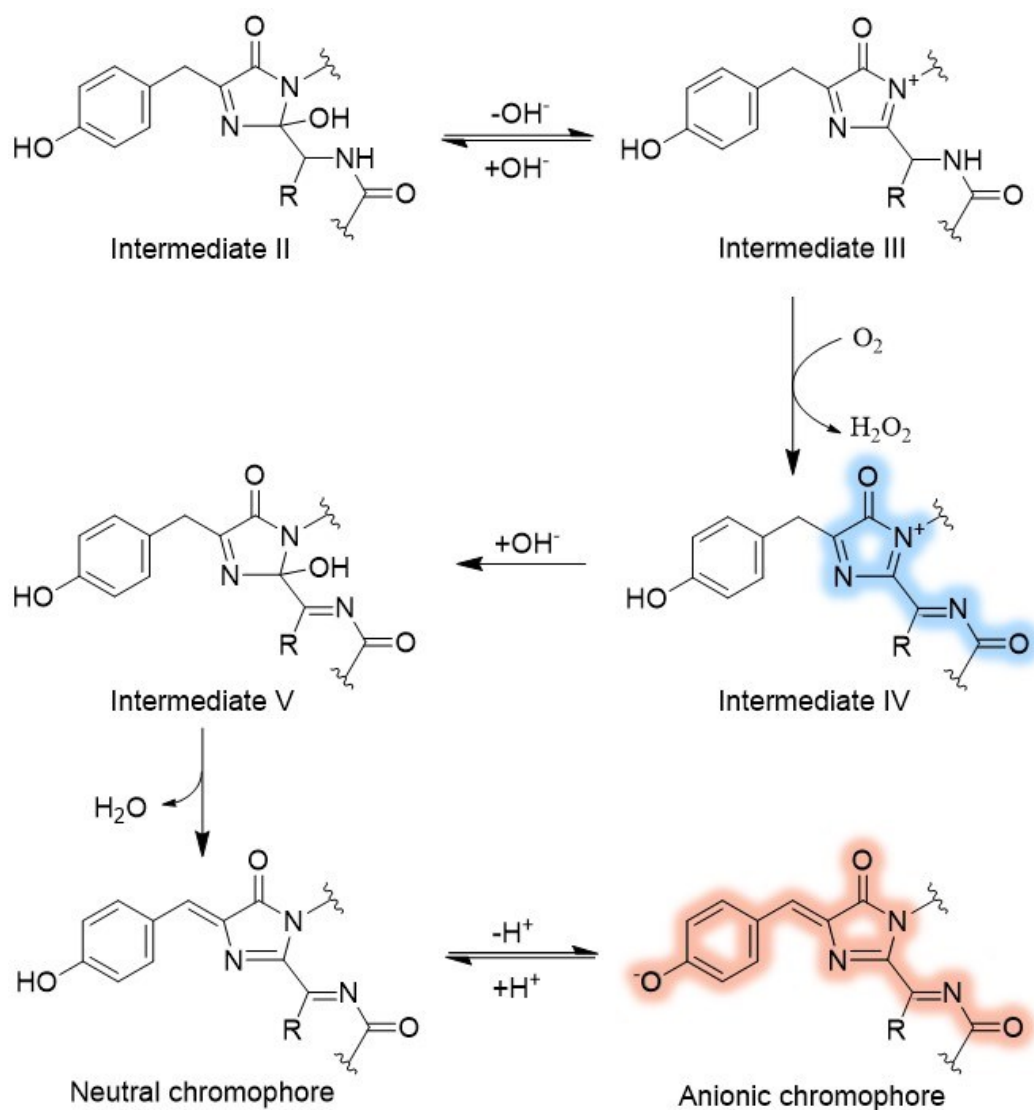
Figure 1-4 Mechanism for chromophore formation in DsRed. A branch point occurs in the GFP chromophore formation pathway at intermediate II (in Figure 1-3), which is in equilibrium with a cyclic imine. A second oxidation step leads to the formation of a blue fluorescent intermediate. Subsequent hydroxylation and dehydration yield the red fluorescent chromophore. Wavy lines are points of attachment to the rest of the protein.

The current accepted mechanism for DsRed chromophore formation reconciles all observations from previous studies (Figure 1-4). In this mechanism, DsRed chromophore formation begins with the GFP pathway, however a branch point occurs at the hydroxylated cyclic imine (intermediate II from Figure 1-3). Intermediate II is in rapid equilibrium with a cyclic imine (intermediate III). A second oxidation generates a conjugated species (intermediate IV, which accounts for the observed blue fluorescence). This is followed by an irreversible hydroxylation (intermediate V) and dehydration of the blue species to form the neutral form of the mature DsRed chromophore. Reversible deprotonation forms the red fluorescent anionic form.

Yet another class of naturally occurring FP chromophores irreversibly change their emission wavelength from green to red upon irradiation with ~400 nm light. These are commonly referred to as Kaede-like chromophores named after Kaede FP (*50*, *51*). As a digression, kaede is the Japanese word for "maple leaf". Similar to the RFPs, Kaede-like FPs are naturally found in corals. Examples of this class include Kaede FP, EosFP (*52*), dendFP (*53*) and mcavRFP (*54*). The chromophore forming tripeptide His-Tyr-Gly is conserved in all Kaede-like FPs. Mutagenesis studies have confirmed that histidine at the first position of the tripeptide is required but not sufficient for photoconversion (*50*). A photoinduced β-elimination reaction causes main chain cleavage between the His amide nitrogen and the α−carbon bond, subsequently extending the π-

conjugated system of the green chromophore to the imidazole ring of histidine and creating a new red chromophore (Figure 1-5). This reaction occurs when exciting the neutral form of the green chromophore. Excitation of the fluorescent anionic form does not result in photoconversion and instead results in green fluorescence as is observed with other GFPs.
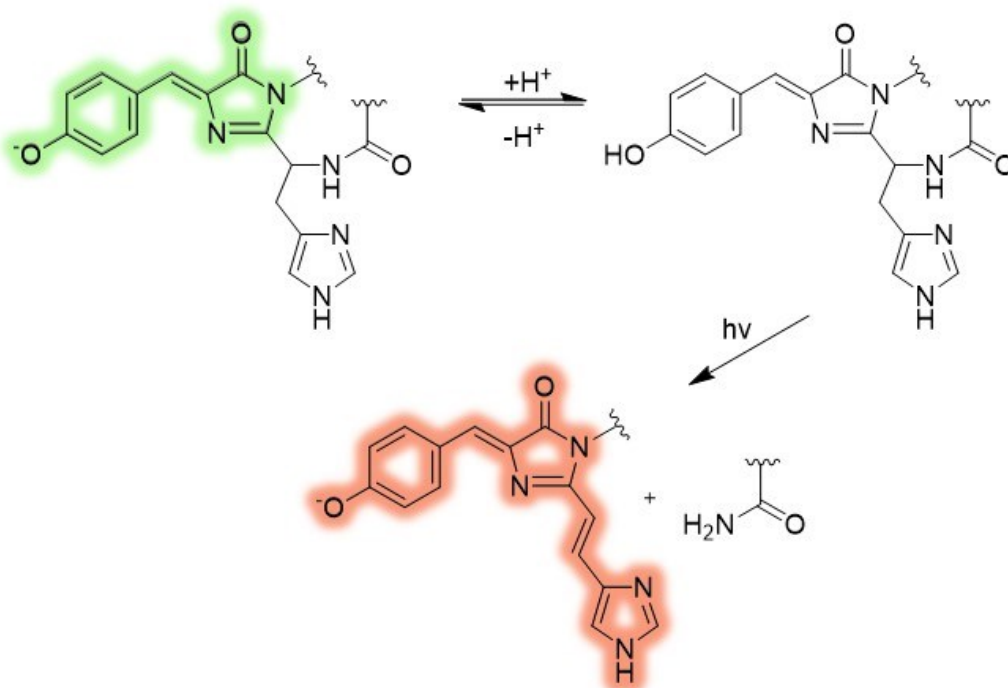
Figure 1-5 Light induced irreversible change in emission wavelength of a Kaede-like chromophore. Upon irradiation with UV light, the protonated form of the chromophore undergoes a β-elimination reaction to form the red fluorescent species.

1.2.4 Protein engineering to address practical limitations of FPs

The unprecedented genetically encoded fluorescence associated with GFP-like chromophores provides a powerful tool for biological

fluorescence imaging. Although the discovery of natural FPs opened new avenues for fluorescence imaging, it remained limited by the practical limitations of the naturally occurring proteins. Those limitations arose because FPs evolved to express and function in marine organisms which live at relatively cool temperatures and ambient light levels. Some of the practical limitations that hampered FPs have been addressed by researchers, leading to improved FPs that are better suited for fluorescence imaging applications. Because FPs are genetically encoded, they can be manipulated using molecular biology techniques to introduce amino acid mutations and subjected to laboratory directed evolution for desirable properties. Arguably, the evolution of FPs in laboratories over the past two decades provides us with the most exquisite example of the beauty of protein engineering and how amenable proteins are to fulfill desired properties; it is just a matter of exploring the right protein space.

1.2.4.1 Engineering for desired spectral properties:

The wild type *Aequorea victoria* GFP had several major drawbacks that reduced its effectiveness as a tool for fluorescence imaging. One of those drawbacks was the fact that it had two separate excitation peaks due to the coexistence of both the neutral (wavelength of maximal excitation (λ_{ex}) ~395 nm) and phenolate (λ_{ex} ~490 nm) forms of the chromophore (*21*). In fact the more prominent form present was the neutral form (~85% compared to the anionic form). The red shifted anionic form (λ_{ex} ~490 nm) requires lower energy light to excite, which is less toxic

to cells and more attractive for fluorescence imaging. To shift the equilibrium towards the anionic form, a single point mutation Ser65Thr was needed (*55*). This variant had a single excitation peak at ~490 nm which resulted in a 6-fold increase in brightness (for the same amount of protein) compared to the wild type (*55*).

Structural analysis later revealed that in wild type GFP, Ser65 donates a hydrogen bond to the carboxyl group of Glu222 and promotes its deprotonation. An electrostatic clash prevents both the Glu222 and the chromophore having a negative charge in close proximity in the FP barrel and therefore the neutral form of the chromophore is stabilized. On the other hand, the Ser65Thr mutation resulted in disruption of the hydrogen bonding with Glu222. This prevented ionization of the carboxylate group of Glu222, therefore removing the electrostatic clash and stabilizing the anionic form of the chromophore (*24*, *56*, *57*).

In addition to engineering wild type GFP to have a single more favourable excitation peak, site-directed and random mutagenesis of amino acid residues has resulted in a myriad of GFP variants with colours ranging from the blue to the yellow regions of the visible spectrum. Because the conjugated structure of the chromophore gives rise to the FP fluorescence, modifying the chromophore forming residues can lead to a change in colour. Indeed, mutating Tyr66 in GFP to other aromatic residues produced blue shifted FPs (Figure 1-6). Replacement with phenylalanine, histidine or tryptophan led to a blue shift in excitation and

emission spectra of the parent GFP chromophore to form ultramarine, blue and cyan variants respectively. These proteins later served as progenitors for engineering bright and photostable FPs useful for fluorescence imaging, namely Sirius (Phe66-based chromophore) (*58*), EBFP2 (His66 based chromophore) (*59*), ECFP (*37*), Cerulean (*60*), and CyPet (Trp66 based chromophore) (*61*).
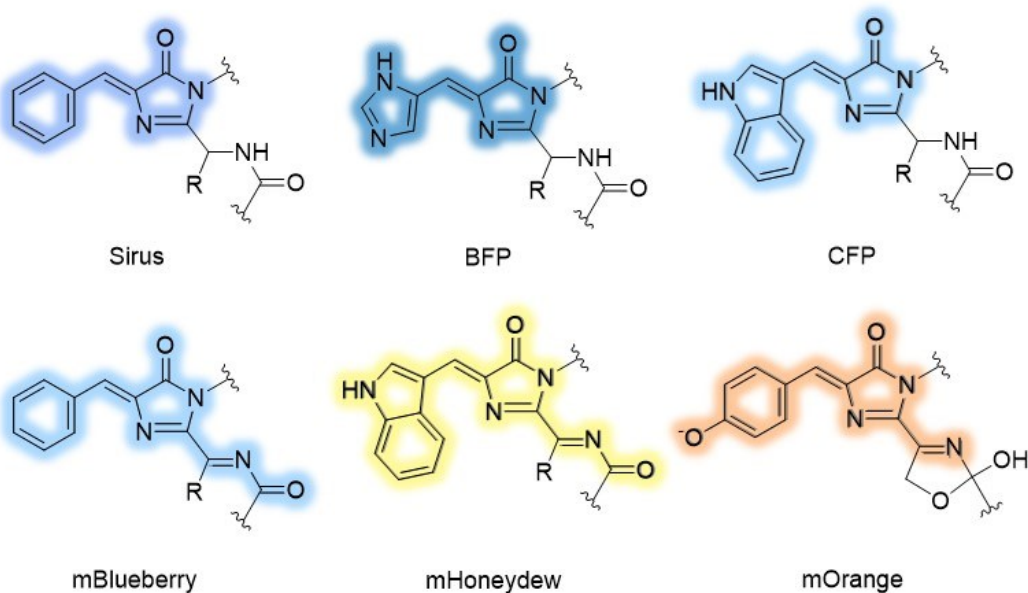
Figure 1-6 Chemical structures of engineered FP chromophores. Top row structures are modified GFP chromophores by mutating Tyr66 into other aromatic residues. Bottom row structures are modified RFP chromophores by either mutating Tyr66 into other aromatic residues (mBlueberry and mHoneydew) or Glu65Thr mutation (mOrange).

The replacement of Tyr66 in other FPs derived from corals also gave rise to FPs with modified spectra (Figure 1-6). For example, mutating Tyr66 in mCherry to a phenylalanine led to a blue variant, mBlueberry (*59*). Replacing the same residue in mRFP1 with tryptophan led to a

yellow FP, mHoneydew (*62*). Introduction of the Glu65Thr mutation into mRFP1 led to an orange variant, mOrange (*62*) (Figure 1-6) that includes a third ring within the chromophore structure.

Mutations in the vicinity of the chromophore also have a large effect on the spectral properties. For example, a single point mutation to the wild type GFP gene, Thr203Leu, abolishes the favourable 490 nm peak and stabilizes the chromophore in its neutral form such that it has a single excitation peak at 395 nm (*24*). Furthermore, another substitution, Thr203Tyr leads to a 20 nm red shift in both the excitation and emission spectra (*28*). Tyr203 forms a π-π interaction with the chromophore phenol ring leading to a reduction in the energy of the excited state and a red shift in excitation and emission.

Although the environment around the chromophore has the strongest effects on the FP chromophore, the spectral properties can also depend on mutations far from the chromophore. For example, eight mutations were found necessary to generate a green to red photoconvertible fluorescent variant (KikGR) (*63*) from a GFP-like green FP (KikG, from the coral *Favia favus*) (*63*). Some of those mutations were not in the vicinity of the chromophore but were required for proper protein folding, maturation, and photoconversion.

1.2.4.2 Engineering for improved FP folding and brighter fluorescence:

The brightness of an FP is defined as the product of its molar extinction coefficient and quantum yield. The extinction coefficient reflects the ability of the chromophore to absorb light and, in the case of FPs, depends on proper folding and maturation. On the other hand, the quantum yield is a measure of the efficiency with which the chromophore emits fluorescence after absorbing light. Because the natural host of FPs are marine organisms, these proteins have evolved to fold most efficiently at reduced temperatures. When expressed in heterologous systems like mammalian cells, FPs often don't fold efficiently and therefore many translated polypeptide chains are "wasted" since they do not go on to produce a fluorophore. To address this, researchers have evolved FPs to have higher folding efficiency at 37 °C.

One of the most important and widely used engineered FPs is enhanced GFP (EGFP) (*64*, *65*). EGFP has two mutations relative to wild type GFP, Phe64Thr and Ser65Thr, which contribute to more efficient folding at 37 °C and a corresponding 30-fold increase of brightness over wild type GFP (*64*). In addition, codon optimization of the EGFP gene sequence to yield higher expression levels in mammalian cells (*65*) led to yet further increased brightness in mammalian live cell imaging. The wild type DsRed FP also suffers from slow protein folding and maturation (*45*, *66*). This was addressed by screening libraries of DsRed to identify faster

maturing variants. This effort resulted in the DsRed.T variants that exhibit 10-15-fold faster maturation (*67*).

Much of the observed brightness increases in engineered FPs are due to improvements in chromophore maturation efficiency that result in higher effective molar extinction coefficients. Improvement in quantum yield can also be achieved, though mutations that improve quantum yield are less commonly encountered. A recent study aimed at improving the quantum yield of FPs relied on computationally-assisted rational protein design (*68*). Pandelieva *et al.* started with mRojoA (*69*) (a dim red-shifted variant of mCherry FP) and evolved variants that helped to rigidify the chromophore by restricting its movement (*68*). Indeed, the brightest variant identified in this work exhibited ~3-fold improved quantum yield relative to mRojoA (0.03 to 0.09). The brighter variant had a tyrosine residue directly above the chromophore, which was hypothesized to limit the conformational degrees of freedom of the chromophore (*68*).

1.2.4.3 Engineering monomeric FPs:

Essentially all naturally occurring FPs have some tendency to oligomerize. This characteristic often complicates fluorescence imaging when FPs are used to tag proteins of interest because the oligomerization of the FP hinders the proper localization or function of the protein of interest. One typical observation is that a protein of interest fused to an oligomeric FP forms artificial aggregates when expressed in cells. Even the popular *Aequorea victoria* GFP and its derivatives show a weak

tendency to dimerize (*29, 70–72*). Fortunately, a single point mutation eliminates this dimeric tendency (*70*). FPs from *Renilla* sea pansy form obligate dimers and most yellow, orange and red FPs discovered in reef corals and sea anemones form obligate tetramers (*32, 45, 73*).

Engineering FP monomers from the tetrameric reef coral and sea anemone proteins proved to be far more difficult than point mutations that easily monomerized *Aequorea victoria* GFP. It was an engineering challenge that required multiple site directed mutations to disrupt the tetrameric interface, followed by random mutagenesis to rescue fluorescence. For example, DsRed from the coral *Discosoma striata* is an obligate tetramer (*45, 74*) with a hydrophobic interface and a hydrophilic interface for each protomer (*30, 75*) (Figure 1-7). DsRed was monomerized through iterative cycles of surface residue mutations and random mutagenesis that ultimately produced the monomeric red FP (mRFP1) with a total of 33 mutations compared to DsRed (*76*). mRFP1 is considered the first bright and monomeric red FP that was useful for fluorescence imaging of intracellular localization of fusion proteins (*76*). Another example of a tetrameric reef coral protein is cFP484 from *Clavularia sp*. coral. Using a similar approach, a monomeric teal FP, mTFP1 (*77*), was engineered after a total of 29 mutations and swapping seven residues at the N- and C- termini with those from GFP (*77*). mTFP1 is one of the brightest and most photostable FPs reported to date (*77*).
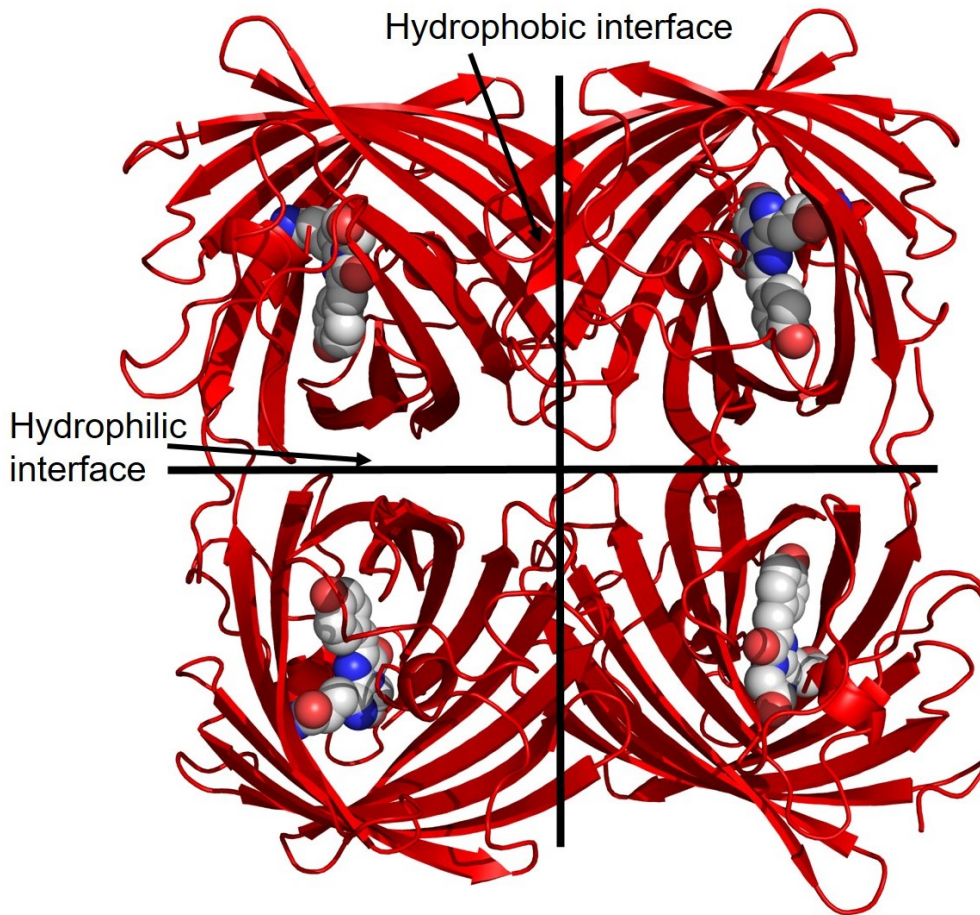
Figure 1-7 Cartoon representation of DsRed crystal structure showing its tetrameric structure. PDB ID 1GGX (*75*). Representation is prepared using PyMol (*31*).

1.3 Applications of FPs

Perhaps the most basic use of FPs is to use them as fluorescent reporters for imaging of subcellular protein localization in real time. An FP is used to tag proteins of interest and its localization is monitored using fluorescence microscopy. The ease with which this can be done using routine molecular biology techniques has enabled a revolution in

fluorescence imaging, ushering in a new age of knowledge about cellular processes. FPs can simply be genetically fused to the N- or C- terminus of a protein of interest. The gene encoding this protein fusion can be transiently expressed in cells by delivering the fused gene in a plasmid. The localization of the target protein can then be determined using fluorescence microscopy. Depending on the experiment, sustained and homogenous expression of a protein of interest tagged with an FP is also possible by generating stable cell lines or transgenic animals.

Another more elaborate example of utilizing FPs to image neural structure and connections is Brainbow (*78, 79*). This method involves the use of a multipart gene cassette with three to four different colour FPs that have *lox* recombination sites inserted between them. This gene cassette is then used to generate transgenic animals. Cre-loxP recombination (*80*) occurs in each neuron, causing a random combination of FPs to be expressed from each cassette. This random expression of a combination of FPs (*81*) labels individual neurons with a unique available hue of FP fluorescence, as visualized using a RGB model. This method has been used for exploration of neural connectivity, cell migration and lineage analysis (*82–90*).

The advent of photomodulatable FPs (i.e., photoactivatable, photoconvertible, or photoswitchable FPs) has enabled a plethora of more sophisticated fluorescence imaging techniques to study biology in more detail. These FPs can change their fluorescence state upon illumination of

light at a certain wavelength. This has been used to track cells in tissues and embryos (*91–93*), track cellular compartments and structures (*94–99*), and in studies of protein diffusion and binding kinetics (*100–102*). These studies are possible because discrete populations of proteins can be selectively highlighted and followed over time, an experiment that is not possible with traditional FPs.

Moreover, photomodulatable FPs have become valuable tools in super-resolution microscopy techniques that overcome the diffraction barrier (*103–105*). In these techniques proteins of interest, tagged with photomodulatable FPs, are illuminated in small numbers to maintain a density low enough that their diffraction-limited single molecule fluorescence spots don't overlap. The centers of those spots are then determined with high resolution (10s of nm) and the process repeated to construct a super-resolution image that is otherwise not possible with conventional diffraction-limited optical techniques.

In addition to the relatively straightforward uses of FPs mentioned above, protein engineers have developed FP-based indicators to report biochemical processes by fusing them with sensor domains. This will be discussed in more detail in the next section.

1.4 Genetically encoded FP-based indicators

Recognition of the relatively "malleable" nature of FPs opened the door to engineering of fully genetically encoded fluorescent indicators to visualize specific biochemical processes in live cells. Attaching FPs to a

sensory domain can lead to modulation of the FPs' fluorescence in response to a specific biochemical process. Because the FP requires no exogenous cofactors for fluorescence, FP-based indicators can be encoded in the genome and produced by the cell of interest through transient transfection or transgenic techniques. In this way, dynamic biochemical processes can be followed with high spatiotemporal resolution through real-time monitoring of fluorescence changes.

The first genetically encoded FP-based indicator was a protease indicator that was reported in 1996 (*106*). It was composed of a BFP and a GFP linked together by a trypsin cleavable linker (*106*). In this particular design, a change in the distance between the two FPs when the linker is cleaved leads to a change in the FRET signal. This can be measured by a change in the ratio of emission from the two FPs. Although this was a relatively simple design, it clearly established that FPs can be used as indicators.

FP-based indicators can be grouped into three main classes. The first class is indicators based on FRET, an example of which was briefly mentioned above. The second class is indicators based on bimolecular fluorescence complementation (BiFC), which utilizes the ability of some FPs to form from 2 fragments when the gene is expressed in a split form. The third class is indicators based on a single FP. For the single FP class of indicators, a biochemical event leads to a change in the chromophore environment of the FP, which in turn, leads to changes of its excitation and

emission spectra. These three classes of FP-based indicators are discussed in more detail below.

1.4.1 FRET-based indicators

FRET is the non-radiative transfer of energy from an excited state donor chromophore to an acceptor chromophore by dipole-dipole through-space interactions (*107, 108*). The efficiency of FRET is inversely proportional to the sixth power of the distance between the two chromophores. This makes FRET very sensitive to small changes in distance. FP-based indicators belonging to this class consist of a blue shifted donor FP and a red shifted acceptor FP that undergo distance- and/or orientation-dependent FRET. A requirement for the choice of the FP pair is that the donor emission spectrum and the acceptor absorbance spectrum should have significant overlap. Donor emission bleedthrough and acceptor cross-excitation should be minimized. Moreover, to engineer a robust indicator, FPs used should have high brightness, high photostability, and minimal tendency to dimerize.

FRET can be imaged by excitation of the donor FP while monitoring the dynamic change in fluorescence intensities of both the donor and acceptor FP throughout the course of an experiment. An increase in FRET efficiency is associated with quenching of donor fluorescence and an increase in the emission of fluorescence by the acceptor. This design is inherently ratiometric, which enables quantitative measurements despite cell-to-cell variability in expression of the indicator. Several FP-based

FRET indicator designs have been engineered to detect different biochemical processes. A typical design involves genetic fusion of an FP pair suitable for FRET to a sensing domain. Dynamic changes in the conformation of the sensing domain lead to a change in the relative distance and/or orientation of the FP pair leading to a change in FRET signal.

An overview of the four most commonly used designs of FRET-based indicators is shown in Figure 1-8. In the first design, the indicator is engineered, by genetically linking a FRET pair with a protease substrate sequence, to report the activity of a proteolytic enzyme. Initially, the two FPs are in close proximity and have a high FRET signal. Proteolysis of the substrate linker separates the FP pair resulting in a loss of FRET signal. Indeed, as mentioned above, the first example of an FP-based indicator was based on this design and involved insertion of a trypsin cleavable linker between BFP and GFP (*106*). Other examples for FRET-based protease indicators include indicators for caspases (*109–112*), hepatitis C virus NS3-4A protease (*113*), poliovirus 2A protease (*114*) and human enterovirus 3C protease (*115*). In the second FRET-based design, the donor and acceptor FPs are linked separately to two potential interacting proteins of interest. FRET occurs when the two proteins interact and form a complex. This process is typically reversible and FRET will decrease if the protein partners dissociate.
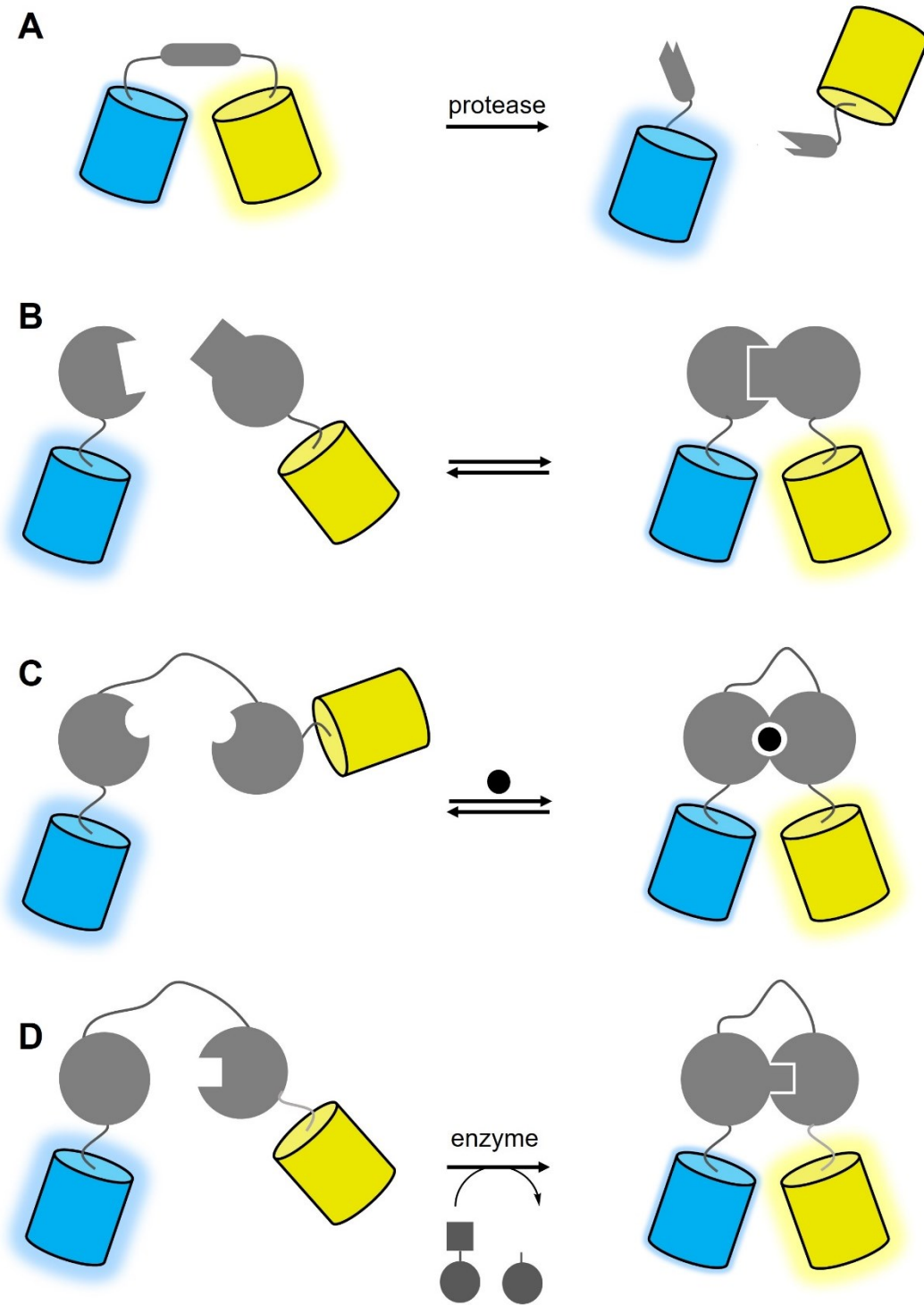
Figure 1-8 Overview of FP-based FRET indicator designs. (A) A protease indicator where a FRET pair is linked by a protease substrate. (B) An indicator for protein-protein interactions. (C) An indicator for small molecules (represented by a black circle). (D) An indicator for post-

translational modification enzyme activity. In all panels the cyan FP represents the donor, while the yellow FP represents the acceptor.

In the third design, FRET is used to report the binding of a small molecule to a sensory domain. The indicator is constructed by fusing the two FPs to flank the sensory domain. Binding of the small molecule induces a conformational change that leads to a change in distance and/or orientation of the FPs leading to a FRET signal. Perhaps the most famous FRET indicators belong to this group and are Ca^{2+} sensors known as cameleons (*12*, *116*). In cameleons the sensory domain is composed of the Ca^{2+} binding protein calmodulin and a Ca^{2+}/calmodulin binding peptide (*12*, *116–119*). Binding of Ca^{2+} induces calmodulin to wrap around the Ca^{2+}/calmodulin binding peptide and increase the FRET efficiency between the flanking FPs. Other examples that fall in this design include indicators for glucose (*120*), maltose (*121*, *122*), glutamate (*123*), Zn^{2+} (*124*) and cAMP (*125*).

In the fourth design, FRET is used to report the activity of enzymes that post-translationally modify a substrate polypeptide. Similar to the third design, the indicator is constructed by fusing the FP pair to flank a sensory domain. However in this case the sensory domain includes a substrate for the enzyme of interest and a binding domain. When the enzyme acts on its substrate this triggers the binding of both domains resulting in a change in FRET signal. Typical examples for this design include various types of kinase indicators (*126–130*).

1.4.2 BiFC-based indicators

Bimolecular fluorescence complementation (BiFC)-based indicators are normally used to report protein-protein interactions. In this type of indicator, the FP is split in two non-fluorescent fragments. One fragment is fused to a protein of interest and the other fragment is fused with an interacting protein partner. When the two proteins are not interacting, the two fragments show no fluorescence. Interaction between the two proteins brings the two FP fragments into close proximity, allowing reconstitution of an intact FP (*131*, *132*) (Figure 1-9A). Moreover, fluorescent complementation is also possible between fragments from different FPs (*133*) (Figure 1-9B). This allows for monitoring more than one interaction simultaneously.

By enabling visualization of protein-protein interactions, BiFC-based indicators have been used for subcellular localization of protein complexes (*134–138*), visualization of signal transduction networks (*139–143*), and in various high-throughput screens (*144–147*). However, an important consideration of BiFC-based indicators is that they are irreversible, and therefore not appropriate for applications that require real-time imaging of reversible events to be monitored. A more recently developed strategy for constructing indicators that can monitor reversible events relies on dimerization-dependant FPs (*148*, *149*). In this strategy, two dim fluorescent or non-fluorescent monomers reversibly associate to form a highly fluorescent dimer. Dimerization-dependant FPs have been used to

construct a variety of indicators including dynamic processes like Ca^{2+} ion concentration (*150*).
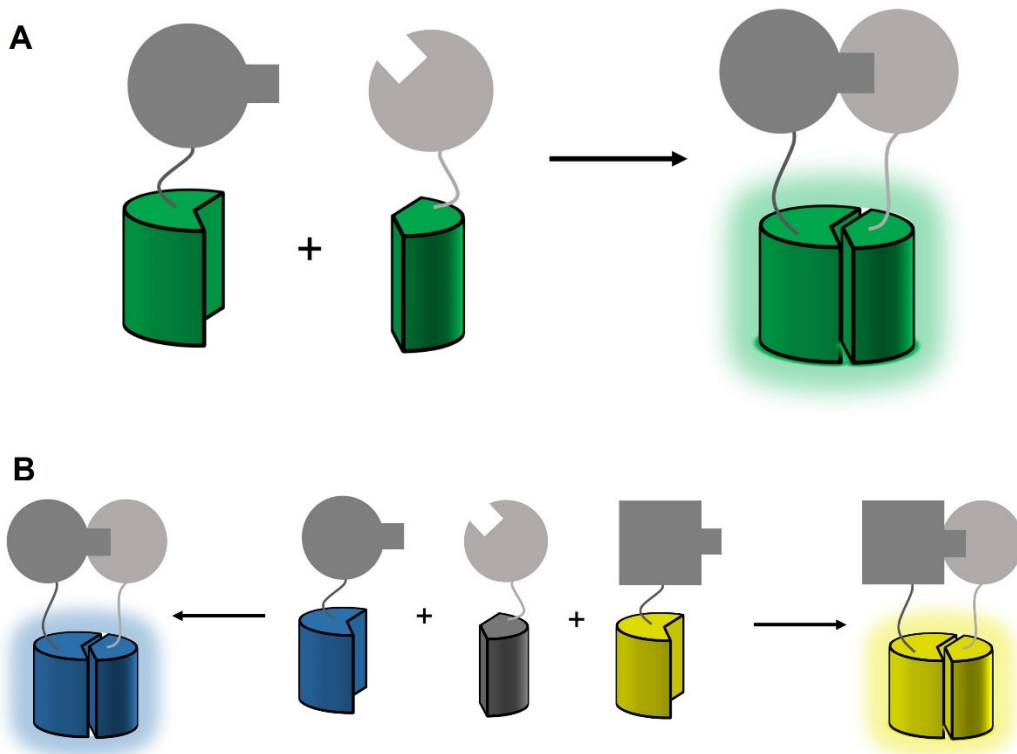
Figure 1-9 Overview of BiFC-based indicators. (A) Schematic of two proteins of interest fused to split fragments of an FP. When the proteins of interest interact, the FP fragments reconstitute fluorescence. (B) Schematic of multicolour BiFC by complementation using fragments of different FPs.

1.4.3 Single FP-based indicators

Single FP-based indicators rely on the ability of a single FP chromophore to change its spectral properties in response to a biochemical process. They can be subdivided into two main groups. The first group takes advantage of the inherent sensitivity of an FP barrel to its

environment. For example, some FP barrels are inherently sensitive to pH and halide ion concentration (*151*, *152*). This is normally regarded as a disadvantage when using the FP as a static fluorescent tag for proteins of interest. However, this sensitivity also makes some FPs suitable for use as indicators for pH and halide ion concentration (*151*, *152*). Different colours of FP variants with improved pH sensitivity have been engineered to monitor pH during live cell imaging (*153–156*). Improved and more selective halide ion indicators have also been engineered (*157*, *158*). Moreover, FPs have been engineered to report redox potential by installing cysteine residues on the outer surface of the barrel in close proximity to the chromophore (*159–161*).

The second group of single FP-based indicators depends on the incorporation of a sensory domain that changes its conformation in response to a biochemical event. This change in conformation is then relayed to the FP chromophore environment leading to a change in its spectral properties. The sensory domain needs to be incorporated such that it would not disrupt the proper folding and maturation of the FP. At the same time, in order for conformational changes to be efficiently relayed to the chromophore, the sensory domain must also be close to the chromophore. Because the wild type N- and C- termini of FPs are far from the chromophore (Figure 1-2), simple fusion of a sensory domain on either termini of the FP will probably not result in a significant change in the chromophore environment. This led protein engineers to change the N-

and C- termini and bring them spatially closer to the chromophore by generating circularly permutated FP (cpFP) variants. This was achieved by genetically linking the original N- and C- termini with a flexible linker and introducing new N- and C-termini that are closer to the chromophore (Figure 1-10).
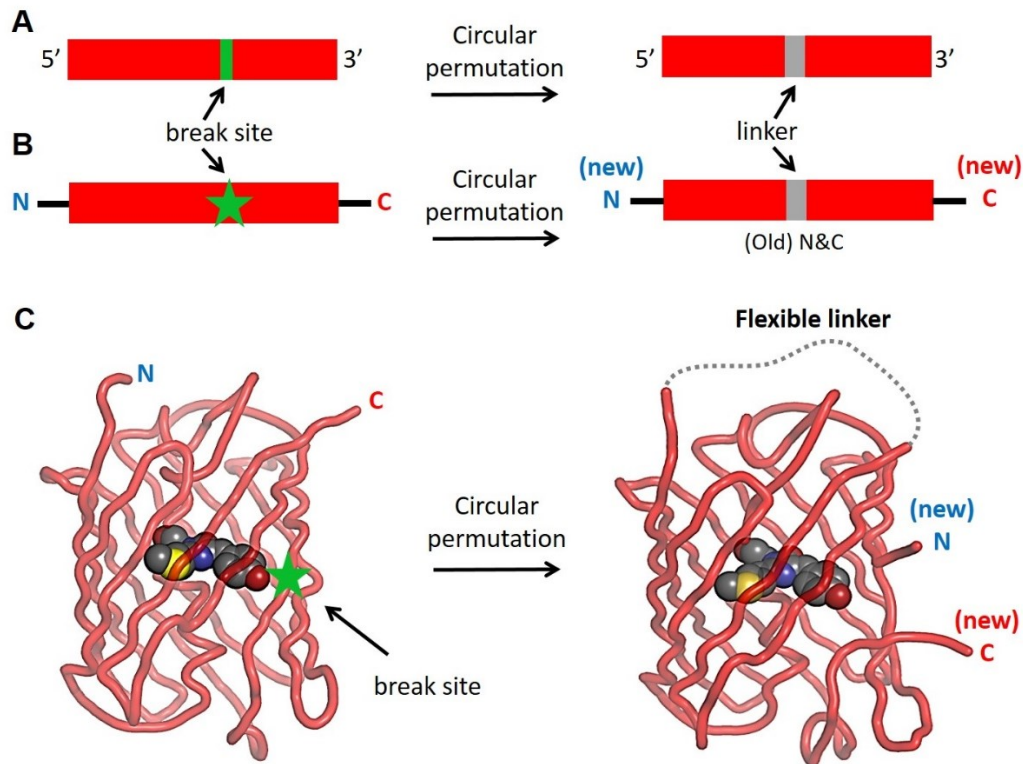
Figure 1-10 Circular permutation of FPs. (A) Schematic showing DNA sequence rearrangement for circular permutation. The original 3' end of the gene is linked with the original 5' end of the gene. (B and C) Schematic of circular permutation in RFP. The old N- and C- termini are linked by a flexible linker and new N- and C- termini are created close to the chromophore. Cartoon representation in (C) is prepared using PyMol (*31*).

In fact, the first application of circular permutation with FPs was a result of a serendipitous finding. During random mutagenesis of a cyan FP, a variant was found with six residues inserted at position 145 that maintained its fluorescence (*162*). This suggested that FP barrels might be amenable to circular permutation at position 145 and still mature and form a functional FP barrel. Interestingly, subsequent systematic interrogation for alternative circular permutation sites that are suitable for relaying conformational changes to the chromophore did not yield any positions that are as close to the chromophore and as well-tolerated as position 145.

Perhaps the most commonly used FP-based indicator is the Ca^{2+} sensor GCaMP (*13*). GCaMP is a fusion of a Ca^{2+} sensing domain to circularly permutated GFP. The Ca^{2+} sensing domain in this case is made up of two fragments; an M13 peptide bound to the N-terminus of the cpGFP barrel, and calmodulin fused to the C-terminus of the cpGFP barrel. In the unbound state, the GFP chromophore is exposed to the bulk solution and exhibits dim fluorescence. When Ca^{2+} is present, the calmodulin domain wraps around the M13 peptide leading to a more conformationally rigid linker that prevents access of the solvent to the chromophore restoring its fluorescence (*163*, *164*) (Figure 1-11). This design has been used to engineer greatly improved GCaMP variants that are ultrasensitive to Ca^{2+} fluctuations (*165*, *166*). In addition, swapping the cpGFP with different colour cpFP barrels led to Ca^{2+} sensors spanning the

visible spectrum (*167–171*). Other examples using cpFPs are indicators for membrane potential (*15*), glutamate (*123*) and redox potential (*172*).
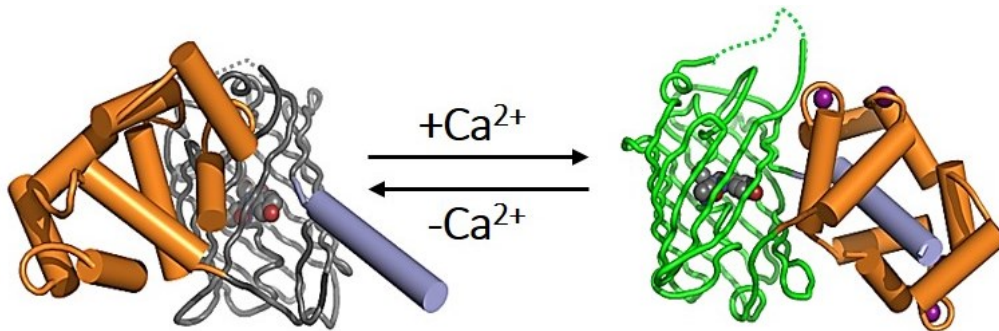
Figure 1-11 Cartoon schematic of GCaMP. Calmodulin shown as brown tubes, M13 peptide shown as a purple tube. In the presence of Ca^{2+}, CaM wraps around M13 and restores fluorescence. PDB ID 3EVR. Cartoon representations are prepared using PyMol (*31*).

1.5 Challenges of studying neuronal activity

Having introduced FPs and FP-based indicators, it is prudent to briefly introduce the challenges that face the neuroscience community in using those tools (and others tools) to interrogate neural circuits. Neural circuits communicate at spatial and temporal scales spanning orders of magnitude (from micrometers to millimeters and from milliseconds to weeks) (*173*). The first challenge to neuroscientists is monitoring this activity with the required spatial and temporal resolution. The second challenge is to be able to monitor this activity in living animal models so that studies can be used to better understand phenomena like learning, memory, and sensory-motor skills.

A growing set of tools for studying neural circuits *in vivo* exists and are being improved regularly. Each tool has its strengths and inherent drawbacks. For example, in most neuroscience laboratories voltage recordings have traditionally been done using patch clamp (*174, 175*). The patch clamp method gives a remarkably high temporal resolution recording of membrane potential fluctuations at the microsecond time-scale. However this method is limited by the number of cells that can simultaneously be interrogated. Parallel recordings from hundreds of cells can be achieved using multi-electrode arrays to record field potentials, however this method sacrifices spatial resolution as the signal cannot be attributed to a specific cell (*176*). Optical imaging of the activity of numerous cells simultaneously can be achieved using Ca^{2+}- or voltage-sensitive small-molecule organic dyes (*177, 178*). Drawbacks of small-molecule organic dyes include: high fluorescence background due to residual dye in the extracellular space, non-specific staining of all cell types, inability to target a genetically-defined subset of cells of interest, and incompatibility with long-term imaging (*178*).

Optical imaging using genetically encoded indicators *in vivo* has the potential to overcome the drawbacks of organic dyes, and enable robust, cell type-specific, long-term reporting of neural activity. However, practical issues have prevented genetically encoded indicators from realizing their full potential. The first issue is the properties of the genetically encoded indicators themselves, including kinetics, response amplitude, brightness

36

(which has to sufficiently high to enable high speed recording), and photostability. The second issue is light scattering, which limits the depth of imaging in brain tissue. These two issues could potentially be circumvented by developing red shifted indicators that have improved characteristics allowing robust neural imaging *in vivo*.

1.6 Scope of the thesis

The objective of my thesis is to use protein engineering to develop FP-based neural activity indicators with improved spectral properties and other characteristics. In contrast to past efforts to develop such indicators, I relied heavily on the use of directed protein evolution to select for variants with desired properties. In this process, rational and random mutagenesis of protein residues is used to generate protein libraries that explore part of the protein space. Effective screening of those libraries for the desired characteristics (like brightness, kinetics, and response amplitude) leads to the identification of variants that "win" the screen with improved characteristics relative to their parent template.

Chapter 2 describes our work to develop the first bright red voltage indicator that reports single action potentials with high fidelity in single trial recordings. In Chapter 3, I describe our efforts to explore novel designs in engineering FP-based voltage indicators based on tandem dimer voltage sensor domains. Using these designs we successfully engineered prototypes for a red voltage indicator and a green/red ratiometric voltage indicator. Chapter 4 reports our work to develop the first highlightable

voltage indicator. We engineered a green to red photoconvertible voltage indicator that reported membrane potential changes in mammalian cells. Chapter 5 describes our efforts in developing a GFP-based GABA indicator. In Chapter 6, I conclude with a summary of the thesis and highlight some potential future directions.

Chapter 2 Engineering a red voltage indicator for live cell imaging[1]

2.1 Introduction

Optical imaging of membrane potential using voltage indicators based on green FPs or Archaerhodopsin has emerged as a powerful approach for detecting the activity of many individual neurons with high spatial and temporal resolution. Despite the fact that prototypes of both genetically encoded voltage and Ca^{2+} indicators were first reported in 1997 (*12*, *179*), the development of robust voltage indicators has lagged far behind Ca^{2+} indicators. The design that has proven most successful for developing Ca^{2+} indicators with large dynamic range is based on fusing a cpFP (*162*) to a Ca^{2+} sensing domain (*11*, *13*, *165*, *167*). Similarly designed voltage indicators, constructed by fusing FPs to voltage sensing domains (VSDs), typically suffer from small response amplitude, slow kinetics, and/or poor membrane localization (*179*, *180*). However, two recently reported green FP-based voltage indicators, ArcLight (*14*) and ASAP1 (*15*), are able to resolve single action potentials in neurons in single trials.

Four design strategies have been used to engineer genetically encoded voltage indicators. The first uses a voltage sensitive domain fused to an FP (*14*, *15*, *179–185*). This class includes two green FP-based

---

[1] A version of this chapter has been published as: A. S. Abdelfattah *et al.*, *J. Neurosci.* **36**, 2458–2472 (2016).

voltage indicators, ArcLight (*14*) and ASAP1 (*15*), which are able to resolve single action potentials in neurons in single trials. ArcLight has the highest response amplitude (~30% ΔF/F to a 100 mV step) (*14*) yet reported for an FP-based voltage indicator. However, its slow kinetics produces a response to action potentials of only ~3% ΔF/F (*14*). The ASAP1 indicator has a smaller response amplitude (~17% to a 100 mV step) (*15*) but exhibits faster kinetics, and therefore its response to action potentials is ~5% ΔF/F (*15*).

The second class of voltage indicators also uses a voltage sensitive domain, but relies on the modulation of FRET between two fused FPs (*186*, *187*). Although these sensors can have relatively large ratiometric changes (>10%), the kinetics are typically slow (τ > 10 ms) (*186*, *187*). The third class is based on microbial rhodopsins, which can exhibit voltage-dependent changes in the fluorescence of their bound retinal cofactor (*188*, *189*). Although these indicators show larger response to voltage changes, the brightest variants (known as QuasArs) (*190*) are still much dimmer than FP-based voltage indicators (*190*, *191*). One important advantage of the microbial rhodopsin-based indicators is that, relative to the currently preferred members of the other classes, they have a near-infrared fluorescent emission. The fourth class is based on FRET from an FP to a microbial rhodopsin with a voltage-dependent absorption (*192*, *193*). This design circumvents the brightness issue of the third class at the cost of a blue shift in fluorescence emission and slower kinetics (*192*,

193). While many of the previously reported FP-based voltage indicators have one or more near-ideal properties, none has yet emerged as the optimal combination of all favourable properties.

Red-shifted fluorophores that require longer wavelength excitation light provide the added advantages of lower phototoxicity, deeper tissue penetration, and lower autofluorescent background (*194*). Moreover they are spectrally distinct from green fluorescent indicators and blue-light excitable channelrhodopsin variants (*195*). The only reported attempt to engineer an indicator based on a cp red FP (cpRFP) resulted in indicators that are not practically useful due to small fluorescence responses (~1% ΔF/F to 200 mV step potentials) and slow kinetics (τ_{on} ~60 ms and τ_{off} ~150 ms) (*182*). We set out to develop a new FP-based voltage indicator that combined the advantages of red-shifted fluorescent emission with the higher brightness of FPs, while also affording the fast kinetics required to report neuronal activity. Note that we follow the convention of referring to FPs that emit in the 590-620 nm range as "red", although such wavelengths are more accurately described as orange.

In this chapter we describe the development of a bright and fast red voltage indicator based on a fusion of a cpRFP (cpmApple) and the VSD from *Ciona intestinalis* (Ci) voltage sensitive phosphatase (*196*). This fusion was used as a template for directed protein evolution to improve brightness and voltage sensitivity. The end product is FlicR1 (**Fl**uorescent **i**ndi**c**ator for voltage imaging **R**ed), with kinetics and relative response

amplitude comparable to the best available green voltage indicators. We show that FlicR1 reports single action potentials in single-trial recordings from neurons and can track high frequency voltage fluctuations (up to 100 Hz). We also demonstrate that FlicR1 can be combined with a blue-shifted channelrhodopsin, PsChR (*197*), and spatially patterned blue illumination to simultaneously perturb and image membrane potential in the same neuron. However, blue light-photoactivation of the FlicR1 chromophore, as observed in R-GECO1 which has the same FP barrel and chromophore (*198*), presents a challenge for applications that require spatially overlapping yellow and blue excitation.

2.2 Results

2.2.1 Development of FlicR

The first step for creating the voltage indicator was to make a chimera from the genes for a red-shifted FP and a voltage sensitive domain (Figure 2-1A, B). Our choice of the red-shifted FP to use as the template was inspired by the X-ray crystal structure (*170*) of the Ca^{2+} indicator, R-GECO1 (*167*). The structure reveals that the Lys80 (R-GECO1 numbering) side chain from the surface of the cpmApple-derived β-barrel engages in an electrostatic interaction with the phenolate oxygen of the chromophore. This structural evidence, combined with additional mutagenesis results (*168*), points to this interaction as the mechanistic basis for the response of R-GECO1. Since the lysine is part of the β-barrel

42

(in contrast to GCaMP, where the key interaction is with an arginine from CaM (*164*)), we reasoned that the cpmApple domain is likely a self-contained unit that would retain its fluorescence modulation mechanism even if the Ca^{2+} sensitive domain were replaced with an alternative sensing domain.
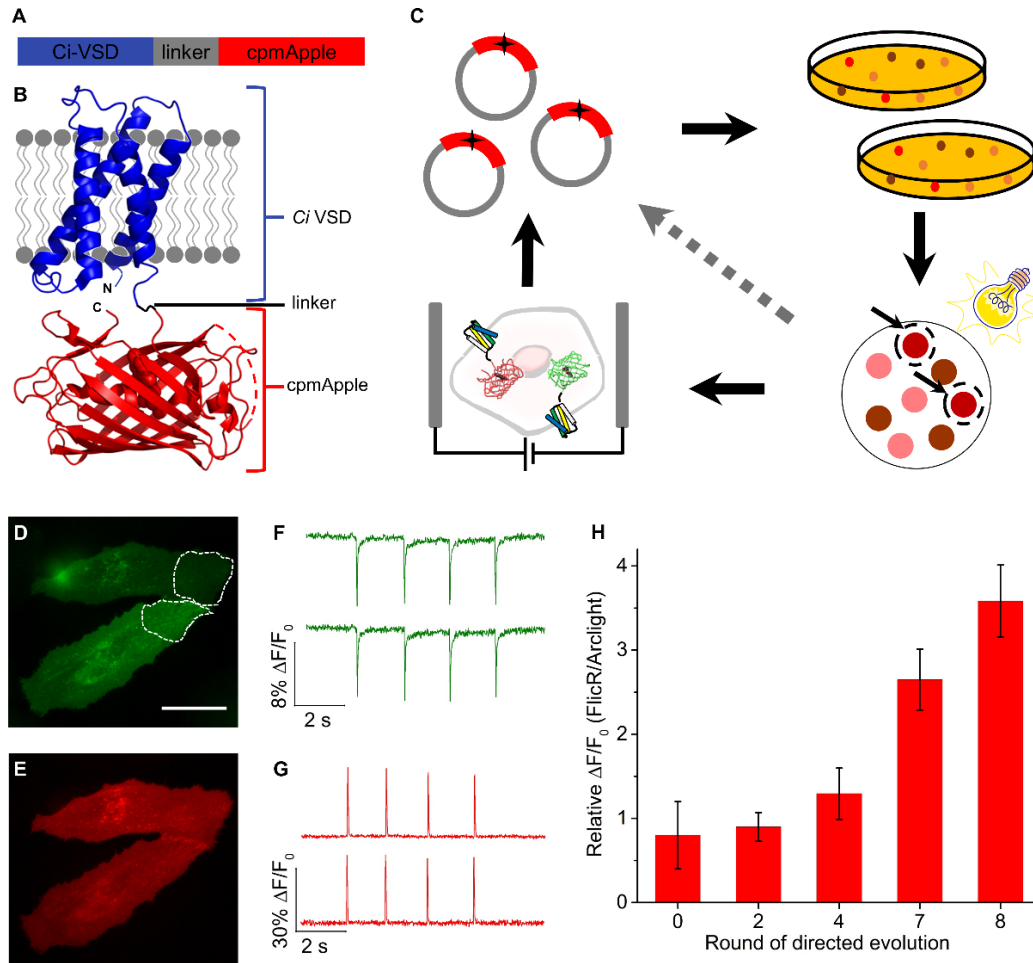
Figure 2-1 Schematic representation of FlicR indicator and directed evolution process. (A-B) Representation of FlicR indicator. (B) A model of FlicR1 represented by the crystal structures of CiVSD (PDB ID 4G80) (*199*) and cpmApple (PDB ID 4I2Y) (*170*). (C) Schematic representation of directed evolution strategy used to develop FlicR1. First, libraries of DNA encoding indicator genes were transformed into *E. coli* and cultured on

43

agar plates. Second, *E. coli* colonies expressing FlicR1 were illuminated with yellow light. Colonies with bright red fluorescence were picked and screened for voltage sensitivity in mammalian cells. Voltage sensitivity of FlicR1 variants was then tested via field stimulation in HeLa cells co-expressing ArcLight. (D-E) Image of HeLa cells co-expressing ArcLight Q239 (D) and FlicR1 (E), Scale bar 10 μm. (F) ArcLight fluorescence response of two regions shown in (D) to electrical field stimulation pulses (10 ms, 25 V). (G) FlicR1 fluorescence response of the same two regions shown in (D) to electrical field stimulation pulses (10 ms, 25 V). (H) Improvement in voltage sensitivity of FlicR variants during directed evolution. Represented as a ratio of response amplitude in HeLa cells compared to ArcLight Q239. Error bars are standard deviation (n = 10-15 cells). Fluorescence imaging for field stimulation measurements was performed at 100 Hz. Illumination intensities were 0.2 W/cm^2 for FlicR1 and 0.1 W/cm^2 for ArcLight Q239.

We chose to use CiVSD as the voltage sensitive domain to fuse to cpmApple because it localizes properly to the cell membrane of mammalian cells, as demonstrated by its successful use in recent FP-based voltage indicators (*14*, *181–183*, *186*, *187*). We elected to use a cpFP to increase the chance of coupling voltage-induced conformational changes in the VSD to a change in the FP chromophore environment, likely through its influence on the conformation of the Lys80 side chain. Specifically, fusion of cpmApple to the C-terminus of CiVSD should bring Lys80 and the chromophore in close proximity to the mobile S4 helix of the VSD domain. We hypothesized that this design should maximize the

likelihood of developing an indicator with fast kinetics since movement of S4 could directly influence the chromophore environment.

Although directed protein evolution has been one of the main strategies to improve FP properties and FP-based Ca^{2+} indicators (*165, 167*), it has not been widely implemented for voltage indicators. To facilitate our directed evolution strategy, we designed a high-throughput workflow for screening of voltage indicators (Figure 2-1C). This procedure was divided in two steps. The first step is an *E. coli* bacterial colony screen for brightness, and the second step is a mammalian cell screen for voltage sensitivity. The second step of the screen also enabled us to assess the membrane localization of the engineered variants, so that variants that do not localize properly can be excluded from further rounds of screening. In brief, libraries of genes encoding voltage indicator variants were inserted in a dual bacterial and mammalian expression vector, and used to transform *E. coli*. After overnight growth on agar plates, the red fluorescence of the colonies was imaged using a custom fluorescence imaging setup (*200*) that can image approximately 1000 colonies simultaneously, enabling the screening of tens of thousands of variants per round. The brightest variants were cultured and their plasmid DNA was used to transfect HeLa cells co-expressing ArcLight Q239 and an inward rectifying potassium channel (Kir2.1). ArcLight Q239 provides an internal reference to assess voltage sensitivity. Kir2.1 hyperpolarizes the resting membrane potential of HeLa cells to approximately -60 mV (*190,*

192, 201) to mimic that of neurons. The transfected cells were subjected to 10 ms electrical field pulses using a custom-built field stimulation system and fluorescence response to stimulation was recorded (Figure 2-1D-G). FlicR variants with the highest voltage sensitivity were selected to go on to the next round of directed evolution.

For our first-generation construct, we fused cpmApple (residues 60-304, R-GECO1 numbering (*170*)) (Figure 2-2) to the C-terminus of CiVSD truncated at residues 236 through 242 to construct seven variants. We chose these positions to bring cpmApple as close as possible to the S4 helix. The shortest linker that exhibited fluorescence was the variant with CiVSD truncated at 239. Our experience with evolving FP-based indicators (*14*, *167*, *185*, *198*) has shown that even small adjustments in the linker between the sensing domain and the FP are critical to the indicator function. In an effort to identify the optimal composition of the linker between CiVSD and the cpmApple domain, we created a library of 1024 gene variants (400 protein variants) by fully randomizing the codons for two residues immediately following residue 239 of CiVSD (Pro240 and Val241, respectively). Screening of this library for red fluorescence, followed by voltage sensitivity tests in HeLa cells subjected to field stimulation, led to the identification of a variant with mutation Pro240Arg. We designated this variant as our first generation **Fl**uorescent **i**ndi**c**ator for voltage imaging-**R**ed (FlicR). This FlicR variant (FlicR0.1) exhibited dim fluorescence that was responsive to membrane potential changes in

46

mammalian cells, albeit with a small response amplitude (Figure 2-1H). Notably, FlicR0.1 (and all subsequent variants) exhibits an increase in fluorescence in response to membrane depolarization, whereas ArcLight and ASAP1 exhibit decreases in fluorescence. To evolve FlicR0.1 brightness and voltage sensitivity, we used both rational design and directed protein evolution by multiple rounds of construction and screening of libraries containing thousands of variants.
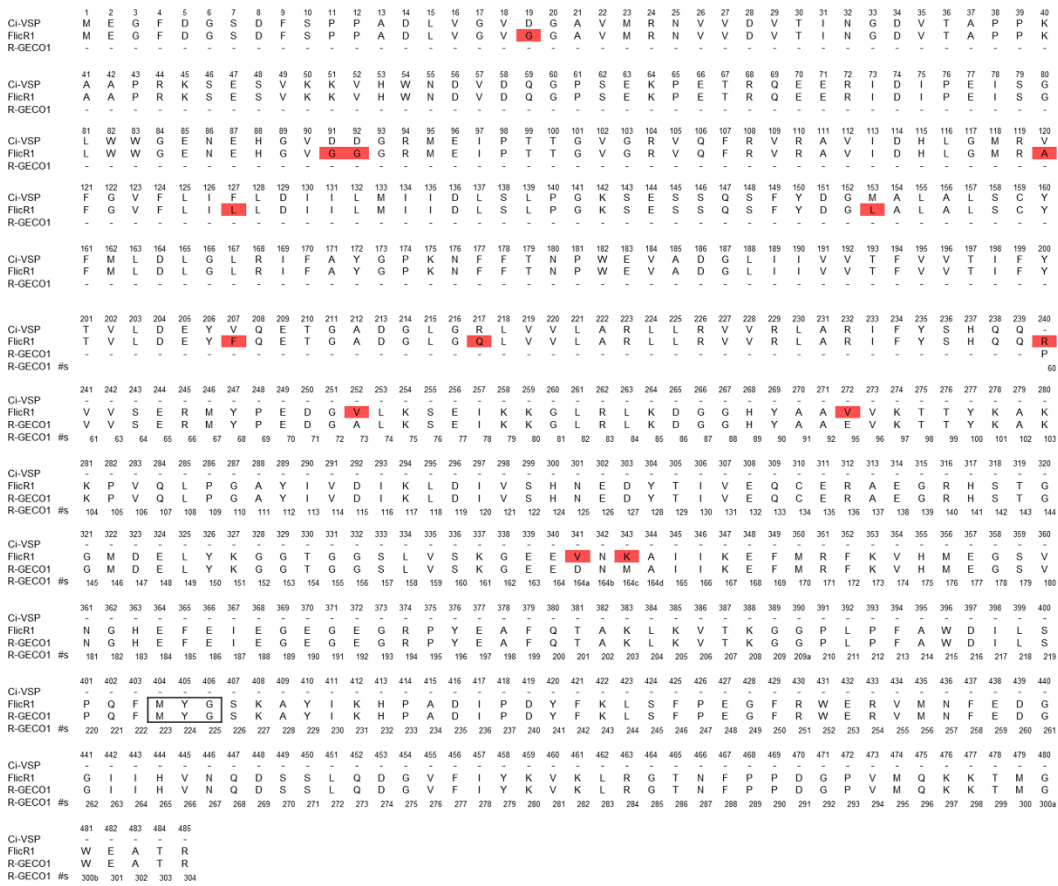
Figure 2-2 Sequence alignment of FlicR1. Alignment of FlicR1 gene with CiVSD domain (top) and cpmApple (residues 60-304, R-GECO1 numbering) from R-GECO1 (bottom). The red highlighted residues are the amino acid mutations of FlicR1 compared to the starting template. Residues MYG in the box correspond to the mApple chromophore.

47

Calmodulin (CaM) and the M13 peptide are not shown in the R-GECO1 sequence.

In a typical round of directed evolution, we used error-prone PCR to create a large library based on our most promising template(s), and then screened the library using the workflow described above. A mixture of the 3-6 variants with the brightest fluorescence, proper membrane localization, and largest responses to voltage change would then be used as the template for the next round of library creation by random mutagenesis. Four rounds of this procedure led to FlicR0.5 which was 16 ± 3-fold brighter than FlicR0.1 (n = 100 colonies) and could easily be imaged with widefield fluorescence microscopy when expressed in mammalian cells. Three more rounds of evolution were then performed, with greater emphasis placed on identifying variants with improved voltage sensitivity, rather than improved brightness. This effort led to the identification of the Val207Ala mutation, located in the S3 to S4 linker of the CiVSD, which provided a pronounced improvement in voltage sensitivity. For the eighth round of evolution, we mutated position 207 to all 20 possible amino acids and screened the library as before. The best variant identified from this library harboured the Val207Phe mutation that further improved the voltage sensitivity (Figure 2-1E, G). This variant, which has 12 mutations relative to FlicR0.1 (Figure 2-2), was designated as FlicR1. Relative to ArcLight Q239, FlicR1 has a 3.6 ± 0.4-fold (n = 12 HeLa cells) greater fluorescence response to a 10 ms electrical pulse

(Figure 2-1D-H). When stimulated with a train of electrical pulses at 10 Hz, FlicR1 fluorescence response showed faster response and decay kinetics compared to ArcLight Q239, which did not return to baseline between stimulations.

2.2.2 Characterization of FlicR1 in HEK cells

To quantify the voltage sensitivity and speed of FlicR1, we expressed it under a CMV promoter in human embryonic kidney (HEK) cells and used whole-cell voltage clamp to change membrane potential while recording FlicR1 fluorescence under 561 nm illumination (10 W/cm^2). FlicR1 trafficked well to the membrane of HEK cells (Figure 2-3A). When we applied a triangle wave of membrane voltage from −100 mV to +50 mV, fluorescence increased almost linearly with membrane voltage, with a fluorescence change ($\Delta F/F_0$) of 6.6 ± 0.6% (n = 5) per 100 mV (Figure 2-3B, D). This sensitivity is almost an order of magnitude larger than previously reported cpRFP-based voltage sensors (*182*). To measure the kinetics of FlicR1, we stepped membrane voltage between −70 and +30 mV at 22 °C (Figure 2-3C). These steps induced a rapid biexponential response in the fluorescence of FlicR1, with a dominant fast component that had a 3.0 ± 0.1 ms time constant accounting for 90% of the activation response. For deactivation, the fast component made up 70% of the response and had a time constant of 2.8 ± 0.2 ms (Figure 2-3F and Table 2-1). These values compare favourably to ArcLight Q239 kinetics at 22 °C, which follow a biexponential response to the same protocol with

time constants of 28 ± 8 ms (39%) and 271 ± 6 ms (61%) for the rising edge and of 100 ± 20 ms (61%) and 280 ± 40 ms (39%) (n = 6) for deactivation (Figure 2-3E, G, H and Table 2-1). We repeated the FlicR1 measurements at 34 °C and found that the time constant of the fast component decreased to 0.74 ± 0.06 ms (90%) for activation and 0.93 ± 0.07 ms (79%) for deactivation (n = 6) (Figure 2-3F and Table 2-1). The sensitivity at this temperature was 6 ± 1% per 100 mV and not significantly different from the value at 22 °C (n = 6, P = 0.49, two–tailed student's t-test).
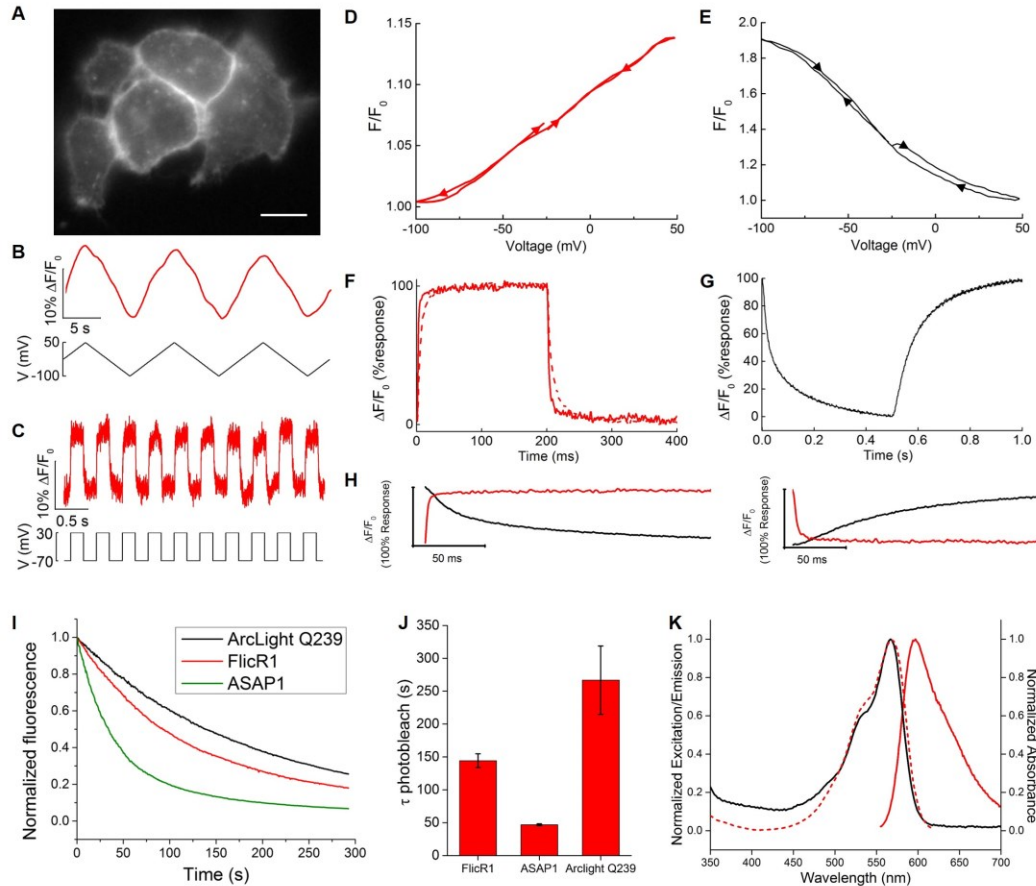
Figure 2-3 Characterization of FlicR1. (A) Image of HEK293 cells expressing FlicR1 under the CMV promoter. Scale bar 10 μm. (B) Fluorescence response (top) to a triangle wave in membrane potential (bottom) from −100 mV to +50 mV. Fluorescence trace (acquired at 10 Hz) is filtered using a 15 point moving average low-pass filter. (C) FlicR1 fluorescence response (top) from a representative cell to a square wave in membrane potential (bottom) from −70 mV to +30 mV. (D-E) FlicR1 (D) and ArcLight Q239 (E) fluorescence as a function of membrane voltage in a representative HEK293 cell. Fluorescence is the mean of three ramp cycles from −100 mV to +50 mV and back. Fluorescence is plotted starting at –25 mV, depolarizing to +50 mV, hyperpolarizing to –100 mV, and then returning back up to –25 mV as marked by the arrows. Fluorescence showed little hysteresis between increasing and decreasing voltage ramps. (F) FlicR1 fluorescence response to a 100 mV step potential in

HEK293 cells. Solid line shows fluorescence response at 34 °C. Dotted line shows fluorescence response at 22 °C. (G) ArcLight Q239 fluorescence response to a 100 mV step potential in HEK293 cells 22 °C. Note the different time axis compared to (F). (H) Zoom in on "on" and "off" portions of 22 °C fluorescence traces from FlicR (red) and ArcLight (black). (I) Normalized bleaching curves for FlicR1, ArcLight and ASAP1 in HEK239 cells. (J) Time constants for photobleaching of FlicR1, ASAP1 and ArcLight Q239 in HEK293 cells using continuous 10 W/cm^2 561 nm light illumination for FlicR1 and continuous 10 W/cm^2 488 nm light illumination for ASAP1 and ArcLight Q239. Fluorescence was captured every 500 ms. Time constants are based on single exponential fits. Error bars are standard error of the mean for FlicR1 (n = 5 cells), ASAP1 (n = 5 cells) and ArcLight Q239 (n = 4 cells). (K) Spectral characterization of FlicR1 *in vitro*. Absorbance (solid black line), excitation (dotted red line) and emission (solid red line) of FlicR1. Fluorescence imaging for voltage sensitivity measurements was performed at 10Hz. Step responses were recorded at 2 kHz for FlicR1, 1 kHz for ArcLight Q239. Illumination intensities were 10 W/cm^2.

Table 2-1 FlicR1 and ArcLightQ239 kinetics in HEK293 cells. Values for ArcLight Q239 at 34 °C are from Ref. (*14*).

		Activation -70 mV to 30 mV	Deactivation 30 mV to -70 mV	Activation -70 mV to 30 mV	Deactivation 30 mV to -70 mV
FlicR1	τ1 fast (ms)	3.0 ± 0.2	2.8 ± 0.3	0.74 ± 0.06	0.93 ± 0.07
	τ2 slow (ms)	41 ± 7	18 ± 3	27 ± 6	14 ± 6
	% fast component	90 ± 2	70 ± 4	90 ± 2	79 ± 4
	n	5		6	
ArcLightQ239	τ1 (ms)	28 ± 8	100 ± 20	9 ± 1	17 ± 1
	τ2 (ms)	271 ± 6	280 ± 40	48 ± 4	60 ± 7
	% fast component	39 ± 8	61 ± 15	50 ± 3	79 ± 3
	n	6		6	

We compared the rate of photobleaching of FlicR1 with other FP-based voltage indicators using 10 W/cm^2 of either 561 nm (FlicR1) or 488 nm light (ASAP1 and ArcLight Q239) (Figure 2-3I). Single exponential fits gave photobleaching time constants of 150 ± 10 s (*n* = 5 cells) for FlicR1, 47 ± 1 s (*n* = 5 cells) for ASAP1, and 300 ± 30 s (*n* = 4 cells) for ArcLight Q239 (Figure 2-3J). Measurement of the absorbance, excitation, and emission spectra of FlicR1 *in vitro* (Figure 2-3K) revealed excitation and emission maxima of 570 and 597 nm, respectively.

The fact that the absorption spectrum of FlicR1 is red-shifted relative to other FP-based voltage sensors made it a promising candidate for two-photon excitation in the 1100-1300 nm range. To test the utility of FlicR1 for two-photon imaging, a two-photon scanning-beam microscope, set to

deliver 1120 nm excitation pulses, was used to image HEK cells expressing FlicR1. Under whole-cell voltage clamp, the membrane voltage was varied in a square wave between −100 to +100 mV at 2 Hz. FlicR1 responded with a fluorescence change ΔF/F of 9 ± 1% per 100 mV (n = 8 cells) (Figure 2-4A).
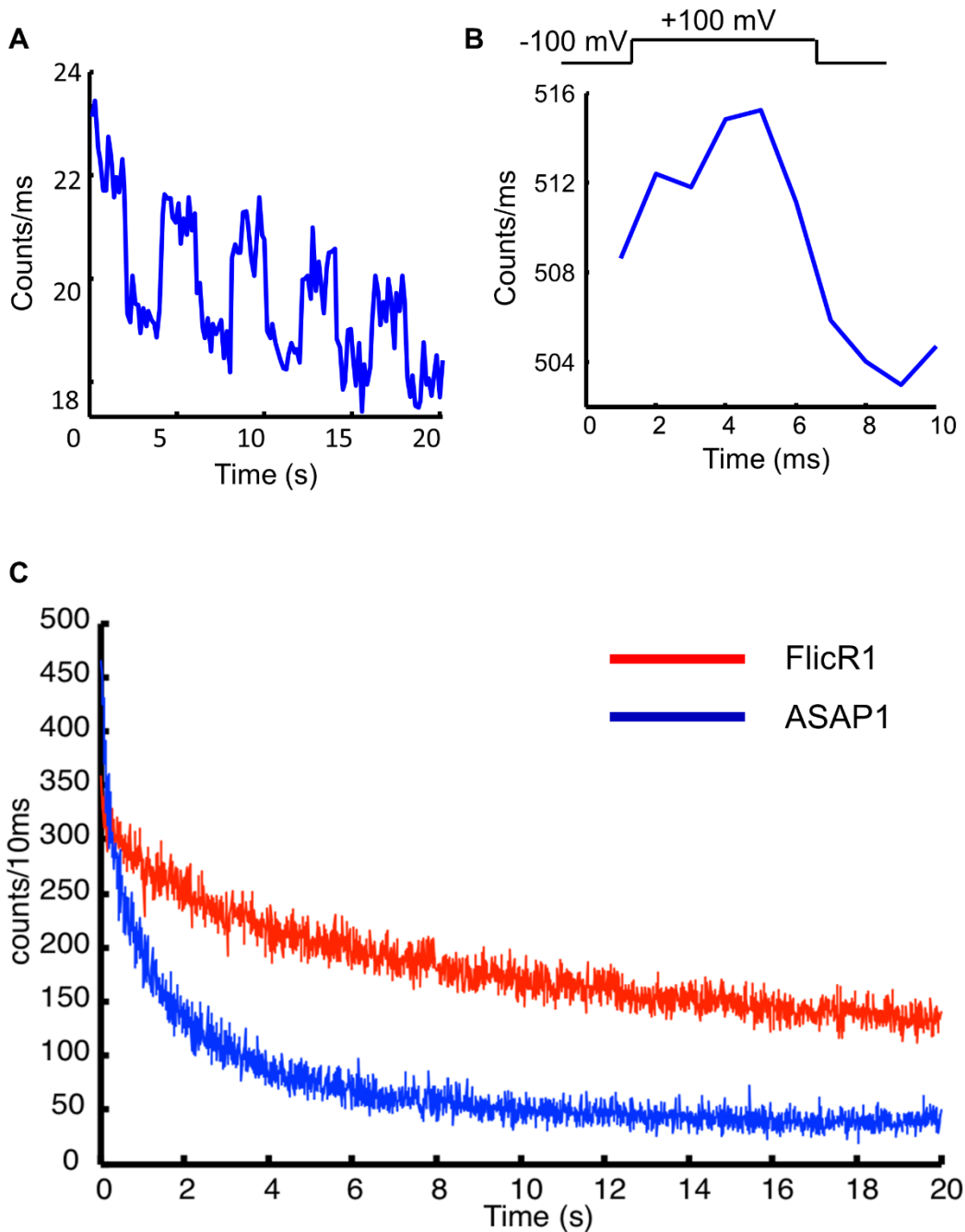
Figure 2-4 Two-photon imaging of FlicR1 in HEK cells. (A) The uncorrected fluorescence response of FlicR1 during −100 to +100 mV voltage steps (0.25 Hz square wave, 2 s +100 mV, 2 s −100 mV) when excited at 1120 nm in image-scanning mode (6.5 frames/s). (B) Fluorescence intensity as a function of time for a 1000 Hz point scan of FlicR1 fluorescence during a 100 Hz voltage square wave (5 ms +100 mV,

5 ms −100mV) (n = 50 cycles averaged). (C) Fluorescence intensity as a function of time for a point scan of ASAP1 excited at 950 nm and FlicR1 excited at 1120 nm. Fluorescence is sampled at 100 Hz, with excitation power (~1 mW at both wavelengths) tuned to achieve ~400 counts per bin initially.

The speed of the FlicR1 response to a voltage step under two-photon excitation was tested in point-recording mode. Cells were subjected to a square wave in voltage from −100 to +100 mV at 100 Hz, and fluorescence was recorded at 1 kHz from a single point on the cell membrane (Figure 2-4B). FlicR1 is an order of magnitude more stable to two-photon photobleaching compared to ASAP1 (Figure 2-4C) which enabled us to do point measurements. FlicR1 was fast and sensitive enough to resolve these voltage changes, though the signal amplitude was limited to ~2% per 200 mV at 100 Hz (Figure 2-4B). Due to rapid photobleaching under static two-photon illumination we did not pursue two-photon voltage imaging further. However, imaging with a beam that rapidly traces the contour of a cell membrane could ameliorate photobleaching and provide a viable option for further exploration (*202*).

2.2.3 Imaging and characterization of FlicR1 in cultured neurons

An important benchmark for a voltage indicator is to resolve single action potentials in single neurons with single-trial recording. Based on the characterization in HEK cells, we reasoned that the combination of the high fluorescence response and fast kinetics of the FlicR1 fluorescence

56

signal would allow it to record neuronal activity in single-trial recordings. To test this hypothesis, we transfected cultured hippocampal neurons with FlicR1 driven under the control of human synapsin I promoter.

FlicR1 labelled the plasma membrane both at the cell body and in individual dendrites (Figure 2-5A). It also showed intracellular puncta in the cell bodies similar to other cpmApple-derived indicators. When imaged at 100 Hz using a widefield fluorescence microscope with a 200 W lamp (0.2 W/cm^2 power fluence at sample), membrane-localized FlicR1 clearly reported spontaneous activity of the transfected neurons (Figure 2-5B and C) with a signal amplitude of $\Delta F/F = 4.3 \pm 0.6\%$ ($n = 7$) corresponding to a signal-to-noise ratio (SNR) of 9 ± 2 ($n = 7$).
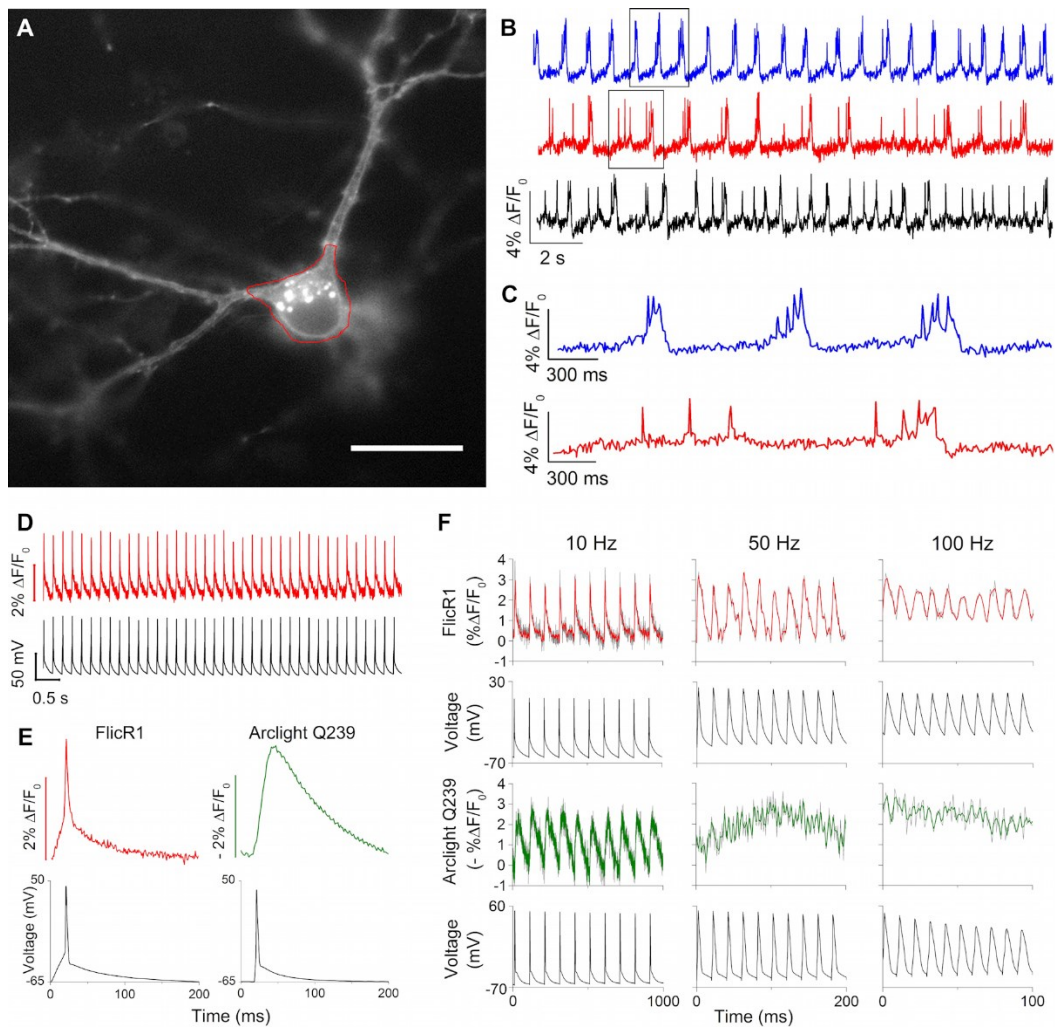
Figure 2-5 FlicR1 characterization in neurons. (A) Image of cultured hippocampal neuron expressing FlicR1. Scale bar 30 μm. (B) Detection of spontaneous activity waveforms in rat hippocampal neuron culture with FlicR1 indicator. Sample single-trial recordings of spontaneous action potential bursts from three neurons. Red trace from cell in (A). (C) Zoom in on regions marked in (B). (D) FlicR1 fluorescence response to 5 Hz stimulated action potential train using whole cell current clamp. (E) Mean fluorescence response of FlicR1 (left) and ArcLight Q239 (right). (F) FlicR1 (top) and ArcLight (bottom) response to 10, 50 and 100 Hz stimulated action potential trains using whole cell current clamp in neurons. Coloured traces are filtered with Savitzky-Golay smoothing (5 pts) and are overlaid over the grayscale unfiltered traces. All traces have

single exponential correction of bleach. For panels A-C fluorescence was recorded at 100 Hz frame rate and illumination intensity was 0.2 W/cm^2. For panels D-F fluorescence was acquired at 1 kHz frame rate and 10 W/cm^2 illumination intensity. Coloured traces in panels (D-F) are filtered with Savitzky-Golay smoothing (5 pts) for both FlicR1 and ArcLight Q239.

We next characterized the response of FlicR1 to action potentials in neurons. All measurements were performed at 22 °C at a frame rate of 1 kHz while illuminating with 10 W/cm^2 561 nm light. In whole cell current-clamp mode, we stimulated action potentials in neurons transfected with either FlicR1 or ArcLight Q293. FlicR1 faithfully reported single action potentials with a change in fluorescence of ΔF/F = 2.6 ± 0.8% (n = 7), averaging over the entire cell body (Figure 2-5D), corresponding to a SNR of 6 ± 1 (n = 7). ArcLight Q239 showed a similar fluorescence response amplitude to single action potentials (ΔF/F = −3.4 ± 0.9%, n = 5). However, because FlicR1 had faster kinetics than ArcLight, the fluorescence signal of FlicR1 more closely matched the electrical trace and was not broadened to the extent it was with ArcLight Q239 (Figure 2-5AE). To investigate FlicR1's ability to track high-frequency firing in neurons, we stimulated action potentials at frequencies from 5 Hz to 100 Hz (n = 7). FlicR1 reported voltage fluctuations of up to 100 Hz, clearly discriminating individual peaks in single trial recordings (Figure 2-5F). In contrast, ArcLight Q239 was not able to discriminate peaks at speeds higher than 10 Hz and only showed increased baseline

fluorescence (Figure 2-5F). We detected no significant differences in action potential amplitude (p = 0.16, two-tailed Student's t-test), membrane resistance (p = 0.67), or membrane capacitance (p = 0.21) between ArcLight Q239 (n = 6) and FlicR1 (n = 7) transfected cells.

2.2.4 Imaging brain slice activity with FlicR1

To test whether FlicR1 provides sufficient spatial and temporal resolution to report spontaneous activity in neuronal tissue, we expressed and imaged FlicR1 in organotypic rat brain slices. Organotypic rat hippocampal slices have been shown to maintain native hippocampal morphology and function and show spontaneous network activity (*203*). FlicR1 was delivered under human synapsin I promoter using *ex vivo* electroporation. To test the long-term effect of expression of FlicR1, hippocampal slices were cultured for 22-25 days (18-21 days post-transfection). Transfected neurons were clearly visible under wide-field epifluorescence imaging (Figure 2-6A, D). Wide-field epifluorescence imaging of FlicR1 successfully reported spontaneous activity of transfected neurons in single trial optical recordings when excited with constant yellow light illumination using a 100 W mercury lamp (0.4 W/cm^2 power fluence at sample). A signal amplitude of ΔF/F = 4 ± 1% and a SNR of 8 ± 2 (n = 12 cells) was obtained when averaging over the whole cell body. This is compared to a signal amplitude of ΔF/F = 9 ± 2% (n = 12 cells) and a SNR of 8 ± 2 obtained by averaging multiple ROIs in dendritic regions (Figure 2-6B, C). We attribute the difference in signal amplitude to

the presence of unresponsive puncta in the cell bodies. We also used theophylline to pharmacologically excite FlicR1 transfected neurons in organotypic brain slices. Theophylline has been shown to evoke sustained rhythmic seizure-like activities in different neuronal networks including hippocampal neurons (*204*). Indeed, upon treatment with theophylline, FlicR1 successfully reported seizure-like voltage oscillations when imaged at 50 Hz using the same 100 W mercury lamp with a signal amplitude of $\Delta F/F = 9 \pm 2\%$ (*n* = 12 cells) which corresponds to a SNR of 14 ± 2 (*n* = 12) (Figure 2-6E).
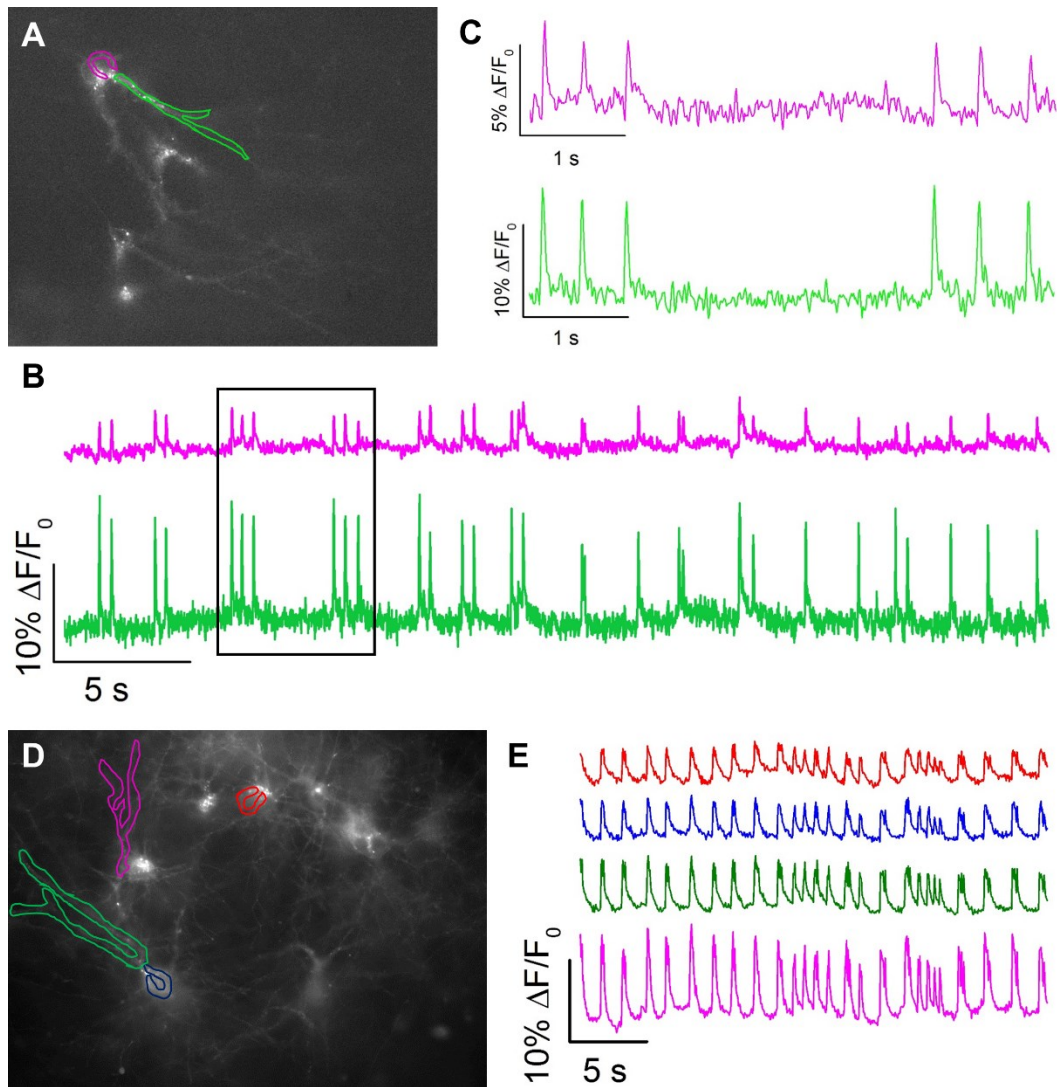
Figure 2-6 Detection of spontaneous activity and theophylline induced activity in rat hippocampal brain slice with FlicR1 indicator. (A) Fluorescence image of hippocampal brain slice transfected with FlicR1 and imaged 21 days post-transfection. Neuron processes are clearly labeled with FlicR1. Both cell bodies and processes show some fluorescence puncta. (B) Single trial fluorescence traces of activity in neuron cell bodies and neuron processes imaged with FlicR1. The traces correspond to the regions in the image marked with the same colour. These traces are from wide-field fluorescence data acquired using a 100 W mercury lamp at 100 Hz imaging frequency. (C) Zoom in on traces in

(B) marked with black borderline. (D) Fluorescence image of hippocampal brain slice transfected with FlicR1 and imaged 18 days post-transfection. Neuron processes are clearly labeled with FlicR1. Both cell bodies and processes show some fluorescent puncta. (E) Fluorescence traces acquired at 50 Hz of theophylline-induced membrane depolarization in neuron cell bodies and neuron processes imaged FlicR1. The traces correspond to the regions in the image marked with the same colour. All fluorescence traces are bleach corrected and traces in (B) and (C) are filtered with Savitzky-Golay smoothing (5 pts). Fluorescence traces were recorded at 100 Hz (A-C) and 50Hz (D-E) frame rate. Illumination intensity was 0.4 W/cm^2.

2.2.5 All optical electrophysiology with FlicR1

Next, we explored the utility of FlicR1 as a voltage indicator in an all-optical electrophysiology setup. One advantage of a red voltage indicator is its orthogonal spectrum to blue-light excitable channelrhodopsin actuators, suggesting a pairing of FlicR1 with a blue-light excitable channelrhodopsin for all-optical electrophysiology. As a proof of concept experiment, we co-transfected HeLa cells with FlicR1 and the channel rhodopsin variant ChIEF (*205*). Both FlicR1 and ChIEF showed high expression and good membrane trafficking when expressed in HeLa cells (Figure 2-7A and B). FlicR1 successfully reported blue-light (405 nm, 20 mW/cm^2) stimulated depolarization of HeLa cells with a fluorescence change of $\Delta F/F = 6.1 \pm 0.7\%$ ($n = 8$) (Figure 2-7D and E). As expected, at the image acquisition rate of 100 Hz, FlicR1 did not show any delay in response to the blue light stimulation of ChIEF. Although FlicR1 is based

on mApple, the same FP backbone as R-GECO1 Ca^{2+} indicator which shows blue light photoactivation (*198*) (Figure 2-7G-K), control cells transfected with FlicR1 alone showed no photoactivation with the 20 mW/cm^2 405 nm blue light used to stimulate HeLa cells (Figure 2-7C and F).
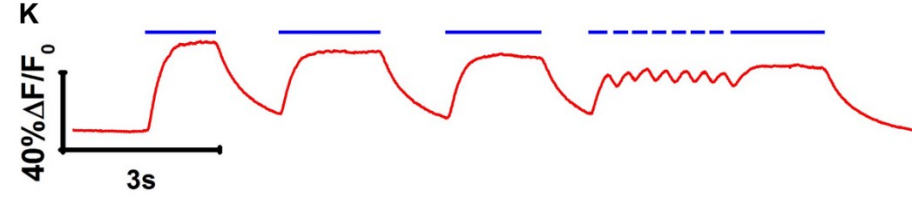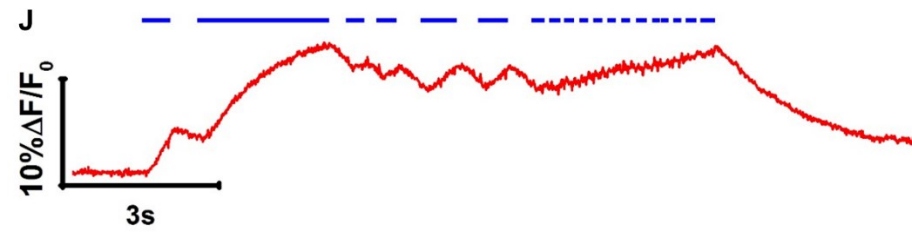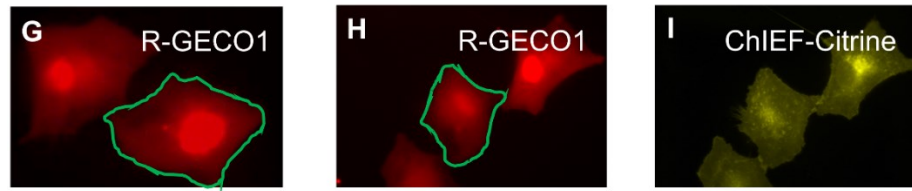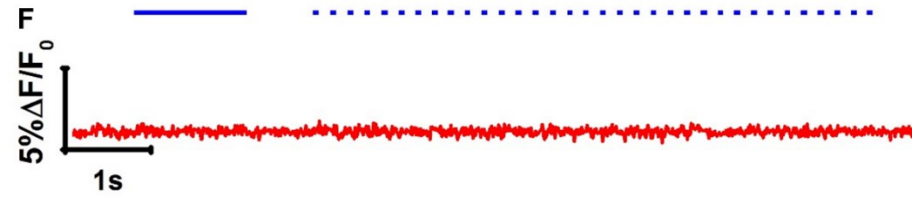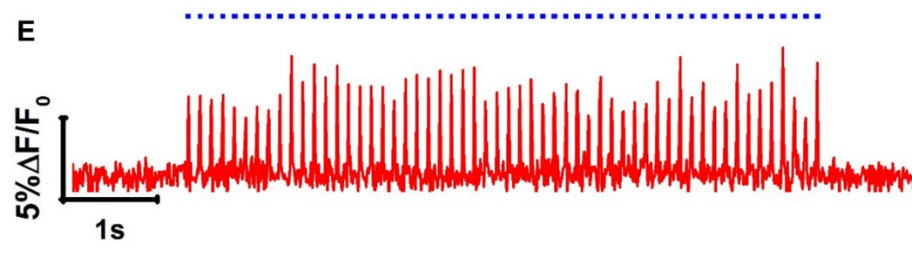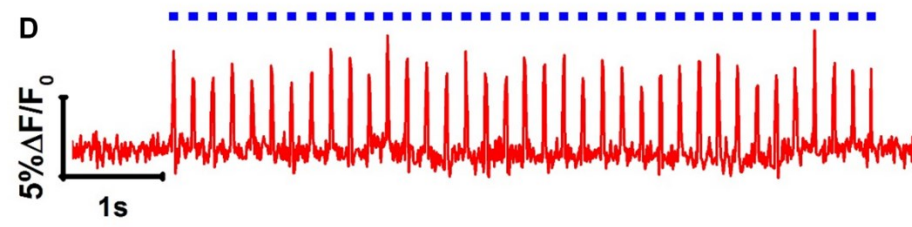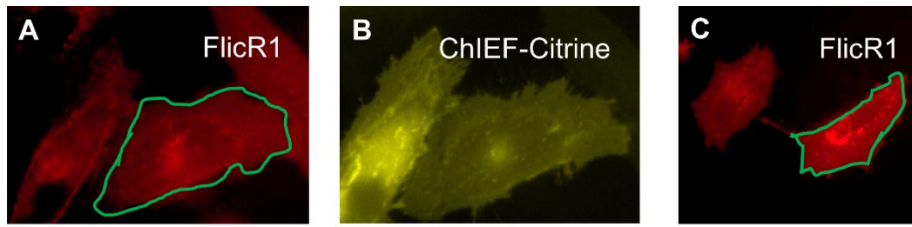
Figure 2-7 All optical electrophysiology with FlicR1 indicator in mammalian cells and comparison with R-GECO1 photoactivation. (A-B) Image of HeLa cells co-expressing FlicR1 (A) and ChIEF-Citrine (B). (C) Image of HeLa cells expressing FlicR1 only. (D) Fluorescence trace of FlicR1 in HeLa cells activated by 5 Hz stimulation of ChIEF using 405 nm laser pulses. Trace from cell in (A). (E) Fluorescence trace of FlicR1 in HeLa cells activated by 10 Hz stimulation of ChIEF using 405 nm laser pulses. Trace from cell in (A). (F) Control fluorescence trace for FlicR1 in HeLa cells using 405 nm laser pulses without co-expression of ChIEF. Trace from cell in (C). (G) Image of HeLa cells expressing R-GECO1 only. (H-I) Image of HeLa cells co-expressing R-GECO1 (H) and ChIEF-Citrine (I). (J) Control fluorescence trace for R-GECO1 in HeLa cells using 405 nm laser pulses. Trace from cell in (G). (K) Fluorescence trace of R-GECO1 in HeLa cells activated by stimulation of ChIEF using 405 nm laser pulses. Trace from cell in (H). Fluorescence traces were recorded at 100 Hz. The intensity of yellow light used to image FlicR1 and R-GECO1 was 60 mW/cm^2. 405 nm laser intensity to activate ChIEF was 20 mW/cm^2 in all experiments.

Although we were encouraged by these results, the 405 nm light intensity in our proof of concept experiment was 10-fold smaller than the light intensities necessary to reliably induce action potentials in cultured hippocampal neurons with most commonly used channelrhodopsin actuators (*206*). We therefore characterized the response of FlicR1 under blue light illumination conditions comparable to those necessary for neuronal experiments. We transfected HEK cells with FlicR1 and monitored their fluorescence with a 100 Hz imaging rate under 10 W/cm^2 561 nm illumination while using whole-cell patch clamp to vary the

membrane voltage for three cycles between -100 to +50 mV. For the third

cycle, we also illuminated the cell with 208 mW/cm^2 458 nm light. The

fluorescence traces showed significant photoactivation of FlicR1 by the

blue light and a simultaneous decrease in voltage sensitivity. We also

repeated the measurement with 25 mW/cm^2 405 nm light and observed a

similar photoactivation effect in one of four runs. These results indicated

that under the blue light illumination conditions necessary to drive action

potentials with channelrhodopsin actuators, photoactivation of FlicR1

could still present a challenge. Nevertheless, we attempted to use FlicR1

for all-optical electrophysiology in neurons. We cotransfected cultured rat

hippocampal neurons with FlicR1 and TsChR, a blue-shifted

channelrhodopsin (*207*), and attempted to elicit action potentials with blue

light illumination while monitoring FlicR1 fluorescence. We found that

illumination pulses of 10 to 1000 ms at 5 to 210 mW/cm^2 for both 458 nm

and 488 nm light (data not shown) caused sufficient photoactivation of

FlicR1 to obscure its voltage response. This is in contrast to HeLa cells in

which 20 mW/cm^2 of 405 nm light did not cause photoactivation. We

suspect that the difference between neurons and HeLa cells is attributable

to intracellular puncta that are present in neurons but absent in HeLa cells.

These puncta represent a large pool of protein that does not contribute to

the voltage sensitive response, yet can undergo photoactivation.

To circumvent photoactivation of FlicR1 in neurons, we used a digital

micromirror device (Figure 2-8A) to spatially target 488 nm illumination

pulses (5 mW/cm^2 to 1.7 W/cm^2, 10 or 50 ms duration) to the neuronal processes of cells coexpressing FlicR1 and either ChR2-H134R, TsChR, or PsChR (*197*), another blue-shifted channelrhodopsin, while avoiding blue illumination of the soma. We illuminated the whole cell with 561 nm light at 10 W/cm^2 and collected FlicR1 fluorescence from the soma. We used simultaneous manual patch clamp in current-clamp mode to provide independent detection of action potentials. When blue illumination was excluded from the soma, cells coexpressing FlicR1 and ChR2-H134R did not produce sufficient photocurrents to induce action potentials under any illumination parameters, consistent with previous reports (*190*). In a neuron expressing both FlicR1 and PsChR, FlicR1 could report optically-induced action potentials with similar signal-to-noise ratio as electrically-induced action potentials (Figure 2-8B and C). The 561 nm illumination used for eliciting FlicR1 fluorescence depolarized the cell by 14 mV (Figure 2-8D), but did not induce action potentials on its own. This result suggests that FlicR1 could be used for all-optical electrophysiology under appropriate expression conditions.
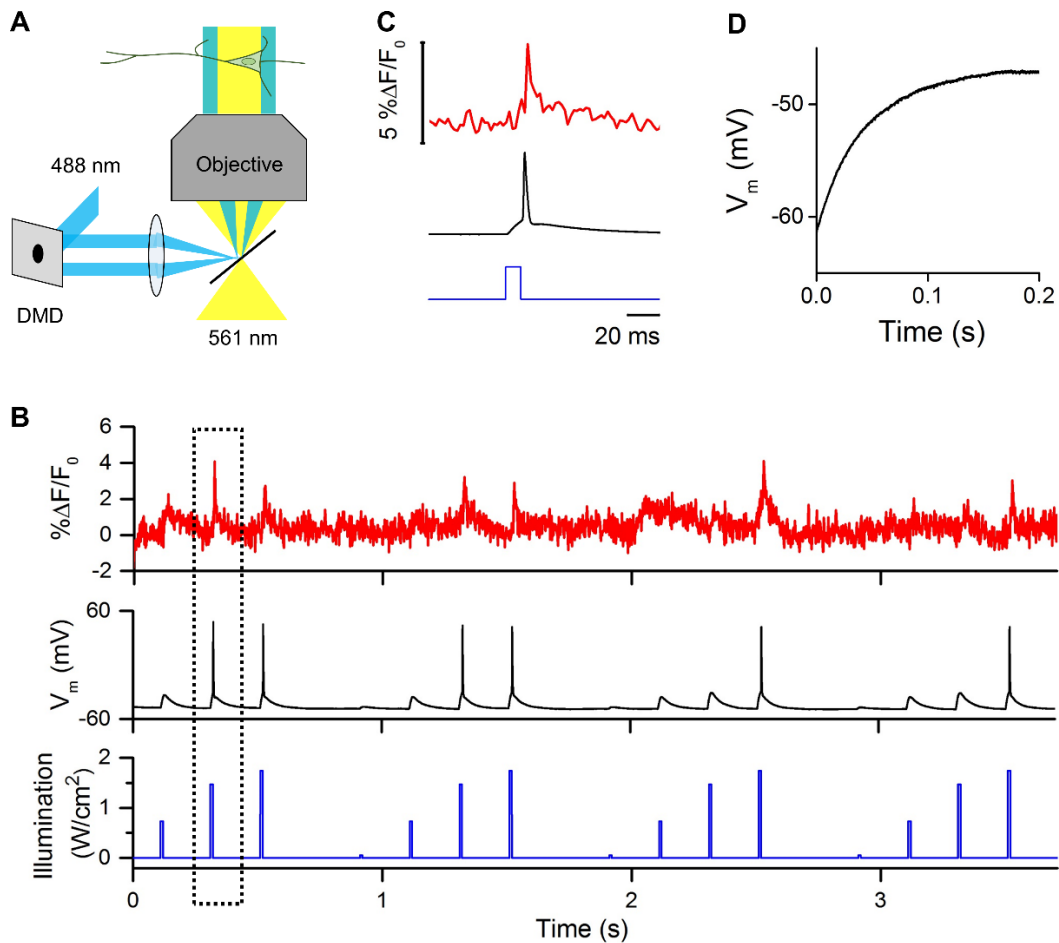
Figure 2-8 All optical electrophysiology using FlicR1 in cultured hippocampal neurons. (A) Diagram showing experimental setup using a digital micromirror device (DMD) to target the blue light to the neuronal processes. (B) Red: FlicR1 fluorescence readout from single-trial optical recording of single action potentials initiated by pulses of blue light illumination using the experimental setup shown in (A). Yellow illumination to image FlicR1 was 10 W/cm^2. Black: Patch recording. Blue: 488 nm illumination (10 ms, 0.5-2 W/cm^2). (C) Zoom in on traces in (B) marked with black borderline. (D) Patch clamp recording of neuron expressing PsChR when exposed to 561 nm laser (10 W/cm^2). This illumination depolarized the cell by 14 mV, but did not induce action potentials on its own. All fluorescence traces are bleach corrected. Fluorescence trace

collected at a frame rate of 500 Hz using an EMCCD camera. Fluorescence trace in (C) is filtered with Savitzky-Golay smoothing (5 pts).

2.3 Conclusion

FlicR1 is a red indicator with performance comparable to state-of-the-art green voltage indicators like ASAP1 and ArcLight. FlicR1 was designed with the rationale that fusion of a cpRFP to a VSD would maximize the chance of coupling voltage-induced conformational changes to the FP chromophore, leading to a large response amplitude and fast kinetics. Indeed, the large and fast response of FlicR1 indicates that the S4 movement rapidly changes the environment around the mApple chromophore. In contrast to ASAP1, FlicR1 has the cpFP linked to the end of the S4 helix. Fusion to the end of the S4 helix bestows FlicR1 with a fluorescence voltage response that is dominated by a fast component (~ 3 ms) for both on and off kinetics (90% on and 78% off) at room temperature. Although ASAP1 has slightly faster kinetics (~ 2 ms) (*15*), the fast component of the FlicR1 response has ~1.5-fold and ~2-fold increased weight for on and off, respectively, compared to ASAP1 (60% on and 43% off). The comparable responses to single action potentials for both ASAP1 and FlicR1 is consistent with this increased weight of the fast component, because a greater fraction of the full FlicR1 response amplitude is utilized to report neuronal activity.

Our screening strategy was crucial to engineer FlicR1 to be a fast, bright, voltage indicator with large response amplitude. Simply fusing the

cpRFP resulted in a dim indicator that had a small response amplitude to voltage changes. Other reports of manually inserting cpFPs to the C-terminus of CiVSD resulted in indicators with low response amplitude (*181*, *182*) and/or slow kinetics (*182*). Only through the use of our screening strategy did we discover variants that are both bright and highly responsive to membrane potential changes.

One of the most intriguing mutations that resulted from random mutagenesis is Val207Ala, located in the S3 to S4 linker of the CiVSD. Subsequent randomization of this position led to the discovery of the further beneficial Val207Phe substitution. We initially reasoned that this mutation must be important for modulating the voltage sensitivity of FlicR1. The recently reported X-ray crystal structures of CiVSD in both the activated and resting state (*199*) show that this residue is part of an alpha helix that unwinds when the VSD is in the activated (depolarized) state. Based on this insight, we suggest that this mutation might be increasing the rate and/or extent with which the S4 helix moves, and therefore improving FlicR1's response to membrane depolarization.

We showed that FlicR1 traffics well to the cell membrane in neurons and is suitable for long-term expression in organotypic slices. However some fraction of the protein resides in intracellular puncta when expressed in neurons. We believe these puncta are due to the Anthozoa-derived mApple FP body of FlicR1, as related FPs often form intracellular puncta in neurons (*78*). These puncta however did not interfere with long term

expression of FlicR1 in organotypic slices. After three weeks of FlicR1 expression, neurons in organotypic slices showed spontaneous activity and responded to stimulation as expected. FlicR1 was ~30-fold brighter when compared to Archaerhodopsin-based voltage indicators, requiring only ~10 W/cm^2 to image neural activity compared to ~300 W/cm^2 for the recently reported QuasAr2 (*190*).

In conclusion, FlicR1's fast responses to single action potentials and ability to track high-frequency trains makes it an excellent sensor for action potential detection in rapid firing events. FlicR1's red fluorescence allows for all optical electrophysiology together with blue–light excitable channelrhodopsins under illumination conditions carefully tuned to minimize optical crosstalk. Finally, FlicR1 is likely to be useful in combination with a wide variety of green fluorescent indicators, though this has not yet been demonstrated and will require crosstalk mitigation depending on the experimental setup and green indicator used.

2.4 Materials and methods

Molecular biology to construct FlicR variants. Polymerase chain reaction (PCR) amplification was used to construct the DNA template for FlicR. Synthetic oligonucleotides (Integrated DNA Technologies) were used as primers for amplification and Pfu polymerase (Thermo Fisher Scientific) was used to maintain high fidelity DNA replication. Overlap PCR was used to link CiVSD to cpmApple FP. Random mutagenesis was performed with error-prone PCR amplification using Taq polymerase (New

England Biolabs) in the presence of $MnCl_2$ (0.1 mM) and 800 µM excess dTTP and dCTP. Randomization of targeted codons was performed with QuikChange Lightning kits (Agilent Technologies). Restriction endonucleases (Thermo Fisher Scientific) were used to digest PCR products and expression vectors. Agarose gel electrophoresis was used to purify DNA products from PCR and restriction digestion reactions. The DNA was extracted from the gels using the GeneJET gel extraction kit (Thermo Fisher Scientific). Ligations were performed using T4 DNA ligase (Thermo Fisher Scientific).

DNA encoding the first 242 amino acids from CiVSD (VSD242) was generated by PCR amplification of CiVSD domain from the voltage sensor VSFP3.1 (*183*) using forward primer (FW-BamHI-VSD) and reverse primer (RV-cpmApple-VSD242). DNA encoding the cpmApple variant was generated by PCR amplification of gene encoding R-GECO1 using forward primer (FW-VSD242-cpmApple) and reverse primer (RV-XbaI-cpmApple). Primers RV-cpmApple-VSD242 and FW-VSD242-cpmApple contain an overlap region that was used to join these two genes together by overlap PCR. Primers RV-cpmApple-VSD242 and FW-VSD242-cpmApple also contained two fully randomized codons (NNK codons) that link the two genes together generating 1024 variants. The length of the VSD amplified by PCR was varied (VSD 236, VSD237, VSD238, VSD239, VSD240 and VSD241). Other sets of overlap primers along with FW-BamHI-VSD primer and RV-XbaI-cpmApple primer were used to link DNA

encoding cpmApple to the shorter VSDs as outlined above for VSD242. This led to a library of 1024 FlicR variants for each length of VSD.

Error-prone PCR together with DNA shuffling were used to construct libraries in the following rounds of directed evolution on FlicR variants from VSD239 library. PCR products were purified by agarose gel electrophoresis, digested, and ligated into a modified pcDNA3.1(+) vector as described below.

Plasmid for dual *E. coli* and mammalian cell expression. A vector for expression in prokaryotic and eukaryotic systems was constructed based on mammalian expression vector pcDNA3.1(+). To facilitate prokaryotic expression, an *E. coli* ribosome binding site (aggaggaa) for prokaryotic translation was introduced using a Quikchange reaction (Agilent Technologies). We named the resulting vector pcDuEx0.5. The transcription of the encoded genes relies on the weak activity of the cytomegalovirus (CMV) promoter in *E. coli* cells (*208*). pcDuEx0.5 exhibited moderate expression of FlicR variants in *E. coli* cells, and showed comparable expression levels in HeLa cells compared to the original pcDNA3.1(+). We used pcDuEx0.5 as the vector for screening of FlicR libraries. Other dual expression vectors have been developed previously (*209*).

Plasmid for neuronal expression. To express FlicR1 in neurons, FlicR1 was cloned from plasmid pcDuEx0.5 into the *BamHI*/*HindIII* sites of an AAV2 vector using F-VSD-BamHI and R-HindIII-cpmApple primers.

FlicR1 expression was controlled using human synapsin I promoter to preferentially express in neurons. A 3' Woodchuck Hepatitis Virus Posttranscriptional Regulatory Element (WPRE) sequence was used to enhance expression. For channelrhodopsin expression, a TsChR-TS-EGFP fusion was cloned into the same plasmid, where TS represents a KiR2.1 trafficking sequence used to improve membrane trafficking of channelrhodopsins. The amino acid sequence of the TS sequence is KSRITSEGEYIPLDQIDINV. ChR2(H134R)-EGFP was expressed from a lentiviral construct under a CamKII promoter described previously (*190*).

Screening of FlicR library variants in *E. coli*. Gene libraries of FlicR variants were transformed into electro-competent *E. coli* strain DH10B (Invitrogen). *E. coli* cells were then plated and cultured at 37 °C on LB agar plates supplemented with ampicillin (400 µg/ml) to obtain 500-1000 colonies per plate. Colonies were then imaged using a custom imaging setup described previously (*200*). To screen for FlicR mutant brightness, plate images were acquired using a 560/40 nm excitation filter and 630/60 nm emission filter. For each round of random mutagenesis, ~10,000 colonies (10-20 plates) were screened. For each library generated by codon randomization, ~3 times more colonies than the expected randomization library size were screened. Colonies with the top 0.01% fluorescence brightness were manually picked and cultured in 4 ml LB media supplemented with ampicillin (100 µg/ml). Plasmids were then extracted using GeneJET plasmid miniprep kit (Thermo Fisher Scientific).

Expression and *in vitro* spectroscopic characterization of FlicR1.

To purify FlicR1, the pcDuEx0.5 plasmid harboring FlicR1 was used to transform electro-competent *E. coli* DH10B cells (Invitrogen). The *E. coli* were grown on LB agar plates supplemented with ampicillin (400 µg/ml). A colony was used to inoculate 8 ml of LB liquid medium (100 µg/ml ampicillin) and grown overnight at 37 °C. The next day, the 8 ml of bacterial culture was added to 500 ml of LB medium (100 µg/ml ampicillin) and grown for 4 hours at 37 °C then grown for 48 hours at 25 °C. The cell pellets were then collected by centrifugation and lysed by suspension in B-PER solution (Pierce). The insoluble fraction (containing the membrane proteins) was collected after centrifugation and resuspended in a solution of 2% *n*-dodecyl-β-D-maltopyranoside (Anatrace) in Tris-buffered saline (TBS). The suspension was then homogenized by an ultrasonic homogenizer and centrifuged at 4 °C. Solubilized FlicR1 protein in the supernatant was used to measure the fluorescence spectrum on a Safire2 plate reader (Tecan) and the absorbance spectrum on a DU-800 UV-visible spectrophotometer (Beckman).

Cell culture. HeLa cells (ATCC, CCL-2) were cultured in Dulbecco's modified Eagle's medium (DMEM) (supplemented with 10% fetal bovine serum (FBS) (Sigma), 2 mM GlutaMax (Invitrogen), penicillin-G potassium salt (50 units/ml), and streptomycin sulfate (50 µg/ml)) and the cells were incubated for 48 h at 37 °C, 5% CO_2. Cells were split and cultured on collagen-coated 35 mm glass bottom dishes (Matsunami) to ~50%

confluency. Transfection was performed by incubating HeLa cells with the mixture of 1 µg of plasmid DNA and 2 µL of Turbofect (Thermo Fisher Scientific) for 2 h following the manufacturer's instructions. Imaging was performed 24-48 hours after transfection.

HEK293T cells (ATCC CRL-11268) were cultured and transfected following standard protocols (*189*). Briefly, HEK293T cells were grown at 37 °C, 5% CO_2, in DMEM supplemented with 10% FBS and penicillin-G potassium salt (50 units/ml), and streptomycin sulfate (50 µg/ml). Cells were transfected with 400 ng DNA using Transit 293T (Mirus) following the manufacturer's instructions. After 24 hours cells were re-plated onto glass-bottom dishes (In Vitro Scientific, D35-20-1.5-N) coated with matrigel (BD biosciences) at ~10,000 cells/cm^2. Measurements were performed 48 hours after transfection.

Rat hippocampal neurons. Rat glial monolayers were prepared similarly to Ref. (*210*). Briefly, dissociated hippocampal cells from P0 rat pups of either sex (Sprague Dawley, Tocris) (*211*) were plated on a 10 cm culture dish in glial medium (GM), comprised of 15% FBS (Life Technologies), 0.4% (w/v) D-glucose, 1% glutamax (Life Technologies), 1% penicillin/streptomycin (Life Technologies) in MEM (Life Technologies). After reaching confluence, cells were re-plated onto glass-bottomed dishes (In Vitro Scientific, D35-20-1.5-N) coated with matrigel (BD biosciences) at a density of (3500 cells/cm^2). When the glial monolayers reached confluence again, the medium was replaced by GM

77

with 2 µM cytarabine (cytosine-β-arabinofuranoside, Sigma). Dishes were maintained in GM with 2 µM cytarabine until use.

Hippocampi dissected from P0 rat pups were dissociated using papain and plated in plating medium (PM) at 8,000 cells/cm^2 on the pre-established glial monolayers (*211*). At one day *in vitro* (DIV), PM was exchanged for 2 µM cytarabine in neurobasal-based medium (NBActiv4, Brainbits llc.). Neurons were subsequently fed every five days by replacing 1 ml of culture media with NBActiv4 without cytarabine. Neurons were transfected on DIV 9 via calcium phosphate as described in Ref. (*212*). Measurements on neurons were performed on DIV 14. For all-optical electrophysiology experiments in neurons, cells were cotransfected by calcium phosphate with channelrhodopsin and FlicR1 DNA on DIV9 and measured on DIV 12-13.

For measurements of spontaneous activity, dissociated E18 Sprague Dawley Hippocampal Cells in Hibernate® EB Complete Media were purchased from BrainBits LLC. The cells were grown on 35 mm glass bottom dish (In Vitro Scientific) coated with poly-D-lysine (EMD Millipore, A-003-E) containing 2 ml of NbActiv4 (BrainBits LLC) supplemented with 2% FBS, penicillin-G potassium salt (25 units/ml), and streptomycin sulfate (25 µg/ml). Half of the culture media was replaced every 3 days. Neuronal cells were transfected on day 8 using Lipofectamine 2000 (Life Technologies) following the manufacturer instructions. Briefly, 1-2 µg of plasmid DNA and 4 µL of Lipofectamine 2000 (Life Technologies) were

78

added to 100 µl of NbActive4 medium to make the transfection medium. This medium was then incubated at room temperature for 10-15 minutes. Half of the culture medium (1 ml) from each neuron dish was taken out and combined together with an equal volume of fresh NbActiv4 medium (supplemented with 2% FBS, penicillin-G potassium salt (25 units/ml), and streptomycin sulfate (25 µg/ml)) to make a 1:1 mixture and incubated at 37 °C and 5% CO_2. 1 ml of fresh conditioned (at 37 °C and 5% CO_2) NbActiv4 medium was then added to each neuron dish. The transfection medium was then added and the neuron dishes were incubated for 2-3 hours at 37 °C in a CO_2 incubator. The media was then replaced using the conditioned 1:1 medium prepared previously. The cells were incubated for 48-72 hours at 37 °C in a CO_2 incubator before imaging.

Induced transmembrane voltage (ITV) screening. FlicR variants were co-expressed in HeLa cells, together with the inward rectifier potassium channel, Kir2.1 (Addgene: 32641), and ArcLight Q239 (Addgene: 36856) as an internal reference. Expression of Kir2.1 in HeLa cells helped maintain the resting potential around -60 mV, which is appropriate for screening neuronal voltage indicators. A uniform electric field of ~50 V/cm was applied across the cell culture to create an ITV. A pulse generator (PG 58A, Gould Advance Ltd.) was used to apply a 10 ms square-wave pulse at ~0.5 Hz. An amplifier (6824A 40V/25A HP/Agilent) was used to obtain a pulse amplitude of 25 V. A pair of parallel platinum electrodes (0.5 cm apart) were used to deliver the pulses to the cell

culture. Fluorescence was imaged simultaneously with multiple electric field pulses for ITV at a frame rate of a 100 Hz for 10 seconds.

Imaging ITV in HeLa cells. Imaging was carried out in HEPES (25 mM) buffered Hanks' Balanced Salt Solution (HBSS). An inverted fluorescence microscope (Eclipse Ti-E, Nikon) equipped with a 200 W metal halide lamp (PRIOR Lumen) and a 60× oil objective was used to image HeLa cells. Images were acquired at 100 Hz with 4×4 binning using a 16-bit QuantEM 512SC electron-multiplying CCD camera (Photometrics). A FITC/Cy2 filter set (470/40 nm (excitation), 525/50 nm (emission), and a 495LP dichroic mirror (set number 49002, Chroma)) was used to image ArcLight Q239. A TRITC/Cy3 filter set (545/30 nm (excitation), 620/60 nm (emission), and a 570LP dichroic mirror (set number 49005, Chroma)) was used to image FlicR1. The NIS Elements Advanced Research software (Nikon) was used to control the microscope and camera. The raw fluorescence traces of both FlicR and ArcLight were extracted from identical regions of interest in cells expressing both constructs, and exported into a customized Microsoft Excel spreadsheet. Background subtraction, photobleaching corrections, calculations of average $\Delta F/F_{min}$, and calculation of SNRs were performed automatically in Excel. The average $\Delta F/F_{min}$ and SNR of FlicR signals were compared to those of ArcLight signals from the same cells, and the ratios of $\Delta F/F_{min}$ of FlicR vs. ArcLight were reported. At least 10 cells co-expressing FlicR and

ArcLight were analyzed for each variant. The best variant with maximum mean ratio in each library was determined and sequenced.

Imaging spontaneous activity in primary neuron culture. Imaging was carried out in HEPES (25 mM) buffered HBSS. Widefield imaging was performed on an inverted Nikon Eclipse Ti-E microscope equipped with a 200 W metal halide lamp (PRIOR Lumen), 60× oil objectives (NA = 1.4, Nikon), and a 16-bit QuantEM 512SC electron-multiplying CCD camera (Photometrics). A TRITC/Cy3 filter set (545/30 nm (excitation), 620/60 nm (emission), and a 570LP dichroic mirror, set number 49005, Chroma) was used to image FlicR1. For time-lapse imaging, neurons were imaged at 100 Hz imaging frequency with 4×4 binning. Raw fluorescence traces were corrected for background autofluorescence and photobleaching. As seen in Figure 2-5A, FlicR1 shows some intracellular puncta. Mounting evidence points to these structures being lysosomes in which the protein is accumulating faster than it is being degraded (*213*).

Simultaneous electrophysiology and fluorescence in HEK cells and primary neuron culture. All imaging and electrophysiology measurements were performed in Tyrode buffer (containing, in mM: 125 NaCl, 2.5 KCl, 3 CaCl$_2$, 1 MgCl$_2$, 15 HEPES, 30 glucose pH 7.3). For HEK cell measurements, 2-aminoethoxydiphenyl borate (100 μM, Sigma) was added to block endogenous gap junctions. Measurements at 34 °C were carried out by perfusing in Tyrode buffer at 1 ml/min, while maintaining

elevated temperature with an in-line heater (Warner) and an objective heater (Bioptechs).

Filamented glass micropipettes (WPI) were pulled to a tip resistance of 4–8 MΩ, and filled with internal solution containing 125 mM potassium gluconate, 8 mM NaCl, 0.6 mM $MgCl_2$, 0.1 mM $CaCl_2$, 1 mM EGTA, 10 mM HEPES, 4 mM Mg-ATP, 0.4 mM Na-GTP (pH 7.3); adjusted to 295 mOsm with sucrose. Pipettes were positioned with a Sutter MP285 manipulator. Whole-cell, voltage and current clamp recordings were acquired using an Axopatch 700B amplifier (Molecular Devices), filtered at 2 kHz with the internal Bessel filter and digitized with a National Instruments PCIE-6323 acquisition board at 10 kHz. Data was only acquired from cells with access resistance < 25 MΩ. To determine the minimal current injection necessary for action potential generation before imaging, square waves of increasing amplitudes were injected in step sizes of 50-100 pA while recording the voltage. The minimal current value that resulted in robust AP generation was used to generate action potentials for imaging experiments.

Illumination light was provided by a 561 nm 100 mW diode-pumped solid-state laser (Cobolt Jive 100 561 nm) for FlicR1 imaging and by a 488 nm 50 mW laser (Omicron PhoxX) for ArcLight imaging. The beam was expanded and focused onto the back-focal plane of a 60× oil immersion objective (Olympus APON 60XOTIRF 1.49 NA). The imaging intensity at the sample was 10 W/cm^2. For all-optical electrophysiology measurements

82

in neurons, the 488 nm beam was expanded and modulated by a digital micromirror device (Texas Instruments DLP LightCrafter Evaluation Module) controlled using built-in software. FlicR1 fluorescence was separated from excitation light and filtered using the dichroic and emission filters from a Cy3-4040C-OMF-ZERO filter set (Semrock). ArcLight fluorescence was separated with a long pass dichroic (Semrock FF495-Di03) and filtered with a 531/40 nm bandpass filter (Semrock FF01-531/40-25). The sample was imaged onto an EMCCD camera (Andor iXon$^+$ DU-860) with 128×128 pixels. For measurements of FlicR1's speed, movies were acquired at a 2 kHz framerate with 2×2 binning. Sensitivity measurements were acquired at 10 Hz with no binning. Photobleaching traces were acquired at 2 Hz with no binning. Neuronal data was acquired at 1 kHz with 2×2 binning or at 500 Hz with 1×1 binning.

Some of the screening of all-optical electrophysiology conditions was performed on another custom built microscope equipped with a higher resolution camera. Illumination light was provided by a 561 nm 100 mW Cobolt Jive (part #0561-04-01-0100-500), a 488 nm 100 mW Coherent Obis (part #1226419), or a 405 nm 30 mW Dragon Laser (part #11042443). Laser lines were combined with dichroic mirrors and intensities were modulated using acousto-optical tunable filters (Gooch & Housego, part #TF525-250-6-3-GH18A or #48058-2.5-.55-5W). The 488 nm laser line was expanded to illuminate the chip of a digital micromirror device (Texas Instruments DLP LightCrafter with DLP 0.3 WVGA chipset)

which was subsequently reimaged onto the sample plane. The 561 nm and 488 nm lines were focused at the back focal plane of an APON 60XOTIRF 1.49 NA objective (Olympus). Collimated 405 nm laser light at the back focal plane of the objective was defocused to obtain a 5 μm spot at the sample and was guided at the sample plane using galvonometric mirrors (Thorlabs GVS202) located in a conjugate plane. Fluorescence light was separated from illumination light using a quadband dichroic mirror (Semrock part #Di01-R405/488/561/635). The fluorescence light was passed through a knife-edge, split into two channels using a dichroic mirror which were recombined and reimaged onto two halves of the chip of a scientific CMOS camera (Hamamatsu ORCA-Flash 4.0). The splitting and recombining were accomplished using dichroic mirrors (Semrock FF662-FDi01). Green and orange fluorescence was filtered using a HQ550/50m bandpass filter (Chroma) for 488 nm excitation, or an ET595/50m bandpass filter (Chroma) for 561 nm illumination. 458 nm illumination light was provided by an LED (LED Supply 07040-PR000-B) positioned above the sample filtered by a D480/60 excitation filter (Chroma) and controlled by a four-channel LED driver (Thorlabs DC4104). Electrophysiological recordings on this microscope were performed as above, but using an Axopatch 200B amplifier and CV203BU headstage (Molecular Devices). Signals were filtered at 5 kHz with the internal Bessel filter and digitized at 10 kHz using a National Instruments PCIe-6259 acquisition board.

Measurements on ArcLightQ239 kinetics were performed using 488 nm illumination light from a Coherent Obis 488-50 laser focused onto the back focal plane of a 60× water immersion objective, numerical aperture 1.20 (Olympus UIS2 UPlanSApo 60×/1.20 W) to a power fluence of 2-4 W/cm^2 at the sample. Fluorescence light was split from the excitation light using a Semrock Di01-R405/488/594 dichroic, passed through a 525/30 bandpass emission filter, and imaged onto a scientific CMOS camera (Hamamatsu ORCA-Flash 4.0). Whole-cell voltage recordings were performed with a patch clamp amplifier (A-M Systems, Model 2400), filtered at 5 kHz with the internal filter and digitized with a National Instruments PCIE-6323 acquisition board at 10 kHz.

FlicR's two-photon voltage sensitivity was tested on a homebuilt beam-scanning two-photon microscope with an 80 MHz, 100 fs tunable pulsed laser (SpectraPhysics Insight DeepSee). Measurements were performed at 1120 nm excitation wavelength with a time-averaged excitation power of 60 mW, or 0.8 nJ per pulse, in imaging mode, and ~ 6 mW or 80 pJ per pulse in point-recording mode. Pulses were focused down to a ~500 nm spot with a 1.2 NA water immersion objective (Olympus UplanSapo); Imaging measurements were performed with linear scan speeds of ~8 cm s^{-1}. Excitation light and fluorescence were separated using a FF775-Di01 dichroic mirror and FF01-790/SP-25 shortpass filter (Both Semrock); fluorescence was detected using a Hamamatsu R943-02 photomultiplier tube in photon counting mode,

cooled to -20 °C. The PMT signal was amplified through an SRS PR325 amplifier and discretized with a Hamamatsu Photon counting unit C9744. Data were acquired using an NI pci-6259 DAQ card. The setup was controlled by Labview software written in-house.

HeLa cell all optical electrophysiology. Imaging was carried out in HEPES (25 mM) buffered HBSS. An inverted fluorescence microscope (Eclipse Ti-E, Nikon) equipped with a 200 W metal halide lamp (PRIOR Lumen) and a 60× oil objective was used. Images were acquired at 100 Hz with 4×4 binning using a 16-bit QuantEM 512SC electron-multiplying CCD camera (Photometrics). Cells expressing R-GECO1 only, R-GECO1 and ChIEF-Citrine, FlicR1 only, FlicR1 and ChIEF-Citrine, were exposed to whole-field illumination with pulses of blue light (405 nm laser, 20 ms, 5 Hz and 10 Hz, 5 mW/mm^2) to stimulate ChIEF. Cells were simultaneously illuminated with yellow light to excite fluorescence of R-GECO1 or FlicR1. A TRITC/Cy3 filter set (545/30 nm (excitation), 620/60 nm (emission), and a 570LP dichroic mirror (set number 49005, Chroma)) was used to image R-GECO1 or FlicR1 fluorescence. The NIS Elements Advanced Research software (Nikon) was used to control the microscope and camera. Fluorescence changes were calculated by averaging over the whole cell. Raw fluorescence traces were corrected for background autofluorescence and photobleaching.

We explored the use of different opsins in an effort to minimize optical crosstalk with FlicR1. The yellow light intensity used to image FlicR1 in

HeLa cells at 100 Hz acquisition rate (60 mW/cm^2) is much lower than that required to image AP transients in neurons (10 W/cm^2). As mentioned above, we used ChIEF in our proof-of-concept experiments because 60 mW/cm^2 of yellow light is not enough to cause activation of ChIEF. However, we had to switch to more blue-shifted opsins (TsChR and PsChR) to try to avoid optical crosstalk with the relatively higher illumination intensity required to image FlicR1 in neurons at 1 kHz (Figure 2-8).

Preparation of rat hippocampal organotypic brain slices. Horizontal brain slices (250 µm thickness) from a 0-day-old (P0) Sprague Dawley rat of either sex were generated in ice-cold HBSS containing 1.3 mM CaCl$_2$ and 1 mM MgSO$_4$ with a vibrating microtome (Leica VT1000S, Leica Microsystems, Richmond Hill, ON, Canada) as described previously (*204*). All procedures were carried out in compliance with the guidelines of the Canadian Council for Animal Care and with the approval of the University of Alberta Animal Care and Use Committee for Health Science. Hippocampal regions were cut from horizontal brain slices and placed on a sterile 0.4 µm pore membrane cell culture insert (Millipore PICMORG50). The insert and slice were then placed in a Petri dish containing 1.5 ml of NbActiv4 (BrainBits) supplemented with 5% fetal bovine serum (FBS), penicillin-G potassium salt (50 units/ml), and streptomycin sulfate (50 µg/ml). Slices were cultured at 37 °C and 5% CO$_2$ for 3-5 days prior to transfection.

***Ex vivo* electroporation of organotypic brain slices.** The Millipore insert along with the slice cultured on it were placed between a platinum plate petri dish electrode (CUY700-P2E, Nepa Gene, Japan), and a square platinum electrode (CUY700-P2L, Nepa Gene, Japan). The gap between the dish electrode and the membrane was filled with electroporation buffer (HBSS with 1.5 mM $MgCl_2$ and 10 mM glucose). Plasmid pAAV2-hSyn-FlicR1 was dissolved in electroporation buffer at a concentration of 1 µg/µL and sufficient volume was added to fill the gap between the slice and the top electrode. Five 20 V pulses (5 ms each, 1 Hz) were applied using a function generator (PG 58A, Gould Advance Ltd.) and an amplifier (6824A HP/Agilent). The direction of electrical field was then reversed and a second set of five pulses with the same settings were applied. After transfection, the slices were returned to the incubator at 37 °C with 5% CO_2. It normally takes 2-3 days for full expression of FlicR1 in cultured brain slices using this transfection method.

Imaging of rat organotypic hippocampal slices. For organotypic brain slice imaging an upright FV1000 confocal microscope (Olympus Canada, Markham, ON, Canada) equipped with FluoView1000 software (Olympus Canada) and a 20× XLUMPlanF1 water immersion objective (NA = 1.00, Olympus) was used. Illumination light was provided by a 100 W mercury arc lamp (Olympus Canada).

The brain slice on the Millipore insert was placed in a custom-made chamber to hold it in place during imaging. Immediately prior to imaging,

88

the slices were perfused with artificial cerebrospinal fluid (ACSF) superfusate containing: 120 mM NaCl, 3 mM KCl, 1 mM $CaCl_2$, 2 mM $MgSO_4$, 26 mM $NaHCO_3$, 1.25 mM NaH_2PO_4 and 10 mM D-glucose (pH adjusted to 7.4 by gassing with 95% O_2, 5% CO_2), at 5 ml/min using a peristaltic pump (Watson-Marlow Alitea-AB, Sin-Can, Calgary, Alberta, Canada) and buffer temperature was controlled at 34 °C. Imaging was started within 10 min following activation of the perfusion system.

To image FlicR1, the hippocampal slice was excited with the 100 W mercury arc lamp using a filter cube with 565/30 nm excitation filter, a 620/50 nm emission filter and 585 nm dichroic (Semrock Inc, Rochester, New York, USA). Images were acquired at 100 Hz at 2×2 binning (Figure 2-6B spontaneous activity) and 50 Hz (Figure 2-6E stimulated activity) using a digital sCMOS camera (Hamamatsu Orca-Flash2.8, Hamamatsu Photonics K.K.). For stimulation with theophylline, approximately 30 s after the start of the experiment, the superfusate was changed from control ACSF to ACSF containing 10 mM theophylline (Sigma-Aldrich, directly dissolved in ACSF). Approximately 10 min later, the superfusate was changed back to control ACSF. Four organotypic brain slices transfected with FlicR1 were imaged and showed similar responses. Figure 2-6 shows representative fluorescence traces from neurons in organotypic slices.

Data Analysis. For measurements of speed and sensitivity in HEK cells, fluorescence traces were extracted using the maximum likelihood

pixel weighting algorithm described in (*189*). Briefly, each pixel's fluorescence was correlated with the average whole-field fluorescence. Pixels with stronger correlation to the mean were weighted preferentially in the measurement of fluorescence, emphasizing the pixels containing the most information. The 5% of pixels with the highest correlation to the mean were used for characterization of protein speed and sensitivity. Fluorescent responses to step functions were averaged over 100 trials and fit with a double exponential function to acquire the time constants of FlicR1's fluorescent response. Sensitivities were defined as the maximum percent change in fluorescence over a 150 mV change in voltage.

Photobleaching traces were obtained by subtracting the average fluorescence of a region of user-defined background region from the average fluorescence of the user-defined region of the cell. The resulting traces were then fit to a single exponential with a baseline offset to obtain the photobleaching time constant. FlicR1 showed transient photoactivation in the first 100 seconds, which was ignored for photobleach calculations.

For neuronal measurements, the cell body and dendrites were manually selected and the average intensity of all included pixels was averaged. The background intensity of a user defined background region was subtracted from the raw signal. A photobleaching baseline was constructed from the whole-field intensity by a sliding minimum filter, followed by a sliding mean filter. Each frame of the movie was then corrected by dividing by this baseline. Signal-to-noise ratio was calculated

90

as the maximum fluorescence response to action potential (as identified by the patch-clamp recording) divided by the standard deviation of the baseline fluorescence.

Data was analyzed using custom Matlab codes and Microsoft Excel. A Q-Q plot was used to test the normality of data sets being compared. Both data sets were determined to have equal variance using the F-Test (α = 0.05). Unless noted otherwise, values reported are Mean ± S.E.M. A statistical method was not used to justify sample sizes, but sample sizes are similar to those used by others in the field. Data selection criteria for experiments are stated in the methods section for each experiment, and are similar to those used by others in the field.

Chapter 3 Fluorescent protein-based voltage indicators based on a tandem dimer design

3.1 Introduction

Changes in membrane potential (i.e., voltage) are the fundamental carriers of neural information and, therefore, measurement of these changes is the most direct read out of neural activity. Although voltage is most commonly measured with electrodes, fluorescence-based techniques are being used for an increasingly wide range of applications. A key requirement of fluorescence-based approaches is an exogenous fluorescent indicator molecule that changes its fluorescence intensity in response to a change in membrane voltage. Numerous examples of both synthetic dye-based indicators and genetically encoded FP-based indicators of membrane voltage have been reported (*214–216*). In this chapter we will focus on the design principles of FP-based voltage indicators and report our findings using novel design strategies.

Four fundamental characteristics that are required for an ideal voltage indicator are: rapid kinetics, high voltage sensitivity, bright fluorescence, and proper membrane targeting. Membrane potential changes occur on the order of a few milliseconds. This fact necessitates that an ideal indicator have sufficiently rapid kinetics and high voltage sensitivity in order to report those changes with high fidelity and without loss of

temporal resolution. An ideal voltage indicator must also be sufficiently bright to enable imaging with the very short exposure times (~1 ms) that are required for ~1 kHz image acquisition. Finally, to report membrane potential, an ideal indicator must efficiently target to the plasma membrane. Any indicator protein that is not properly targeted to the plasma membrane will result in non-responsive background fluorescence that reduces the overall fluorescence signal amplitude.

Protein engineers have used several protein design strategies to couple membrane potential changes to fluorescence changes. In one family of genetically encoded voltage indicators, VSDs are fused to one FP, or a FRET pair of FPs (Figure 3-1). Prototypes have been engineered using various VSDs (*215*), however, it has been found that the VSDs from the marine organism *Ciona intestinalis* (CiVSD) (*217*) and from chicken *Gallus gallus* (GgVSD) (*15*) are most efficiently targeted to the membrane of mammalian cells. VSDs are composed of four transmembrane helices, numbered S1 to S4. The fourth helix (S4) contains several positively charged amino acids and consequently moves with changes in membrane potential. In the case of single FP-based indicators, this conformational change is relayed to an FP barrel and causes changes in the chromophore environment that lead to changes in fluorescence intensity (Figure 3-1A, B and C). In FRET-based indicators, the conformational change leads to a change in distance or orientation between the two FPs,

resulting in a change in FRET signal (Figure 3-1D and E). In all of these designs only one VSD is used.
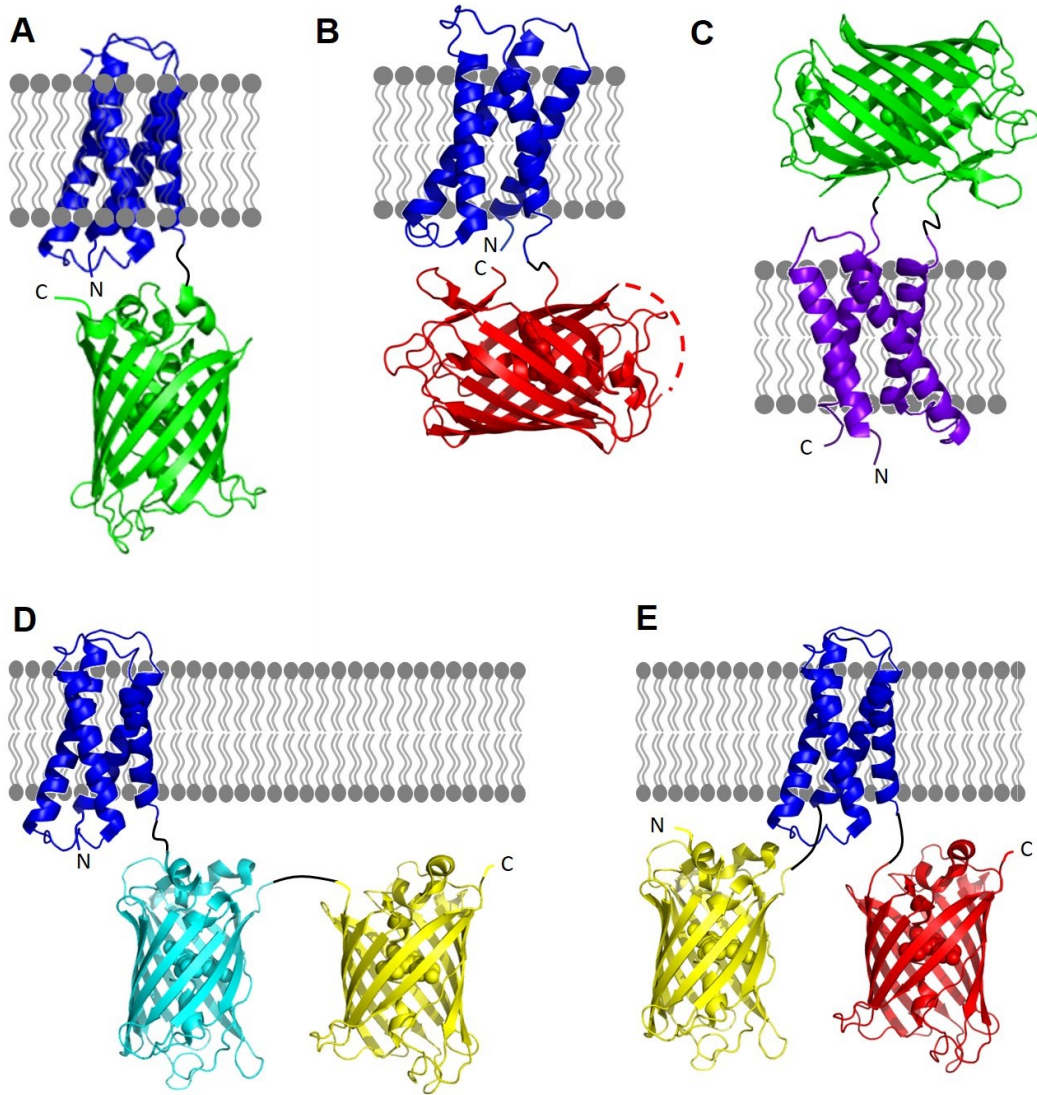
Figure 3-1 Schematic representations of voltage indicator designs based on single VSDs. (A) A single FP is fused to S4 of the CiVSD. (B) A cpFP is fused to S4 of the CiVSD. (C) A cpFP is fused between the S3 and S4 helices of GgVSD. In this design the FP barrel is outside the cell. (D) A FRET pair is fused to S4 of CiVSD. (E) A FRET pair is fused to S1 and S4 and flank the CiVSD. Cartoon representations are prepared using PyMol (32).

Recently, crystal structures of CiVSD have been determined in both the active and resting conformations (*199*). In these crystal structures, it is apparent that CiVSD forms a homodimer at the S1/S4 interface (Figure 3-2). This finding prompted us to design voltage indicators based on a VSD tandem dimer, where a cpFP would link both copies of the VSD. We reasoned that in this design the chromophore of a cpFP would be well positioned to sense S4 helix movement. We tested whether fixing the C-terminus of an indicator with the topology shown in Figure 3-1B to a second VSD domain would lead to improved variants with larger voltage sensitivity. Specifically we tested tandem dimer variants of FlicR and compared them to FlicR1 in terms of voltage sensitivity. We also reasoned that by adding a second VSD we could engineer a two-colour ratiometric voltage indicator by harnessing the movement of both S4 helices to affect the fluorescence of two different colours of FP.

3.2 Results

3.2.1 Development of tandem dimer red voltage indicators

To develop a red fluorescent voltage indicator based on a tandem VSD dimer, we fused a second CiVSD to the C-terminus of FlicR1 (Figure 3-2). Simple fusion led to a construct with dim fluorescence when expressed in *E. coli*. We reasoned that the protein sequence at the fusion site between the C-terminus of the cpRFP (specifically, cpmApple) domain and the second CiVSD would have a strong effect on protein folding and

maturation. Inspection of the X-ray crystal structure shows that CiVSD has 105 flexible residues on its N-terminus. Furthermore, previous studies showed that the first 70 residues on the N-terminus of CiVSD are not necessary for folding or membrane targeting (*186*). In an effort to identify the optimal length and composition of the linker between the cpmApple domain and the second CiVSD, we created a series of linker libraries by systematically truncating the unstructured region to shorten the distance between cpmApple and the second CiVSD (Figure 3-2B). We also randomized two residues at the junction between the two domains.

| Ci-VSD | cpmApple | linker | Ci-VSD |

Δ	Linker sequence												
0	Q K K T M G W E A T R X X G^3	F	D	G	S	D	F	S	P	P	A		
40	Q K K T M G W E A T R X X P^{43}	R	K	S	E	S	V	K	K	V	H		
50	Q K K T M G W E A T R X X H^{53}	W	N	D	V	D	Q	G	P	S			
60	Q K K T M G W E A T R X X E^{63}	K	P	E	T	R	Q	E	E	R			
70	Q K K T M G W E A T R X X I^{73}	D	I	P	E	I	S	G	L	W	W		
80	Q K K T M G W E A T R X X W^{83}	G	E	N	E	H	G	V	G				
90	Q K K T M G W E A T R X X G^{93}	R	M	E	I	P	T	T	G	V			
100	Q K K T M G W E A T R X X G^{103}	R	V	Q	F	R	V	R	A	V			
110	Q K K T M G W E A T R X X I^{113}	D	H	L	G	M	R	A	F	G			

Gene library → Brightness screen → Voltage sensitivity screen

Figure 3-2 Schematic representation of tdFlicR design and linker libraries and directed evolution process. (A) Schematic representation of the tdFlicR design where cpmApple is inserted between two CiVSDs. (B) Linker libraries constructed by varying the linker length between cpmApple and the second VSD domain. Red residues are the C-terminal end of cpmApple, X denotes a randomized residue and blue residues are the

start of the second CiVSD. Superscript numbers denote the original CiVSD residue number. (C) Schematic of screening method used to select tdFlicR variants. A gene library was created using overlap PCR, followed by a brightness screen in *E. coli* followed by a test for voltage sensitivity in HeLa cells. Cartoon representation in (A) is prepared using PyMol (32).

We screened the linker library variants for brightness, membrane trafficking, and voltage sensitivity, as schematically represented in Figure 3-2C. Colonies of *E. coli* transformed with linker libraries exhibited a range of red fluorescence intensities. The colonies with brightest fluorescence were picked for secondary screening in mammalian cells (HeLa cells). Mammalian cells were subjected to 10 ms electrical field pulses using a custom-built field stimulation system and fluorescence response to stimulation was recorded (Figure 3-2C). Arclight Q239 (a green voltage indicator) was used as an internal reference for membrane trafficking and voltage sensitivity (Figure 3-2C).

Truncation of 0, 40 or 50 residues of CiVSD did not result in variants that were bright enough to report ITV in HeLa cells. We found that truncating more than 60 residues of the second CiVSD resulted in constructs with sufficient fluorescence to enable high-speed imaging and report ITV in our HeLa cell screen. In libraries with 60, 70, 80, 90, 100 or 110 residues truncated, Ala, Arg, Gly, Lys and His were selected for at the two randomized positions at the fusion site between cpmApple and the second CiVSD. For these libraries (i.e., 60, 70, 80, 90, 100 or 110 residues truncated), we found that that all variants exhibited similar

brightness and voltage sensitivity. Linker libraries in which more than 110 residues were truncated exhibited an almost complete loss of fluorescence likely due to poor folding efficiency of the second CiVSD domain. We picked a variant from the Δ110 library with Ala and Arg at the fusion site (designated tdFlicR Δ110AR) for further characterization in HeLa cells and cultured neurons.

3.2.2 Imaging tdFlicR in HeLa cells and cultured neurons

When expressed in HeLa cells, tdFlicR Δ110AR localized to the plasma membrane (Figure 3-3A) and gave robust fluorescence changes in response to induced transmembrane voltage (ITV) (Figure 3-3A-D). Relative to ArcLight Q239, tdFlicR Δ110AR has a 2.9 ± 0.5-fold (n = 9 HeLa cells) greater fluorescence response to a 10 ms electrical pulse, which is comparable to FlicR1's voltage sensitivity (Figure 3-3E). Although we applied our screening strategy to additional truncation libraries (truncations in two residue increments from Δ100 to Δ116 while randomizing the two residues at the junction), we were unable to identify variants that surpassed FlicR1's performance.
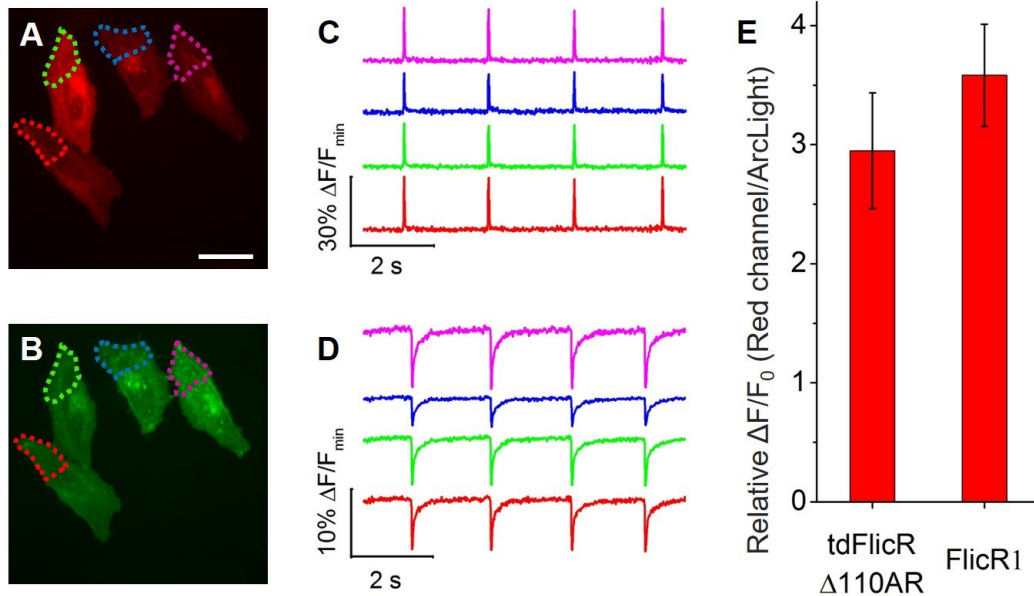
Figure 3-3 tdFlicR Δ110AR imaging in HeLa cells. (A-B) Image of HeLa cells co-expressing tdFlicR Δ110AR (A) and ArcLight Q239 (B), scale bar 10 μm. (C) tdFlicR Δ110AR fluorescence response of four regions shown in (A) to electrical field stimulation pulses (10 ms, 25 V). (D) ArcLight Q239 fluorescence response of the same four regions shown in (C) to electrical field stimulation pulses (10 ms, 25 V). (E) Comparison of voltage sensitivity between tdFlicR Δ110AR (n = 10 cells) and FlicR1 (n = 12 cells) represented as a ratio of response amplitude in HeLa cells compared to ArcLight Q239. Error bars are standard deviation.

Next, we expressed tdFlicR Δ110AR in dissociated rat hippocampal neurons to test its response to spontaneous action potentials during single-trial recordings. tdFlicR Δ110AR labelled the plasma membrane both at the cell body and in individual dendrites (Figure 3-4A). It also showed intracellular puncta in the cell bodies similar to FlicR1 and other cpmApple-derived indicators (Figure 3-4A). When imaged at 100 Hz using a widefield fluorescence microscope, tdFlicR Δ110AR responded to

spontaneous activity of the transfected neurons with ~2% $\Delta F/F_0$ (Figure 3-4B).
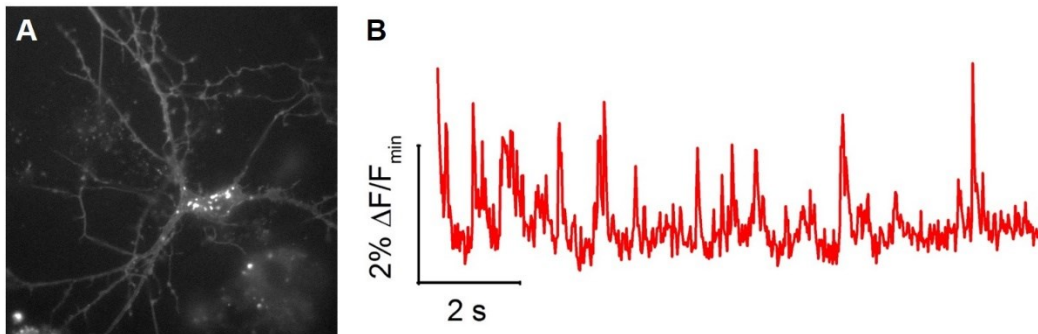
Figure 3-4 tdFlicR Δ110AR imaging in neurons. (A) Image of cultured hippocampal neuron expressing tdFlicR Δ110AR. (B) Detection of spontaneous activity in rat hippocampal neuron culture transfected with tdFlicR Δ110AR. Single-trial recordings of spontaneous action potential bursts imaged at 100 Hz using widefield fluorescence imaging.

3.2.3 Development of a tandem dimer ratiometric green/red voltage indicator

Although we were unable to identify tdFlicR variants that had clear advantages compared to FlicR1, we recognized that the tdFlicR topology included a second VSD that could potentially be used to modulate the fluorescence of a second different colour of FP. We hypothesized that this could enable us to construct a two-colour ratiometric voltage indicator if the second FP: 1) can be spectrally separated from mApple; and 2) exhibits a decrease in fluorescence upon membrane depolarization in contrast to the increase in fluorescence exhibited by tdFlicR.

Arguably the most robust of the currently available green FP-based voltage indicator is ASAP1 (*15*). ASAP1 was constructed by fusing a circularly permutated GFP between the S3 and S4 helices of GgVSD, as schematically represented in Figure 3-1C. Notably, ASAP1 exhibits a decrease in green fluorescence in response to membrane depolarization. This makes ASAP1 a suitable scaffold for use in a two-colour ratiometric voltage indicator using the tdFlicR design. Because ASAP1 uses GgVSD, we began by comparing the amino acid sequence of GgVSD and CiVSD to analyze the S1/S4 interface and rationalize if they would form a heterodimer. Alignment of the two VSD sequences showed high similarity in sequence for the S1 and S4 helices (Figure 3-5). In addition, the residues that were not identical had similar chemical properties (Figure 3-5). Inspection of the CiVSD homodimer S1/S4 interface (PDB ID: 4G80) revealed 14 residues from the S1 and S4 α-helices pointing towards the dimer interface. Nine residues are identical between CiVSD and GgVSD and five residues were conservative substitutions, namely Leu127Ile, Val220Thr, Leu224Val, Val227Ile, and Ala231Ile relative to the CiVSD sequence. We reasoned that fusing GgVSD as part of our tandem dimer construct will very likely result in formation of an intramolecular heterodimer between CiVSD and GgVSD.

```
residue #   1  2  3  4  5  6  7  8  9 10 11 12 13 14 15 16 17 18 19 20 21 22 23 24 25 26 27 28 29 30 31 32 33 34 35 36 37 38 39 40
GgVSD       -  -  -  -  -  -  -  -  -  -  -  -  -  -  -  -  -  -  -  -  -  -  M  E  T  T  -  -  -  -  -  -  -  -  -  -  -  -  -  -
CiVSD       M  E  G  F  D  G  S  D  F  S  P  P  A  D  L  V  G  V  G  G  A  V  M  R  N  V  V  D  V  T  I  N  G  D  V  T  A  P  P  K
                                                                          *        .  .     .

residue #  41 42 43 44 45 46 47 48 49 50 51 52 53 54 55 56 57 58 59 60 61 62 63 64 65 66 67 68 69 70 71 72 73 74 75 76 77 78 79 80
GgVSD       -  -  -  -  -  -  -  -  -  -  -  V  R  Y  -  -  -  E  Q  G  S  -  E  L  T  K  T  S  S  S  P  T  A  D  E  P  T  I  K  -
CiVSD       A  A  P  R  K  S  E  S  V  K  K  V  H  W  N  D  V  D  Q  G  P  S  E  K  P  E  T  R  Q  E  E  R  I  D  I  P  E  I  S  G
                                              *     :        :  *  *     *        *                 .  .        *     *     *

residue #  81 82 83 84 85 86 87 88 89 90 91 92 93 94 95 96 97 98 99 100 101 102 103 104 105 106 107 108 109 110 111 112 113 114 115 116 117 118 119 120
GgVSD       -  -  -  -  -  I  D  D  G  R  D  E  G  N  -  -  E  Q  D  S  C  S  N  T  I  R  R  K  I  S  P  F  V  M  S  F  G  F  R  V
CiVSD       L  W  W  G  E  N  E  H  G  V  G  G  G  R  M  E  I  P  T  T  G  V  G  R  V  Q  F  R  V  R  A  V  I  D  H  L  G  M  R  A
                            :     .  *                 .  .        :  :        :  .     .              :  *  :     *     .

residue # 121 122 123 124 125 126 127 128 129 130 131 132 133 134 135 136 137 138 139 140 141 142 143 144 145 146 147 148 149 150 151 152 153 154 155 156 157 158 159 160
GgVSD       F  G  V  V  L  I  I  V  D  I  I  V  V  I  V  D  L  A  I  S  E  K  K  R  G  I  R  E  I  L  E  G  V  S  L  A  I  A  L  F
CiVSD       F  G  V  F  L  I  L  L  D  I  I  L  M  I  I  D  L  S  L  P  G  K  S  E  S  S  Q  S  F  Y  D  G  L  A  L  A  L  S  C  Y
            *  *  *     *  *  :  :  *  *  *  :     *  :  *  *  :        .        *  .     .     :     :     .  *     *  *  :     .

residue # 161 162 163 164 165 166 167 168 169 170 171 172 173 174 175 176 177 178 179 180 181 182 183 184 185 186 187 188 189 190 191 192 193 194 195 196 197 198 199 200
GgVSD       F  L  V  D  V  L  M  R  V  F  V  E  G  F  K  N  Y  F  R  S  K  L  N  T  L  D  A  V  I  V  V  G  T  L  L  I  N  M  T  Y
CiVSD       F  M  L  D  L  G  L  R  I  F  A  Y  G  P  K  N  F  F  T  N  P  W  E  V  A  D  G  L  I  I  V  V  T  F  V  V  T  I  F  Y
            *  :     *  :     *  *  :  *        .  :     *  *  :  *     .     .        .  :        *        *  :     *     :  :     *

residue # 201 202 203 204 205 206 207 208 209 210 211 212 213 214 215 216 217 218 219 220 221 222 223 224 225 226 227 228 229 230 231 232 233 234 235 236 237 238 239 240
GgVSD       S  F  S  D  -  -  -  -  L  A  A  T  D  Q  M  P  Q  M  V  T  L  L  R  V  L  R  I  V  I  L  I  R  I  F  R  L  A  S  Q  K
CiVSD       T  V  L  D  E  Y  F  Q  E  T  G  A  D  G  L  G  Q  L  V  V  L  A  R  L  L  R  V  V  R  L  A  R  I  F  Y  S  H  Q  Q  -
            :  :        *                    .     .     :        *     :     *  :  *     *  :     *     *  :     *  .     *  *  :        *
```

Figure 3-5 Sequence alignment of CiVSD and GgVSD. S1-S4 are highlighted in red and boxed. A (*) indicates positions which have identical residues. A (:) indicates residues with very similar chemical properties. A (.) indicates residues with similar chemical properties. Amino acid sequences aligned using Clustal Omega (*26*, *27*).

To develop a two-colour ratiometric voltage indicator, we substituted the second CiVSD in tdFlicR variants with ASAP1 (Figure 3-6). Inspection of the GgVSD amino acid sequence shows that its flexible N-terminus is 59 residues shorter than CiVSD (Figure 3-5). We therefore constructed a library of 400 protein variants by varying two amino acids at the junction between cpmApple and the full length of GgVSD without any truncations.

A

| Ci-VSD | cpmApple | linker | Gg-VSD | cpsfGFP | Gg-VSD |

B

Figure 3-6 Schematic representation of tdFlicR-ASAP variants. (A) Representation of tdFlicR-ASAP indicator composed of CiVSD linked to cpmApple linked to GgVSD which has a circularly permutated superfolder GFP (*218*) inserted between S3 and S4 helices. (B) A model of tdFlicR-ASAP is represented by the crystal structures of CiVSD (PDB ID 4G80), cpmApple (PDB ID 4I2Y) and cpGFP (PDB ID 3EVR). Cartoon representation in lower panel is prepared using PyMol (32).

Expression of the library of tdFlicR-ASAP variants in *E. coli* colonies revealed that there were a number of variants with bright fluorescence in both the green and red channels. Green fluorescence was similar in all *E. coli* colonies however red fluorescence varied. We selected colonies that exhibited bright red (and green) fluorescence and isolated their DNA. Next we transfected mammalian cells to check for proper membrane trafficking and test for sensitivity to membrane potential changes. Mammalian cells transfected with tdFlicR-ASAP variants were subjected to 10 ms electrical field pulses to induce a transmembrane voltage. Fluorescence responses to stimulation were recorded in both the green and red channels (Figure 3-7A-D). All variants tested showed an increase in red fluorescence (Figure 3-7C) and a decrease in green fluorescence (Figure 3-7D) in response to ITV. The variant with brightest red and green fluorescence (later found to have Val and Lys at the fusion site) was picked for further characterization in HEK cells and cultured neurons. We designated this variant as tdFlicR-VK-ASAP.
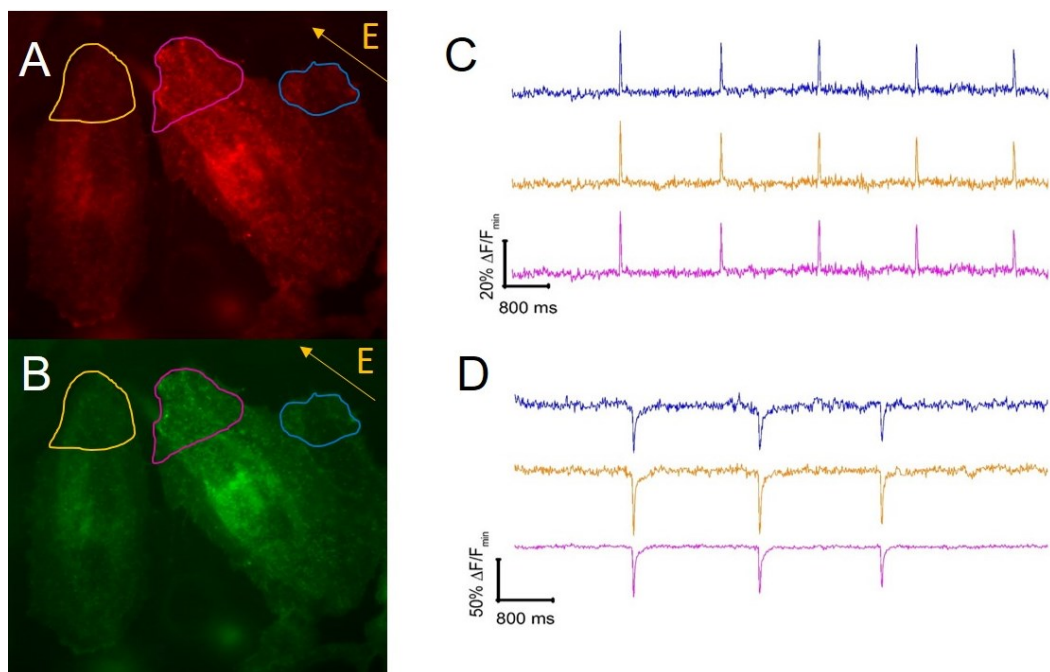
Figure 3-7 Imaging ITV with tdFlicR-VK-ASAP (A-B) Image of HeLa cells expressing tdFlicR-VK-ASAP1 in the red channel (A) and green channel (B). (C) tdFlicR-VK-ASAP red fluorescence response of three regions shown in (A) to electrical field stimulation pulses (10 ms, 25 V). (D) tdFlicR-VK-ASAP green fluorescence response of the same three regions shown in (B) to electrical field stimulation pulses (10 ms, 25 V).

3.2.4 Imaging tdFlicR-ASAP in HEK cells and cultured neurons

We next expressed tdFlicR-VK-ASAP under a CMV promoter in HEK cells and used whole cell voltage clamp to modulate membrane potential while recording the fluorescence response. To realize the full potential of the green/red ratiometric fluorescence response to voltage, we sought to record both the green and red fluorescence channels simultaneously. For this we used a dual band excitation and emission filter along with a beam splitter to spectrally separate both the green and red channels and image

105

them simultaneously (Materials and methods section). We illuminated the cells using a 200 W xenon arc lamp and collected fluorescence images at 100 Hz using a fast CMOS camera. We varied the membrane potential from -70 mV to +30 mV (50 ms spikes at 10 Hz) (Figure 3-8). In voltage clamped HEK cells, tdFlicR-VK-ASAP was able to track 10 Hz voltage spikes in both the green and red channels simultaneously. Green fluorescence decreased by ~10% $\Delta F/F_0$ and red fluorescence increased by ~5% $\Delta F/F_0$ with a ratio change of ~25% $\Delta R/R_0$ (Figure 3-8).
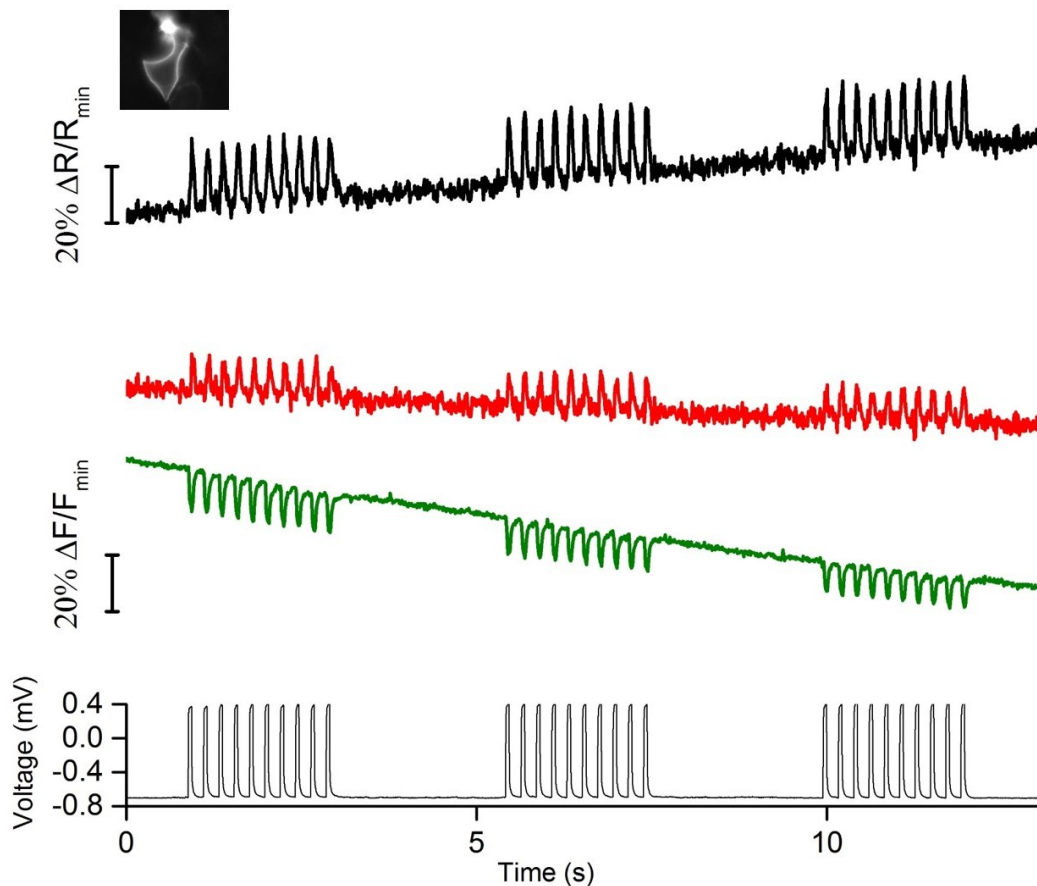
Figure 3-8 Imaging membrane voltage fluctuations with tdFlicR-VK-ASAP. Gray trace: Patch clamp recording. Green trace: Raw tdFlicR-VK-ASAP green fluorescence readout from single-trial optical recording of

membrane fluctuations without correction for photobleaching. Red trace: Raw tdFlicR-VK-ASAP red fluorescence readout from single-trial optical recording of membrane fluctuations without correction for photobleaching. Black trace: Ratiometric fluorescence change (red/green) of single-trial optical recording of membrane fluctuations. Inset: Image of patched HEK cell expressing tdFlicR-VK-ASAP1.

Next we expressed tdFlicR-VK-ASAP in dissociated rat hippocampal neurons to test its membrane trafficking in neurons and its ability to respond to spontaneous action potentials. Although tdFlicR-VK-ASAP trafficked to the membrane of neurons, the red channel revealed puncta in the cell body (Figure 3-9A and B), that is characteristic of mApple-based indicators as discussed previously. The green channel showed membrane targeted green fluorescence with no puncta. Unfortunately, we were unable to detect spontaneous activity in neurons expressing tdFlicR-VK-ASAP when using a widefield fluorescence imaging setup. Compared to the 50 ms artificial spikes we induced in HEK cells (Figure 3-8), true action potentials are ~50 times shorter in duration (1-2 ms). Imaging at 100 Hz using widefield microscopy and 200 W lamp as a light source and a beam splitter to separate the two fluorescence channels probably resulted in very low fluorescence intensities. We suspect that fluorescence responses to voltage were not detected due to an insufficient signal-to-noise ratio.
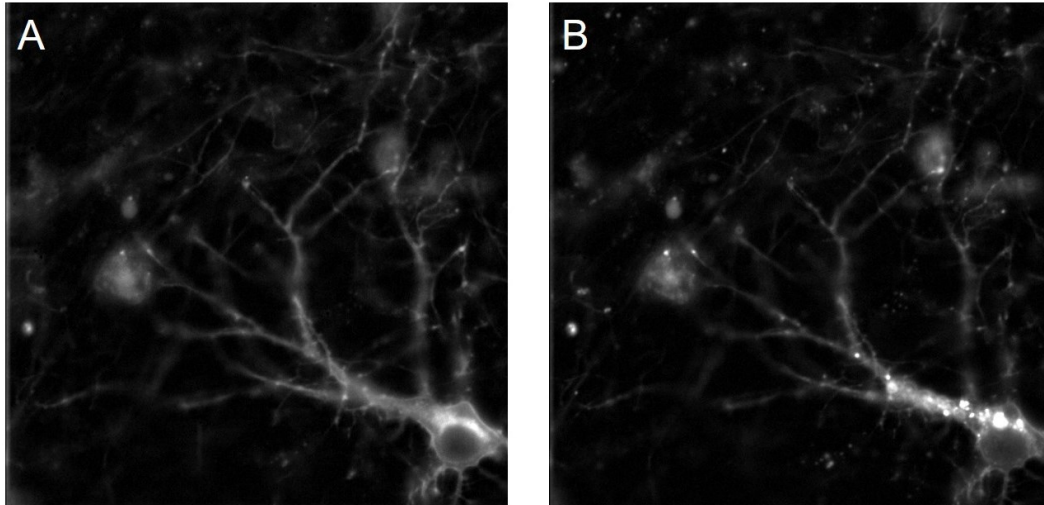
Figure 3-9 tdFlicR-VK-ASAP imaging in neurons. (A-B) Image of cultured hippocampal neuron expressing tdFlicR-VK-ASAP in the green channel (A) and red channel (B). Note that the fluorescence puncta are only present in the red channel (B).

3.3 Conclusion

In this chapter we reported our efforts to explore two novel designs for engineering FP-based voltage indicators. Inspired by the X-ray crystal structure of CiVSD (*199*), we engineered prototypes of a red voltage indicator (tdFlicR1Δ110AR) and a ratiometric green/red voltage indicator (tdFlicR-VK-ASAP) based on a tandem VSD dimer topology. By combining rational design and directed evolution, we selected for variants that had sufficient brightness, response speed, response amplitude, and membrane localization, to report membrane potential fluctuations in mammalian cells.

Using widefield fluorescence imaging, tdFlicR Δ110AR was able to report spontaneous activity in dissociated neuron cultures. tdFlicR-VK-

ASAP was able to report induced changes in membrane potential in HEK cells; however, it was unable to report spontaneous activity in neuron cultures. This negative result may be the result of insufficient illumination intensity used in our widefield imaging setup. Nevertheless, it is prudent to note that increasing illumination intensity would result in photoactivation of mApple (as discussed in Chapter 2), which would likely complicate imaging of tdFlicR-VK-ASAP. To engineer more robust ratiometric green/red indicators, other red FPs could be explored as alternatives for circularly permutated mApple.

3.4 Materials and methods

Molecular biology to construct tandem dimer voltage indicators. Polymerase chain reaction (PCR) amplification was used to construct the DNA linker libraries for tdFlicR variants. Synthetic oligonucleotides (Integrated DNA Technologies) were used as primers for amplification and Pfu polymerase (Thermo Fisher Scientific) was used to maintain high fidelity DNA replication. In the case of tdFlicR variants, overlap PCR was used to link CiVSD to the 3' end of FlicR1. In the case of tdFlicR-ASAP variants, overlap PCR was used to link ASAP1 (Addgene: 52519) to the 3' end of FlicR1. Two codons at the junction were encoded as NNK to fully randomize those positions in all linker libraries. Restriction endonucleases (Thermo Fisher Scientific) were used to digest PCR products and expression vectors. Agarose gel electrophoresis was used to purify DNA products from PCR and restriction digestion reactions. The DNA was

extracted from the gels using the GeneJET gel extraction kit (Thermo Fisher Scientific). Ligations were performed using T4 DNA ligase (Thermo Fisher Scientific).

Plasmids for *E. coli* and mammalian cell expression. We used pcDuEx0.5 (described previously in Chapter 2) as the vector for expression of the constructs in *E. coli*, HeLa cells and HEK cells. The gene was inserted between *BamHI* and *XbaI* restriction sites. For expression of variants in neurons, genes were cloned from plasmid pcDuEx0.5 into the *BamHI* and *HindIII* sites of pAAV2 vector (Addgene: 61249). Expression was controlled using human synapsin I promoter to preferentially express in neurons. A 3' Woodchuck Hepatitis Virus Posttranscriptional Regulatory Element (WPRE) sequence was used to enhance expression.

Screening libraries in *E. coli*. Gene libraries were used to transform electro-competent *E. coli* strain DH10B (Invitrogen) by electroporation (10 kV/cm, ~ 5ms pulse) (MicroPulser™ Electroporator, BIO-RAD). *E. coli* cells were then plated and cultured at 37 °C on LB agar plates supplemented with ampicillin (400 µg/ml) to obtain 500-1000 colonies per plate. Colonies were then imaged using a custom imaging setup described previously (*200*). In the case with tdFlicR variants, plate images were acquired using a 560/40 nm excitation filter and 630/60 nm emission filter to screen for brightness in the red channel. In the case with green/red ratiometric voltage indicator constructs, images were acquired in the green

(470/40 nm excitation filter and 525/50 nm emission filter) and red (560/40 nm excitation filter and 630/60 nm emission filter) channels. For each linker library, ~5,000 colonies (10 plates) were screened. Colonies with the top 0.01% fluorescence brightness were manually picked and cultured in 4 ml LB media supplemented with ampicillin (100 µg/ml). Plasmids were then extracted using GeneJET plasmid miniprep kit (Thermo Fisher Scientific).

Cell culture. HeLa cells (ATCC, CCL-2) or HEK293A cells (CRL-11268, ATCC) were cultured in Dulbecco's modified Eagle's medium (DMEM) (supplemented with 10% fetal bovine serum (FBS) (Sigma), 2 mM GlutaMax (Invitrogen), penicillin-G potassium salt (50 units/ml), and streptomycin sulfate (50 µg/ml)) and incubated for 48 h at 37 °C, 5% CO_2. Cells were split and cultured on collagen-coated 35 mm glass bottom dishes (Matsunami) to ~50% confluency. Transfection was performed by incubating HeLa cells or HEK cells with a mixture of 1 µg of plasmid DNA and 2 µL of Turbofect (Thermo Fisher Scientific) for 2 hours following the manufacturer's instructions. Imaging was performed 24-48 hours after transfection.

Induced transmembrane voltage (ITV) screening. Linker library variants were co-expressed in HeLa cells together with the inward rectifier potassium channel, Kir2.1 (Addgene: 32641). In the case of red tdFlicR variants, ArcLight Q239 (Addgene: 36856) was used as an internal reference. Expression of Kir2.1 in HeLa cells helped maintain the resting

111

potential around -60 mV, which is appropriate for screening neuronal voltage indicators. A uniform electric field of ~50 V/cm was applied across the cell culture to create an ITV. A pulse generator (PG 58A, Gould Advance Ltd.) was used to apply a 10 ms square-wave pulse at ~0.5 Hz. An amplifier (6824A 40V/25A HP/Agilent) was used to obtain a pulse amplitude of 25 V. Two parallel platinum electrodes (0.5 cm apart) were used to deliver the pulses to the cell culture. Fluorescence was imaged (in both the green and red channels) at a frame rate of 100 Hz for 10 seconds during multiple electric field pulses.

Imaging ITV in HeLa cells. Imaging was carried out in HEPES (25 mM) buffered Hanks' Balanced Salt Solution (HBSS). An inverted fluorescence microscope (Eclipse Ti-E, Nikon) equipped with a 200 W metal halide lamp (PRIOR Lumen) and a 60× oil objective was used to image HeLa cells. Images were acquired at 100 Hz with 4×4 binning using a 16-bit QuantEM 512SC electron-multiplying CCD camera (Photometrics). A FITC/Cy2 filter set (470/40 nm (excitation), 525/50 nm (emission), and a 495LP dichroic mirror (set number 49002, Chroma)) was used to image ArcLight Q239. The same filter set was used to image the green channel of tdFlicR-ASAP variants. A TRITC/Cy3 filter set (545/30 nm (excitation), 620/60 nm (emission), and a 570LP dichroic mirror (set number 49005, Chroma)) was used to image the red channel of tdFlicR and tdFlicR-ASAP variants. The NIS Elements Advanced Research software (Nikon) was used to control the microscope and camera. The raw

fluorescence traces of both the red and green channels were extracted from identical regions of interest in cells and exported into a customized Microsoft Excel spreadsheet. Background subtraction, photobleaching corrections, and calculations of average $\Delta F/F_{min}$, were performed in Excel (Microsoft). In the case of tdFlicR variants, the average $\Delta F/F_{min}$ of tdFlicR signals were compared to those of ArcLight signals from the same cells, and the ratio of $\Delta F/F_{min}$ of FlicR over ArcLight was reported. The best variant in terms of maximum mean ratio in each library was identified and the isolated plasmid DNA was submitted for DNA sequencing.

Fluorescence imaging and electrophysiology of HEK cells. All imaging and electrophysiology measurements were performed in Tyrode buffer (125 mM NaCl, 2.5 mM KCl, 3 mM $CaCl_2$, 1 mM $MgCl_2$, 15 mM HEPES, 30 mM glucose, pH 7.3). Filamented glass micropipettes (WPI) were pulled to a tip resistance of 4–8 MΩ, and filled with internal solution containing 125 mM potassium gluconate, 8 mM NaCl, 0.6 mM $MgCl_2$, 0.1 mM $CaCl_2$, 1 mM EGTA, 10 mM HEPES, 4 mM Mg-ATP, 0.4 mM Na-GTP (pH 7.3), adjusted to 295 mOsm with sucrose. Whole-cell voltage recordings were amplified (×10 k) and bandpass filtered (0.3–1 kHz) (A-M systems, 1700, Carlsborg, WA, USA). Signals were then integrated (time constant 15 ms) and digitally sampled at 1 kHz (Powerlab/8SP, ADInstruments, Colorado Springs, CO, USA), and stored on a computer using LabChart7 software (ADInstruments).

Widefield imaging was performed on an upright FV1000 confocal microscope (OlympusCanada, Markham, ON, Canada) equipped with software (FluoView1000, Olympus Canada), a 20× XLUMPlanF1 water immersion objective (numerical aperture (NA) = 1.00), and connected to a 200 W xenon arc lamp (Lambda XL, Sutter Instruments). Images were acquired at 100 Hz with 2×2 binning using a using a CMOS digital camera (Hamamatsu Orca-Flash2.8; Hamamatsu Photonics). A dual band excitation and barrier filter sets (475/10 nm (excitation), 570/10 nm (excitation), 530/30 nm (emission) and 625/50 nm (emission)) and a polychromatic mirror having two bandpass transmission regions (510-555 nm and 585-65 nm bandpass) along with a beam splitter was used to image tdFlicR-VK-ASAP simultaneously in both the green and red channels.

Culturing dissociated rat hippocampal neurons. Dissociated E18 Sprague Dawley hippocampal cells in Hibernate® EB Complete Media were purchased from BrainBits LLC. The cells were grown on 35 mm glass bottom dish (In Vitro Scientific) coated with poly-D-lysine (EMD Millipore, A-003-E) containing 2 ml of NbActiv4 (BrainBits LLC) supplemented with 2% FBS, penicillin-G potassium salt (25 units/ml), and streptomycin sulfate (25 μg/ml). Half of the culture media was replaced every 3 days. Neuronal cells were transfected on day 8 using Lipofectamine 2000 (Life Technologies) following the manufacturer instructions. Briefly, 1-2 μg of plasmid DNA and 4 μL of Lipofectamine

2000 (Life Technologies) were added to 100 µl of NbActive4 medium to make the transfection medium. This medium was then incubated at room temperature for 10-15 minutes. Half of the culture medium (1 ml) from each neuron dish was taken out and combined together with an equal volume of fresh NbActiv4 medium (supplemented with 2% FBS, penicillin-G potassium salt (25 units/ml), and streptomycin sulfate (25 µg/ml)) to make a 1:1 mixture and incubated at 37 °C and 5% CO_2. 1 ml of fresh conditioned (at 37 °C and 5% CO_2) NbActiv4 medium was then added to each neuron dish. The transfection medium was then added and the neuron dishes were incubated for 2-3 hours at 37 °C in a CO_2 incubator. The media was then replaced using the conditioned 1:1 medium prepared previously. The cells were incubated for 48-72 hours at 37 °C in a CO_2 incubator before imaging.

Imaging primary neuron cultures. Imaging was carried out in HEPES (25 mM) buffered HBSS. Widefield imaging was performed on an inverted Nikon Eclipse Ti-E microscope equipped with a 200 W metal halide lamp (PRIOR Lumen), 60× oil objectives (NA = 1.4, Nikon), and a 16-bit QuantEM 512SC electron-multiplying CCD camera (Photometrics). A TRITC/Cy3 filter set (545/30 nm (excitation), 620/60 nm (emission), and a 570LP dichroic mirror, set number 49005, Chroma) was used to image tdFlicR variants. A dual band excitation and barrier filter sets (475/10 nm (excitation), 570/10 nm (excitation), 530/30 nm (emission) and 625/50 nm (emission)) and a polychromatic mirror having two bandpass transmission

regions (510-555 nm and 585-65 nm bandpass) along with a beam splitter was used to image tdFlicR-VK-ASAP simultaneously in both the green and red channels. For time-lapse imaging, neurons were imaged at 100 Hz imaging frequency with 4×4 binning.

Chapter 4 Engineering a photoconvertible voltage indicator for live cell imaging

4.1 Introduction

At its most fundamental level, brain function emerges from the complex circuitry of neurons receiving synaptic inputs and firing action potentials. Accordingly, fluorescent voltage indicators are of particular utility for probing fundamental questions in neuroscience that relate to the activity of populations of neurons. The current toolbox of FP-based voltage indicators provides a variety of choices with respect to indicator fluorescence colour (green (*14*, *15*), red (*219*), and far-red (*190*)) and kinetics (ranging from ~ 100 ms response time (*14*) to <1 ms (*190*)). However, the transient nature of single action potentials (and voltage indicator fluorescent responses) requires continuous rapid imaging of current voltage indicators with sophisticated cameras and equipment. These imaging techniques have limited fields of view and spatial resolution is sacrificed to varying degrees depending on the size of brain region imaged.

A molecular probe that integrates membrane potential changes over a defined period of time would enable monitoring of whole brain electrical activity without the limitations imposed by rapid imaging requirements. Whereas current FP-based voltage indicators report changes in voltage by

rapidly modulating the chromophore environment of an FP, we hypothesized that fusing a VSD with a photoconvertible FP would enable control of the extent of irreversible photoconversion in a manner that is proportional to the activity of a particular neuron. This protein would photoconvert only when both the membrane is depolarized and the cell is being illuminated with the photoconversion light. In this way, we could achieve irreversible labeling of active neurons during a time window that is controlled with the illumination light. This concept has been successfully used to engineer an integrator for Ca^{2+} ion concentration (CaMPARI) as a proxy for neuronal activity (*220*).

In addition to a voltage integrator, another closely related construct that would be useful for the neuroscience community is a photoconvertible voltage indicator. Although a plethora of voltage indicators currently exist, none have yet emerged that enable selective spectral isolation of specific cells for repetitive imaging over long periods of time. If photoconvertible FPs were to be successfully engineered to sense real-time voltage changes, neuroscientists would be able to specifically "highlight" a single neuron within a tissue such that its voltage could be imaged in a distinct spectral channel separate from other cells. In addition, irreversible spectral highlighting of a cell would enable continuous monitoring of its activity in subsequent experiments within the protein turnover timeframe.

In this chapter we report the development of a photoconvertible voltage indicator and our attempts to engineer a voltage integrator. Using

CiVSD and cpmMaple we successfully engineered a prototype green to red photoconvertible voltage indicator designated as FlicGR0.7 (Fluorescent indicator for voltage imaging – green to red). We used directed protein evolution to screen libraries of thousands of variants to identify clones with sufficient brightness and response amplitude that would report membrane potential changes in mammalian cells. Unfortunately, we were ultimately not successful at generating a voltage integrator that changed its photoconversion rate in an activity dependent manner.

4.2 Results

4.2.1 Development of a photoconvertible voltage indicator

To engineer a photoconvertible voltage indicator, we used protein engineering to combine the properties of a genetically-encoded voltage indicator with that of a photoconvertible FP. We constructed a chimera from the genes for CiVSD (as the voltage sensitive domain) and mMaple FP or mEos2 FP (as the photoconvertible FP). Our choice of the FP to test was a result of work by our lab on photoconvertible Ca^{2+} indicators (*221*) and another lab on a Ca^{2+} integrator (*220*). In our lab, several photoconvertible FPs have been previously tested as templates to engineer photoconvertible Ca^{2+} indicators (*221*). These can be classified into three groups: 1) GFP that increases green fluorescence when illuminated with ~400 nm light (*99*); 2) pamCherry that increases red

119

fluorescence with ~400 nm light illumination (*222*); and 3) Kaede-type FPs that convert from green fluorescence to red fluorescence with ~400 nm light illumination (*51*). Whereas efforts to engineer Ca^{2+} indicators based on photoactivatable GFP and pamCherry were not successful (*221*), using circularly permutated variants of Kaede-type FPs was fruitful resulting in green to red photoconvertible Ca^{2+} indicators (GR-GECOs with mMaple FP barrel) (*221*) and a Ca^{2+} integrator (CaMPARI with mEos2 FP barrel) (*220*).

First, we constructed a chimera from the genes for the voltage sensitive domain CiVSD and the photoconvertible FP mMaple. We chose to use a circularly permutated version of the photoconvertible FP to increase the chance of coupling voltage-induced conformational changes to a change in the FP chromophore environment. This design was expected to maximize the likelihood of translating the movement of the S4 helix in the VSD to the chromophore of the photoconvertible FP. The cpmMaple barrel was cloned from GR-GECO1.1 which was previously reported to be sensitive to conformational changes relayed through a Ca^{2+} binding domain (*221*).

To screen for photoconvertible variants, we used a screening strategy that was similar to the one used to evolve voltage indicators described in previous chapters. Briefly, the screen was divided in two steps. The first step was an *E. coli* bacterial colony screen for brightness and photoconversion efficiency. The second step was a mammalian cell

imaging screen for fluorescent responses to ITV. Briefly, libraries of genes

encoding potential photoconvertible variants were inserted in a dual

bacterial and mammalian expression vector and used to transform *E. coli*.

After overnight growth on agar plates, the green fluorescence of the

colonies was imaged. A photoconversion chamber was then used to

illuminate the bacterial colonies with violet light. An image of the colony

red fluorescence was then taken to assess the photoconversion efficiency

on a colony-by-colony basis (Figure 4-1).
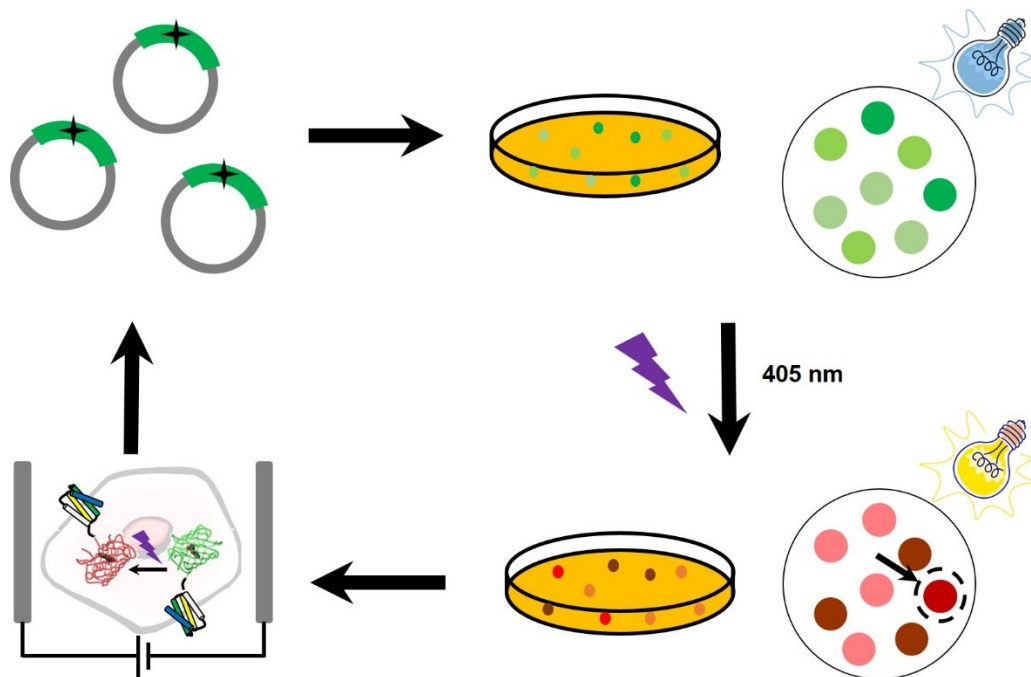
Figure 4-1 Schematic of screening strategy used to engineer FlicGR. First, libraries of DNA encoding indicator genes were used to transform *E. coli* and cultured on agar plates. Second, *E. coli* colonies expressing FlicGR were illuminated with blue light and green fluorescence was imaged. Subsequently, *E. coli* colonies were subjected to 405 nm light for photoconversion. The same colonies were then illuminated with yellow light and red fluorescence was imaged. Colonies with efficient

photoconversion and/or bright red fluorescence were picked and screened for voltage sensitivity in mammalian cells. Voltage sensitivity of FlicGR variants was then tested via field stimulation in HeLa cells. The process was repeated for several rounds.

The variants that most efficiently photoconverted from green to red and were bright in both the green and red channels were cultured and their plasmid DNA was used to transfect HeLa cells to test voltage sensitivity. The transfected cells were subjected to 10 ms electrical field pulses using a custom-built field stimulation system and fluorescence response to stimulation was recorded in the green channel (before photoconversion) and the red channel (after photoconversion). Variants that showed the highest voltage sensitivity in both channels were used as gene templates for the next round of directed evolution.

For our initial template, we fused cpmMaple from GR-GECO1.1 to the C-terminus of CiVSD truncated at residue 239. The linker joining both domains is a particularly important region of the chimeric protein since it is close to the chromophore and plays a pivotal role in relaying conformational changes from the VSD to cpFP domains. Accordingly, even small adjustments (i.e., single amino acid mutations or single residue deletions or insertions) in the linker between the VSD and the FP are expected to be critical to the indicator function. To identify the optimal composition of the linker, we randomized the codons for two residues immediately following residue 239 of CiVSD (P240 and P241). Screening

of this library for green to red photoconversion, followed by voltage sensitivity tests in HeLa cells subjected to field stimulation, led to the identification of a variant with mutations P240R and P241H. We designated this variant as our first generation Fluorescent indicator for voltage imaging - Green to Red (FlicGR0.1). FlicGR0.1 photoconverted from green to red when illuminated with violet light and exhibited dim green and dim red fluorescence that was responsive to membrane potential changes in mammalian cells.

To evolve FlicGR0.1 brightness and voltage sensitivity we used multiple rounds of directed protein evolution, where each round consisted of construction and screening of a library of thousands of variants. In a typical round of directed evolution, we used error-prone PCR to create a large library based on our most promising template(s), and then screened the library using the workflow represented in Figure 4-1. A mixture of the 3 to 6 variants with the brightest fluorescence, most efficient photoconversion, expected pattern of membrane localization, and largest responses to changes in voltage, would be typically used as the template for the next round of library creation by random mutagenesis. Six rounds of this procedure led to FlicGR0.7, which was 10 ± 2-fold brighter than FlicGR0.1 (n = 100 colonies) in the green channel and 12 ± 2-fold brighter than FlicGR0.1 (n = 100 colonies) in the red channel (Figure 4-2), in the context of bacterial colonies.
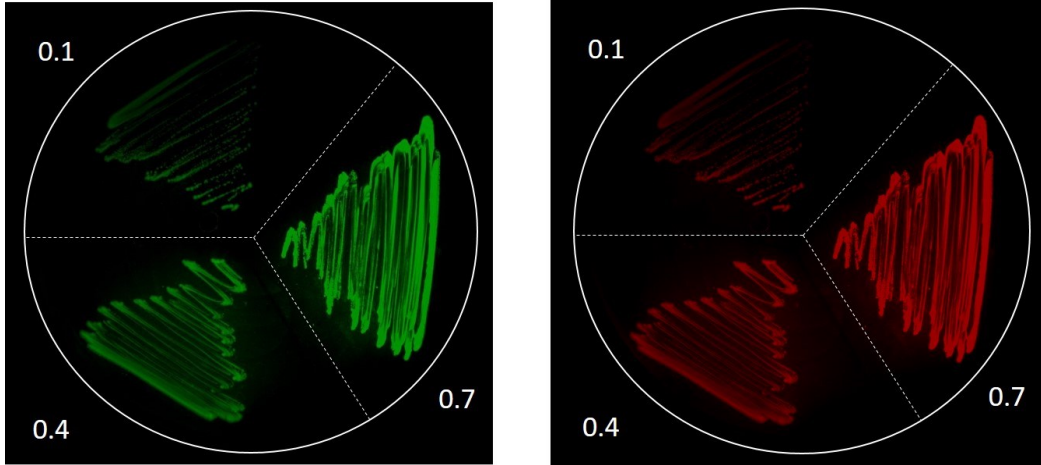
Figure 4-2 Evolution of FlicGR brightness in *E. coli*. Left: Green fluorescence image of *E. coli* expressing various FlicGR variants using pcDuEx0.5 before photoconversion. Right: Red fluorescence image of the same agar plate after photoconversion with 405 nm light.

Figure 4-3 Sequence alignment of FlicGR0.7. Alignment of FlicGR0.7 gene with the CiVSD domain (top) and cpmMaple from GR-GECO1.1 (bottom). Blue highlighted residues are amino acid mutations in the CiVSD domain carried forward from our work on FlicR1 (Chapter 2). Residues highlighted in red are mutations with respect to the starting template. Residues HYG in the box correspond to the mMaple chromophore.

FlicGR0.7 could be readily imaged by widefield fluorescence microscopy when expressed in mammalian cells. FlicGR0.7 exhibited a

decrease in both the green and red fluorescent channels in response to membrane depolarization (Figure 4-4 and Figure 4-5). Compared to the original template, FlicGR0.7 harboured a total of nine mutations: two mutations in the VSD and seven mutations in cpmMaple (Figure 4-3).
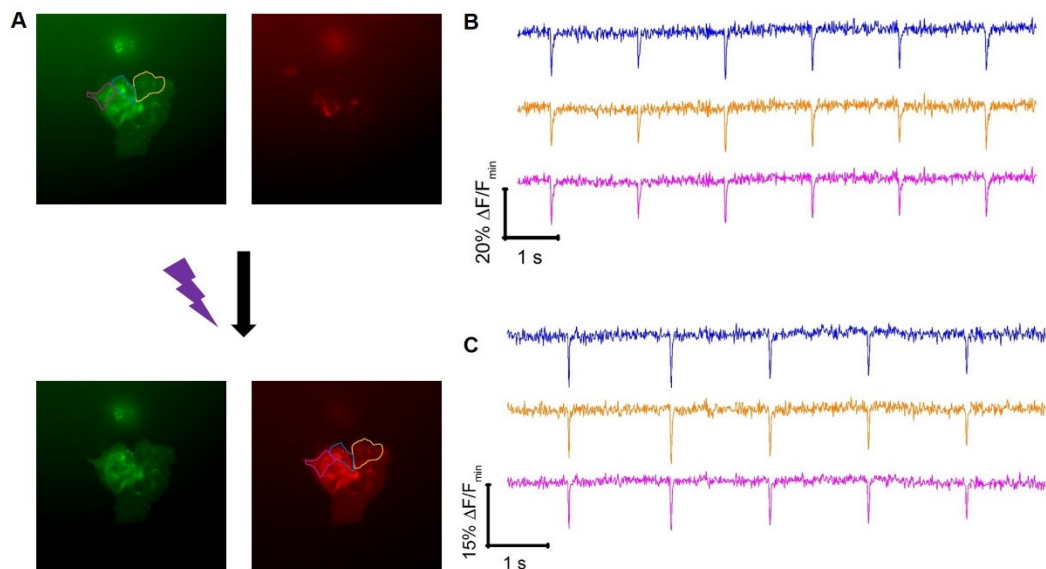
Figure 4-4 FlicGR0.7 fluorescence response to ITV in HeLa cells. (A) Image of HeLa cells expressing FlicGR0.7 before (Top) and after (bottom) photoconversion in the green and red channels. (B) FlicGR0.7 green fluorescence response of three regions shown in (A) to electrical field stimulation pulses (10 ms, 25 V). (C) FlicGR red fluorescence response of the same three regions shown in (A) to electrical field stimulation pulses (10 ms, 25 V) after photoconversion. Fluorescence imaging for field stimulation measurements was performed at 100 Hz. Illumination intensities were 0.2 W/cm^2 for both the green and red channels.
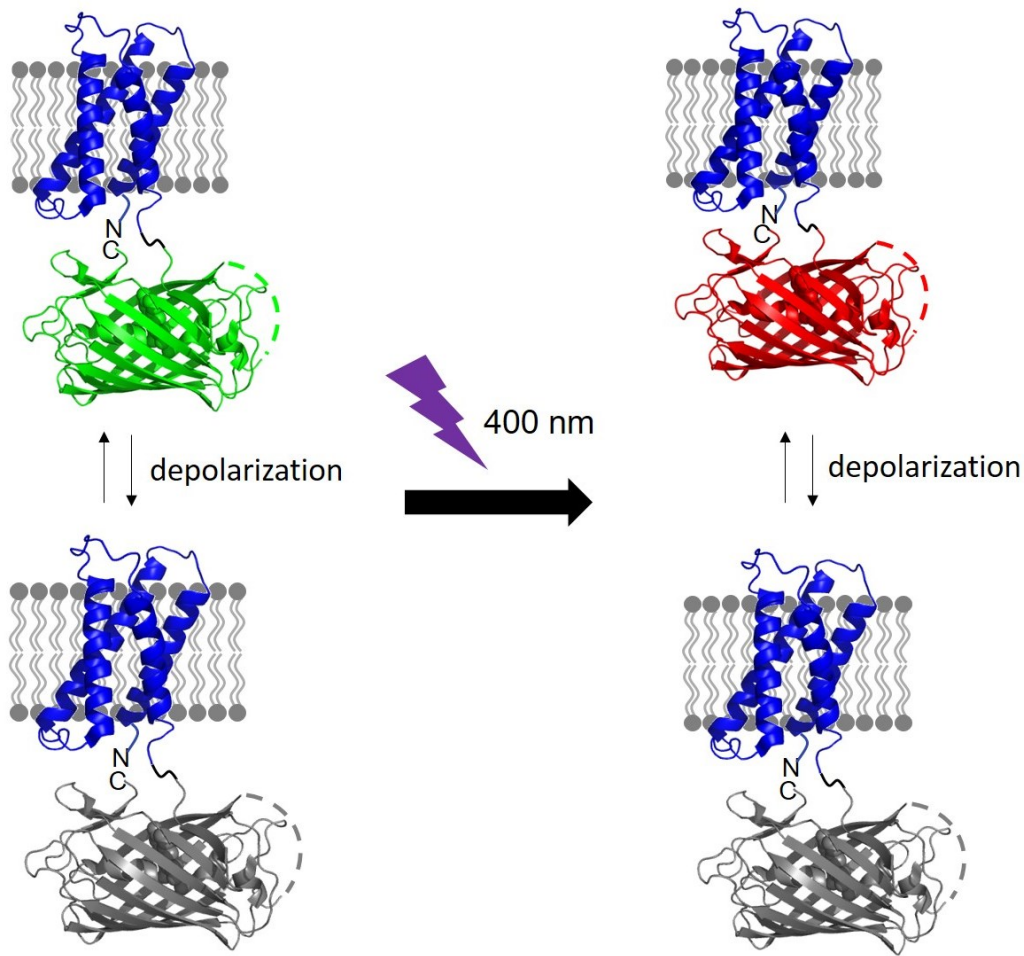
Figure 4-5 Schematic of FlicGR voltage sensitivity and photoconversion. In the original green state before photoconversion, FlicGR decreases in green fluorescence when the membrane is depolarized. Using 400 nm light, FlicGR is irreversibly converted from green to red. The red fluorescent state is sensitive to voltage changes and decreases in fluorescence when the membrane is depolarized.

4.2.2 Attempts to improve the brightness and voltage sensitivity of FlicGR0.7 to report neuronal activity

Having improved its brightness and voltage sensitivity compared to the original template, we expressed FlicGR0.7 in dissociated hippocampal

neurons. FlicGR0.7 targeted properly to the plasma membrane of neurons and successfully photoconverted from green to red when illuminated with violet light (Figure 4-6). Unfortunately, FlicGR0.7 did not produce measurable fluorescence responses to either spontaneous or stimulated activity in neurons. Although FlicGR0.7 can detect 10 ms ITV in HeLa cells (Figure 4-4), true action potentials in neurons are ~ 10 times shorter in duration (~ 1 ms). We suspect that using widefield fluorescence imaging probably meant that FlicGR0.7 fluorescence response to voltage was insufficient to have a detectable signal-to-noise ratio to report rapid neuron firing in single-trial recordings.

In an attempt to improve the brightness and sensitivity of FlicGR0.7 (which would in turn improve signal-to-noise ratio), we turned to additional directed evolution of FlicGR0.7 and also tried other cpFPs (i.e., cpmMaple from GR-GECO1.2 and cpmEos2 from CaMPARI). Further directed evolution of FlicGR0.7 did not result in improved variants with regards to brightness or response to voltage. Variants with cpmMaple from GR-GECO1.2 showed much smaller response to ITV in HeLa cells compared to FlicGR0.7. Variants tested that were based on cpmEos2 did not show response to ITV in HeLa cells. Altogether, these efforts did not yield variants with improved brightness or response amplitude compared to FlicGR0.7 to enable detection of neural activity (typically on the millisecond timescale) in single trial recordings using a widefield fluorescence imaging setup.
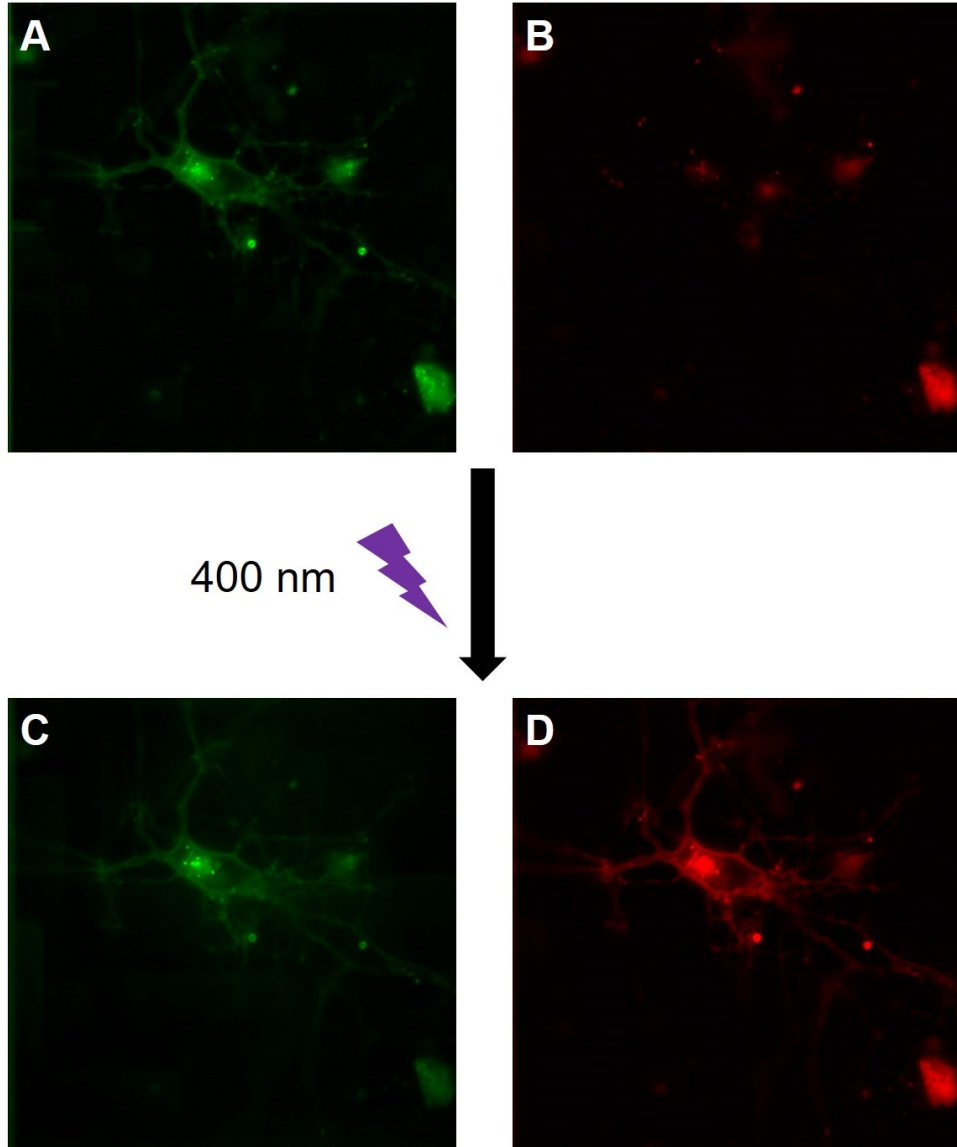
Figure 4-6 FlicGR0.7 imaging in neurons. (A-B) Image of cultured hippocampal neuron expressing FlicGR0.7 in the green channel (A) and red channel (B) before photoconversion. (C-D) Image of cultured hippocampal neuron expressing FlicGR0.7 in the green channel (C) and red channel (C) after photoconversion.

4.2.3 Attempts to engineer a voltage integrator

We reasoned that FlicGR0.7 could potentially act as a light-dependent voltage integrator. FlicGR0.7 responds to membrane depolarization with a decrease in fluorescence (Figure 4-4 and Figure 4-5). Accordingly, we reasoned that the protonated (non-fluorescent) form of the chromophore would be more abundant in an active cell undergoing frequent membrane potential changes relative to a less active cell with infrequent membrane depolarization (Figure 4-7). Because photoconversion proceeds through the non-fluorescent protonated form of the chromophore, as described in the introductory chapter (Figure 1-5), we hypothesized that FlicGR might photoconvert more efficiently when present in a more active cell (Figure 4-7). When illuminated with violet light, the cells that are active (undergoing frequent depolarization events) would be irreversibly labeled with red fluorescence compared to the less active, green fluorescent cells. This phenomenon of varying photoconversion efficiency has been utilized to engineer the Ca^{2+} integrator CaMPARI (*220*). CaMPARI photoconverts from green to red 21 times faster in the presence of Ca^{2+} allowing *post hoc* analysis of the activity of entire brain regions (using Ca^{2+} ion concentration as a proxy for activity) (*220*).
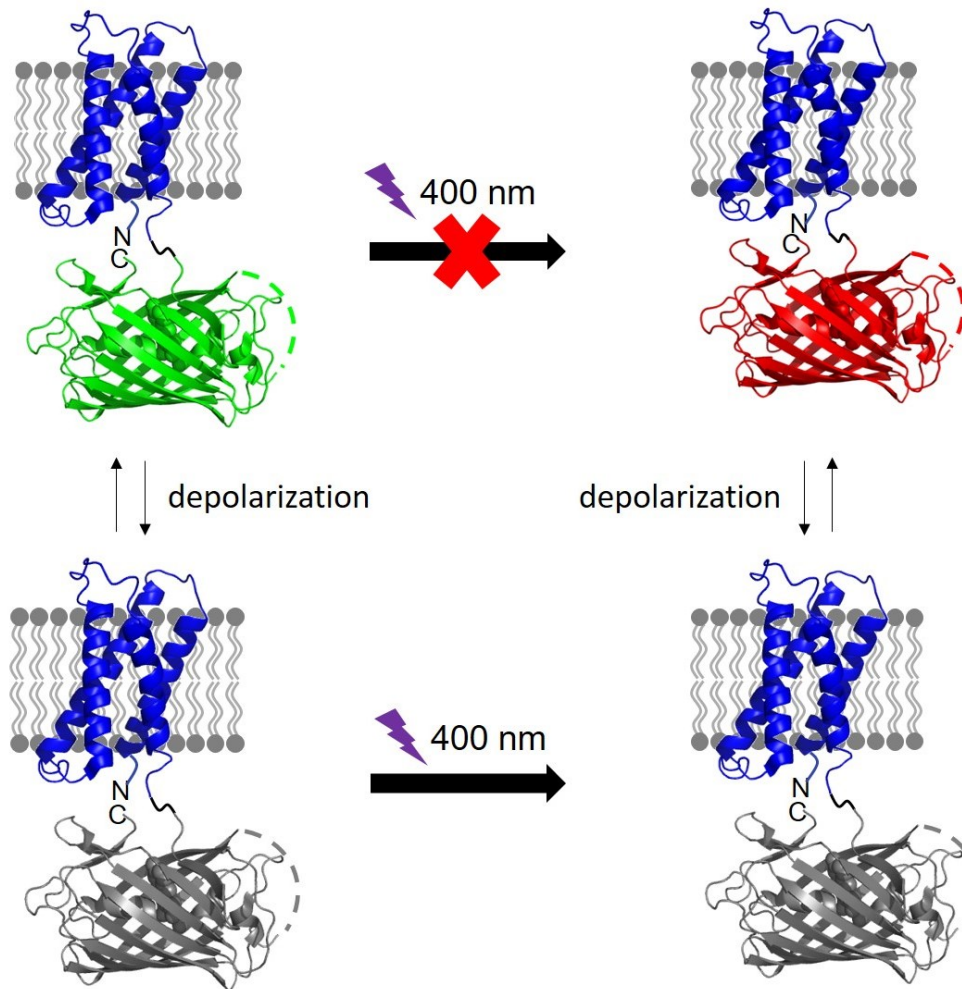
Figure 4-7 Schematic of a hypothetical FlicGR-derived voltage integrator. In an active cell with frequent membrane depolarization, the protonated non-fluorescent form of FlicGR would be more abundant, and can therefore be photoconverted more efficiently in comparison with a less active cell. Over time, the red species would accumulate in proportion to the number of action potentials in a particular cell.

To test this hypothesis, HeLa cells transfected with FlicGR0.7 were illuminated with violet light and their photoconversion rate measured. The rate of photoconversion was then compared to the photoconversion rate

when cells were simultaneously illuminated with violet light and subjected to electric field pulses (10 Hz, 25 V, 10 ms/pulse) (Figure 4-8). However, we did not observe a significant difference in photoconversion rate (comparing light alone to light plus electric field pulses) with FlicGR0.7 or other FlicGR variants (Figure 4-8).
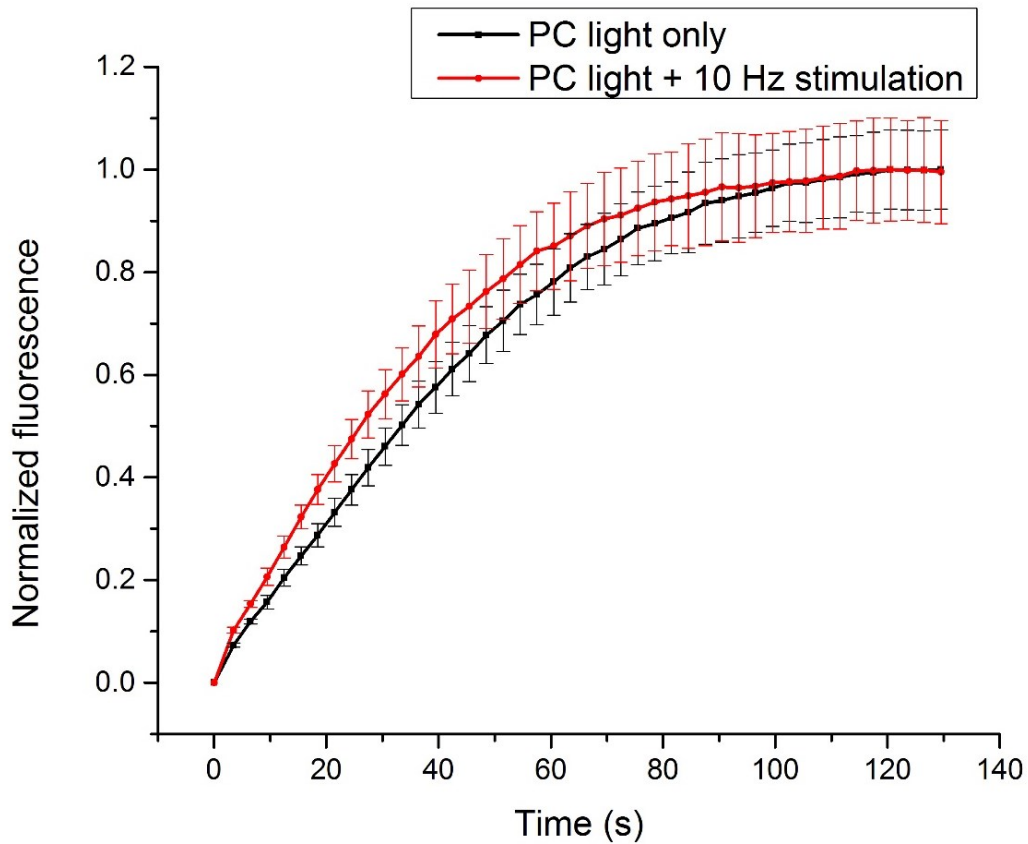
Figure 4-8 Photoconversion rate of FlicGR0.7 in HeLa cells. Black trace: Normalized red fluorescence in the absence of stimulation (n = 8). Red trace: Normalized red fluorescence with field stimulation of HeLa cells (25 V, 10Hz, 10 ms) (n = 6). A 405 nm laser (20 mW/cm^2) was used for photoconversion.

In additional efforts, we explored the use of cpmEos2 (derived from CaMPARI) in place of cpmMaple to engineer FlicGR variants that would integrate voltage. We fused cpmEos2 from CaMPARI with the C-terminus of CiVSD truncated at residue 239 and randomised two residues at the junction between the two domains. This library was screened for brightness and photoconversion in *E. coli* bacterial colonies as described previously. The variants that exhibited fluorescence and photoconversion were cultured and their plasmid DNA was used to transfect HeLa cells to test for voltage integration. Transfected HeLa cells were illuminated with violet light and their photoconversion rate measured. The rate of photoconversion was then compared to the photoconversion rate when cells were simultaneously illuminated with violet light and subjected to electric field pulses (10 Hz, 25 V, 10 ms/pulse). However, all the variants we screened showed dim brightness and no voltage integration.

4.3 Conclusion

A powerful application of FPs is their use as highlighters where they can be converted from one colour to another by light. In this Chapter I described the engineering of FlicGR0.7, which is the first example of a highlightable voltage indicator. Using a chimera of CiVSD and cpmMaple, I was able to generate a construct that photoconverts from a green fluorescent form to a red fluorescent state upon violet light illumination. Furthermore, I demonstrated that both the green and red fluorescent forms exhibit changes in fluorescence in response to membrane potential

changes in mammalian cells. Although I was unable to detect single action potentials in neurons using FlicGR0.7, I believe that further improved variants with brighter fluorescence and improved voltage sensitivity could be useful for imaging of neuronal activity.

I also attempted to construct a light-dependent voltage integrator that could be used to record neural activity without the need for real-time monitoring. However, I was unable to generate a successful prototype using either mMaple or mEos2 FPs. Because our screening methodology was limited to screening of only hundreds of variants in mammalian cells, we probably did not screen a sufficiently large swath of protein sequence space to identify a practically useful voltage integrator. A more streamlined high throughput mammalian screen would be helpful for future efforts to generate a voltage integrator.

4.4 Materials and methods

Molecular biology to construct FlicGR variants. Polymerase chain reaction (PCR) amplification was used to construct the DNA template for FlicGR. Synthetic oligonucleotides (Integrated DNA Technologies) were used as primers for amplification and Pfu polymerase (Thermo Fisher Scientific) was used to maintain high fidelity DNA replication. Overlap PCR was used to link CiVSD to cpmMaple and cpmEos2 FPs. Random mutagenesis was performed with error-prone PCR amplification using Taq polymerase (New England Biolabs) in the presence of $MnCl_2$ (0.1 mM), 200 µM dATP, 200 µM dGTP, 1000 µM dTTP, and 1000 µM dCTP.

Randomization of targeted codons was performed with QuikChange Lightning kits (Agilent Technologies). Restriction endonucleases (Thermo Fisher Scientific) were used to digest PCR products and expression vectors. Agarose gel electrophoresis was used to purify DNA products from PCR and restriction digestion reactions. The DNA was extracted from the gels using the GeneJET gel extraction kit (Thermo Fisher Scientific). Ligations were performed using T4 DNA ligase (Thermo Fisher Scientific).

DNA encoding the first 239 amino acids from CiVSD (VSD239) was generated by PCR amplification of CiVSD domain from the voltage sensor FlicR1 (*219*). DNA encoding the cpmMaple variant was generated by PCR amplification of the gene encoding GR-GECO1.1. Overlap PCR was used to join the two genes together. The photoconvertible cpFP was varied (cpmMaple from GR-GECO1.2 and cpmEos2 from CaMPARI) and similar overlap PCR reactions were used to construct the respective templates. Staggered extension process (StEP) recombination using low fidelity Taq polymerase (New England Biolabs) was used to construct libraries in directed evolution rounds that had more than one FlicGR template (winners from previous round). StEP PCR was performed in the presence of 0.1 mM $MnCl_2$, 200 μM dATP, 200 μM dGTP, 1000 μM dTTP, and 1000 μM dCTP.

Plasmids for *E. coli* and mammalian cell expression. We used pcDuEx0.5 (described previously in Chapter 2, Materials and Methods) as the vector for expression of the constructs in *E. coli* and HeLa cells. The

gene was inserted between *BamHI* and *XbaI* restriction sites. For expression of variants in neurons, genes were cloned from plasmid pcDuEx0.5 into the *BamHI* and *HindIII* sites of pAAV2 vector (Addgene: 61249). Expression was controlled using human synapsin I promoter to preferentially express in neurons. A 3' Woodchuck Hepatitis Virus Posttranscriptional Regulatory Element (WPRE) sequence was used to enhance expression.

Screening of FlicGR library variants in *E. coli*. Gene libraries of FlicGR variants were used to transform electro-competent *E. coli* strain DH10B (Invitrogen) by electroporation (10 kV/cm, ~ 5ms pulse) (MicroPulser™ Electroporator, BIO-RAD). *E. coli* cells were then plated and cultured at 37 °C on LB agar plates supplemented with ampicillin (400 µg/ml) to obtain 500-1000 colonies per plate. Colonies were imaged using a custom imaging setup described previously (*200*). To screen for FlicGR mutant brightness, plate images were acquired using a 470/40 nm excitation filter and 525/50 nm emission filter. The colonies were then photoconverted for 10-20 min using a custom built illumination source composed of six 9 × 11 arrays of 405 nm light emitting diodes (LED) (OptoDiode Corporation, Newbury Park, CA). Plate images were then acquired using a 560/40 nm excitation filter and 630/60 nm emission filter. For each round of random mutagenesis, ~10,000 colonies (10-20 plates) were screened. For each library generated by targeted codon randomization, ~3 times more colonies than the expected randomization

136

library size were screened. Colonies that exhibited bright green fluorescence before photoconversion and bright red fluorescence following photoconversion, were manually picked and cultured in 4 ml LB media supplemented with ampicillin (100 µg/ml). Plasmids were isolated from overnight cultures using GeneJET plasmid miniprep kit (Thermo Fisher Scientific).

Cell culture. HeLa cells (ATCC, CCL-2) were cultured in Dulbecco's modified Eagle's medium (DMEM) (supplemented with 10% fetal bovine serum (FBS) (Sigma), 2 mM GlutaMax (Invitrogen), penicillin-G potassium salt (50 units/ml), and streptomycin sulfate (50 µg/ml)) and the cells were incubated for 48 h at 37 °C, 5% CO_2. Cells were split and cultured on collagen-coated 35 mm glass bottom dishes (Matsunami) to ~50% confluency. Transfection was performed by incubating HeLa cells with a mixture of 1 µg of plasmid DNA and 2 µL of Turbofect (Thermo Fisher Scientific) for 2 h following the manufacturer's instructions. Imaging was performed 24-48 hours after transfection.

Dissociated E18 Sprague Dawley Hippocampal Cells in Hibernate® EB Complete Media were purchased from BrainBits LLC. The cells were grown on 35 mm glass bottom dishes (In Vitro Scientific) coated with poly-D-lysine (EMD Millipore, A-003-E) containing 2 ml of NbActiv4 (BrainBits LLC) supplemented with 2% FBS, penicillin-G potassium salt (25 units/ml), and streptomycin sulfate (25 µg/ml). Half of the culture media was replaced every 3 days. Neuronal cells were transfected on day 8 using

Lipofectamine 2000 (Life Technologies) following the manufacturer's instructions. Briefly, 1-2 µg of plasmid DNA and 4 µL of Lipofectamine 2000 (Life Technologies) were added to 100 µl of NbActive4 medium to make the transfection medium. This medium was then incubated at room temperature for 10-15 minutes. Half of the culture medium (1 ml) from each neuron dish was taken out and combined together with an equal volume of fresh NbActiv4 medium (supplemented with 2% FBS, penicillin-G potassium salt (25 units/ml), and streptomycin sulfate (25 µg/ml)) to make a 1:1 mixture and incubated at 37 °C and 5% CO_2. 1 ml of fresh conditioned (at 37 °C and 5% CO_2) NbActiv4 medium was then added to each neuron dish. The transfection medium was then added and the neuron dishes were incubated for 2-3 hours at 37 °C in a CO_2 incubator. The media was then replaced using the conditioned 1:1 medium prepared previously. The cells were incubated for 48-72 hours at 37 °C in a CO_2 incubator prior to imaging.

Induced transmembrane voltage (ITV) screening. FlicGR variants were co-expressed in HeLa cells, together with the inward rectifier potassium channel, Kir2.1 (Addgene: 32641). Expression of Kir2.1 in HeLa cells helped maintain the resting potential around -60 mV, which is appropriate for screening neuronal voltage indicators. A uniform electric field of ~50 V/cm was applied across the cell culture to create an ITV. A pulse generator (PG 58A, Gould Advance Ltd.) was used to apply a 10 ms square-wave pulse at ~0.5 Hz. An amplifier (6824A 40V/25A HP/Agilent)

138

was used to obtain a pulse amplitude of 25 V. A pair of parallel platinum electrodes (0.5 cm apart) were used to deliver the pulses to the cell culture. Fluorescence was imaged simultaneously with multiple electric field pulses for ITV at a frame rate of a 100 Hz for 10 seconds.

Imaging was carried out in HEPES (25 mM) buffered Hanks' Balanced Salt Solution (HBSS). An inverted fluorescence microscope (Eclipse Ti-E, Nikon) equipped with a 200 W metal halide lamp (PRIOR Lumen) and a 60× oil objective was used to image HeLa cells. Images were acquired at 100 Hz with 4×4 binning using a 16-bit QuantEM 512SC electron-multiplying CCD camera (Photometrics). A FITC/Cy2 filter set (470/40 nm (excitation), 525/50 nm (emission), and a 495LP dichroic mirror (set number 49002, Chroma)) was used to image FlicGR variants before photoconversion. A TRITC/Cy3 filter set (545/30 nm (excitation), 620/60 nm (emission), and a 570LP dichroic mirror (set number 49005, Chroma)) was used to image FlicGR variants after photoconversion. The NIS Elements Advanced Research software (Nikon) was used to control the microscope and camera. The raw fluorescence traces of FlicGR before and after photoconversion were extracted from identical regions of interest in cells, and exported into a customized Microsoft Excel spreadsheet. Background subtraction, photobleaching corrections, calculations of average $\Delta F/F_{min}$, were performed automatically in Excel.

Imaging primary neuron cultures. Imaging was carried out in HEPES (25 mM) buffered HBSS. Widefield imaging was performed on an

inverted Nikon Eclipse Ti-E microscope equipped with a 200 W metal halide lamp (PRIOR Lumen), 60× oil objectives (NA = 1.4, Nikon), and a 16-bit QuantEM 512SC electron-multiplying CCD camera (Photometrics). A FITC/Cy2 filter set (470/40 nm (excitation), 525/50 nm (emission), and a 495LP dichroic mirror (set number 49002, Chroma)) was used to image FlicGR variants in the green channel before photoconversion. A TRITC/Cy3 filter set (545/30 nm (excitation), 620/60 nm (emission), and a 570LP dichroic mirror, set number 49005, Chroma) was used to image FlicGR in the red channel after photoconversion. For attempted time-lapse imaging, neurons were imaged at 100 Hz imaging frequency with 4×4 binning.

Chapter 5 Development of a green fluorescent indicator for GABA

5.1 Introduction

γ-Aminobutyric acid (GABA) is the principal inhibitory neurotransmitter in the adult brain (*223*). An imbalance in GABA release relative to release of excitatory neurotransmitters results in increased activity of the brain causing pathologies like anxiety, epilepsy and schizophrenia (*224*, *225*). GABA also plays a critical role in neurogenesis and embryonic brain development (*226*, *227*). Abnormal GABA signalling results in neurodevelopmental disorders like autism and Down syndrome (*227*). Despite its important role in normal and disease physiology, current measurements of GABA release in the brain have poor spatiotemporal resolution. Tools that could enable the imaging of GABA signalling with high spatiotemporal resolution in animal models would shed light on normal physiological processes like brain development and would aid in understanding the various pathologies associated with imbalances in excitatory and inhibitory neurotransmitter release.

Estimates of GABA release in the brain have traditionally relied on *in vivo* microdialysis methods coupled with high performance liquid chromatography, capillary electrophoresis, and mass spectroscopy (*7*, *228*, *229*). However, microdialysis is an invasive technique, its temporal

resolution is on the order of minutes, and signals can only be attributed to areas of the brain rather than to single cells (*7*). Fluorescent indicators that are sensitive to GABA concentration would address many of these shortcomings. Specifically, if the fluorescent indicator was genetically encoded, it could be delivered to cells of interest by the relatively non-invasive methods of viral infection or transgenesis. Furthermore, if the indicator was engineered to have rapid kinetics, high speed fluorescence imaging would enable real-time monitoring of synaptic release events. Finally, fluorescence imaging of tissue expressing a GABA indicator would provide single-cell spatial resolution.

The only reported example of a prototype fluorescent indicator for GABA is GABA-Snifit (*230*). GABA-Snifit is a semi-genetically encoded fluorescent indicator that is based on the metabotropic $GABA_B$ receptor and a fluorescent antagonist as its synthetic ligand. The fluorescent synthetic ligand is tethered to the $GABA_B$ receptor using a SNAP-tag (*231*) that is fused with a CLIP-tag (*232*) labeled with a second fluorophore. Displacement of the synthetic ligand by GABA results in a change in FRET signal. GABA-Snifit has been used to detect GABA perfused on the surface of HEK cells, but has not been used in neurons to the best of my knowledge (*232*).

In this chapter, we describe our attempts to engineer a genetically encoded indicator for GABA by fusing GFP with a bacterial GABA-binding protein. Bacterial periplasmic binding proteins (PBPs) present a potentially

142

useful pool of naturally occurring proteins that bind small molecule ligands. They consist of two domains connected by a hinge region, with the ligand-binding site between the two domains. When the ligand binds, the two domains move relative to each other in a Venus flytrap manner (*233*, *234*). This phenomenon has been used to engineer indicators for many small molecules (*235*, *236*). For example, indicators for glutamate, the main excitatory neurotransmitter, have been engineered based on a glutamate-binding PBP (*16*, *17*, *123*). To construct a genetically encoded GABA indicator, a GABA-binding domain that undergoes a significant conformational change is required to relay a GABA-dependant conformational change to a fused FP chromophore. Accordingly, we used a GABA-binding PBP from *Agrobacterium tumefaciens* and a circularly permutated GFP to design a genetically encoded indicator for GABA.

5.2 Results

5.2.1 Designing the FP-based GABA indicator: GABA-G

To construct an FP-based GABA indicator, we searched the literature for an appropriate GABA-binding domain that undergoes a substantial conformational change upon binding to GABA. Preliminary evidence had suggested that the plant bacterial pathogen *Agrobacterium tumefaciens* may harbour a GABA-binding PBP (*237*). Building on this work, Planamente *et al.* isolated the selective GABA-binding PBP Atu4243 from *A. tumefaciens* and solved the X-ray crystal structures for both the

143

unbound open form and the GABA-bound closed form (*238*). As with other PBPs, GABA binds at the interface between the two domains of Atu4243 causing a global change in conformation of the two domains relative to each other (Figure 5-1A). We reasoned that we could construct a genetically encoded GABA indicator by analyzing the conformational change between the open and closed crystal structures of Atu4243, and rationally identifying an insertion site for a circularly permutated GFP.
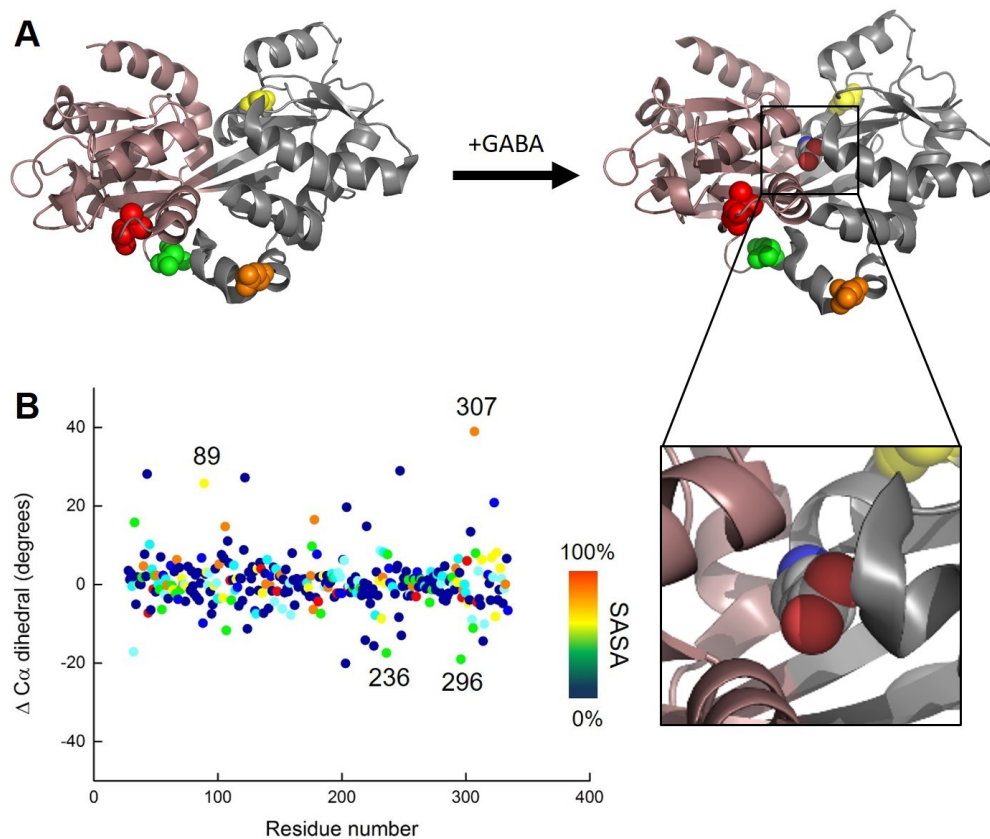
Figure 5-1 Conformational changes of Atu4243 and possible insertion points for cpGFP. (A) Cartoon representation of the free unbound form of Atu4243 (PDB ID: 4EQ7) and the GABA-bound form of Atu4243 (PDB ID: 4EUO). The N-terminal domain is coloured in gray and the C-terminal

domain is coloured in magenta. In the GABA-bound form, GABA is represented as spheres in the cleft between the two domains. The residues where cpGFP was inserted are shown as coloured spheres; yellow: 89, red: 236, orange: 296, and green: 307. Inset: Zoom in on GABA binding site. (B) Calculation of the change in backbone Cα dihedral angle as a measure of change in backbone orientation between the open and closed form of Atu4243. The Cα dihedral at each residue is calculated from four Cα's: $C\alpha_{i+2}$, $C\alpha_{i+1}$, $C\alpha_i$, $C\alpha_{i-1}$. Solvent accessible surface area (SASA) was also calculated for all residues and color-coded as shown in (B). The areas near residues 89, 236, 296 and 307 are labeled. Cartoon representations in (A) are prepared using PyMol (*31*).

5.2.2 Identifying insertion sites in Atu4243

To guide rational design of an FP-based GABA indicator, we computationally analyzed the unbound open form (PDB 4EQ7) and the GABA-bound closed form (PDB ID: 4EUO) of Atu4243 in order to locate plausible insertion sites for cpGFP. We examined the crystal structures for GABA-dependent conformational changes by computing the backbone dihedral angles (defined by four consecutive Cα atoms (*239*)) of both the open and closed form. The larger the change in dihedral angle at a specific residue of Atu4243, the larger the change in conformation caused by GABA binding. This calculation showed that the protein backbone undergoes twists around residues 89 (ΔCα dihedral = +26°), 236 (ΔCα dihedral = -18°), 296 (ΔCα dihedral = -19°) and 307 (ΔCα dihedral = +39°) upon binding to GABA. We hypothesized that inserting a circularly permutated GFP at these specific locations would give the greatest

chance of relaying a GABA-dependant conformational change to the FP chromophore.

Although we identified a number of promising insertion points using our analysis of dihedral angle changes between the open and closed forms of Atu4243, our analysis provides little insight into the expectedly complex nature of conformational coupling between Atu4243 and a fused cpGFP. To maximize our chances of coupling conformational changes in Atu4243 to the FP chromophore environment, we constructed four libraries in which the cpGFP was fused in place of residues 89, 236, 296 or 317 of Atu4243, with the residues at the junctions between the two domains fully randomized. The resulting libraries were expressed in a pBAD/His B vector in *E. coli*. We screened these four libraries for green fluorescence (a strong indicator of proper protein folding) on agar plates, followed by measuring fluorescence intensity of cell lysates in the absence and presence of 10 mM GABA.

Libraries in which cpGFP was inserted at positions 89 and 236 yielded non-fluorescent *E. coli* colonies, indicating that the protein did not fold properly. Libraries in which cpGFP was inserted at positions 296 and 307 yielded dim fluorescent colonies. We picked the fluorescent colonies and tested the dim protein variants for sensitivity to GABA. We identified a variant in the library with cpGFP insertion at position 307 which had a ~20% decrease in green fluorescence emission intensity upon binding to GABA. We designated this variant as GABA-G0.1 (Figure 5-2). GABA-

G0.1 carries mutations Gln306Arg and Thr552Gln in the linkers at the fusion sites between Atu4243 and cpGFP (Figure 5-3). In addition, we noticed that there is a ratiometric change in relative excitation intensity between the 488 nm and 400 nm excitation peaks upon binding to GABA, indicating a change in the chromophore environment (Figure 5-2). This ratiometric change in the excitation profiles suggests that the binding to GABA stabilizes the protonated form of the chromophore. GABA-G0.1 had dim basal fluorescence and a modest change in fluorescence intensity upon binding to GABA. Next, we used directed evolution to improve its brightness and fluorescence response to GABA.

Figure 5-2 Normalized excitation and emission spectra of GABA-G0.1 with

or without 10 mM GABA. GABA-free spectra are shown as a green line. GABA-bound spectra are shown as black lines.

```
Residue #   1  2  3  4  5  6  7  8  9 10 11 12 13 14 15 16 17 18 19 20 21 22 23 24 25 26 27 28 29 30 31 32 33 34 35 36 37 38 39 40
Atu4243     M  R  S  K  L  V  L  S  T  C  A  A  L  F  A  L  G  A  A  A  Q  A  N  D  L  V  F  S  S  W  G  G  T  T  Q  D  A  Q  K  A
cpGFP       -  -  -  -  -  -  -  -  -  -  -  -  -  -  -  -  -  -  -  -  -  -  -  -  -  -  -  -  -  -  -  -  -  -  -  -  -  -  -  -
GABA-G      M  R  S  K  L  V  L  S  T  C  A  S  L  S  A  P  G  A  A  A  Q  A  N  D  L  V  F  S  S  W  G  G  T  T  Q  D  A  Q  K  A

Residue #  41 42 43 44 45 46 47 48 49 50 51 52 53 54 55 56 57 58 59 60 61 62 63 64 65 66 67 68 69 70 71 72 73 74 75 76 77 78 79 80
Atu4243     A  W  A  E  K  F  M  V  E  T  G  I  N  V  L  Q  D  G  P  T  D  Y  G  K  L  K  A  M  V  E  A  N  G  V  T  W  D  V  V  D
cpGFP       -  -  -  -  -  -  -  -  -  -  -  -  -  -  -  -  -  -  -  -  -  -  -  -  -  -  -  -  -  -  -  -  -  -  -  -  -  -  -  -
GABA-G      A  W  A  E  K  F  M  V  E  T  G  I  N  V  L  Q  D  G  P  T  D  Y  G  K  L  K  A  M  V  E  A  N  G  V  T  W  D  V  V  D

Residue #  81 82 83 84 85 86 87 88 89 90 91 92 93 94 95 96 97 98 99 100 101 102 103 104 105 106 107 108 109 110 111 112 113 114 115 116 117 118 119 120
Atu4243     V  E  G  D  Y  A  A  Q  A  G  P  K  G  L  L  E  K  L  D  F  S  V  I  D  K  T  K  L  D  P  R  F  V  T  D  Y  S  V  G  S
cpGFP       -  -  -  -  -  -  -  -  -  -  -  -  -  -  -  -  -  -  -  -  -  -  -  -  -  -  -  -  -  -  -  -  -  -  -  -  -  -  -  -
GABA-G      V  E  G  D  Y  A  A  Q  A  G  P  K  G  L  L  E  K  L  D  F  S  V  I  D  K  T  K  L  D  P  R  F  V  T  D  Y  S  V  G  S

Residue # 121 122 123 124 125 126 127 128 129 130 131 132 133 134 135 136 137 138 139 140 141 142 143 144 145 146 147 148 149 150 151 152 153 154 155 156 157 158 159 160
Atu4243     F  Y  Y  S  F  V  I  G  C  N  V  D  S  V  S  A  C  P  K  S  W  A  D  L  F  D  T  A  K  F  P  G  K  R  T  F  Y  K  W  S
cpGFP       -  -  -  -  -  -  -  -  -  -  -  -  -  -  -  -  -  -  -  -  -  -  -  -  -  -  -  -  -  -  -  -  -  -  -  -  -  -  -  -
GABA-G      F  Y  Y  S  F  V  I  G  C  N  V  D  S  V  S  A  C  P  K  S  W  A  D  L  F  D  T  A  K  F  P  G  K  R  T  F  Y  K  W  S

Residue # 161 162 163 164 165 166 167 168 169 170 171 172 173 174 175 176 177 178 179 180 181 182 183 184 185 186 187 188 189 190 191 192 193 194 195 196 197 198 199 200
Atu4243     A  P  G  V  I  E  A  A  L  L  A  D  G  V  T  A  D  K  L  Y  P  L  D  L  D  R  A  F  K  K  L  D  T  I  K  S  D  I  I  W
cpGFP       -  -  -  -  -  -  -  -  -  -  -  -  -  -  -  -  -  -  -  -  -  -  -  -  -  -  -  -  -  -  -  -  -  -  -  -  -  -  -  -
GABA-G      A  P  G  V  I  E  A  A  L  L  A  D  G  V  T  A  D  K  L  Y  P  L  D  L  D  R  A  F  K  K  L  D  T  I  K  S  D  I  I  W

Residue # 201 202 203 204 205 206 207 208 209 210 211 212 213 214 215 216 217 218 219 220 221 222 223 224 225 226 227 228 229 230 231 232 233 234 235 236 237 238 239 240
Atu4243     W  S  G  G  A  Q  S  Q  Q  L  I  A  S  A  E  A  P  F  G  S  V  W  N  G  R  M  T  A  L  E  Q  S  G  V  K  V  E  T  S  W
cpGFP       -  -  -  -  -  -  -  -  -  -  -  -  -  -  -  -  -  -  -  -  -  -  -  -  -  -  -  -  -  -  -  -  -  -  -  -  -  -  -  -
GABA-G      W  S  G  G  A  Q  S  Q  Q  L  I  A  S  A  E  A  P  F  G  S  V  W  N  G  R  M  T  A  L  E  Q  S  G  V  K  V  E  T  S  W

Residue # 241 242 243 244 245 246 247 248 249 250 251 252 253 254 255 256 257 258 259 260 261 262 263 264 265 266 267 268 269 270 271 272 273 274 275 276 277 278 279 280
Atu4243     A  Q  N  I  T  A  A  D  S  L  V  V  P  K  G  T  K  N  K  D  A  A  M  K  F  I  A  L  A  T  S  A  Q  A  Q  A  D  M  A  T
cpGFP       -  -  -  -  -  -  -  -  -  -  -  -  -  -  -  -  -  -  -  -  -  -  -  -  -  -  -  -  -  -  -  -  -  -  -  -  -  -  -  -
GABA-G      A  Q  N  I  T  A  A  D  S  L  V  V  P  K  G  T  K  N  K  D  A  A  M  K  F  I  A  L  A  T  S  A  Q  A  Q  A  D  M  A  T

Residue # 281 282 283 284 285 286 287 288 289 290 291 292 293 294 295 296 297 298 299 300 301 302 303 304 305 306 307 308 309 310 311 312 313 314 315 316 317 318 319 320
Atu4243     A  T  G  Y  A  P  V  N  I  E  S  A  K  L  M  D  P  K  I  A  K  S  L  P  D  Q
cpGFP                                                                             -  -  S  H  N  V  Y  I  M  A  D  K  Q  R  N  G
GABA-G      A  T  G  Y  A  P  V  N  I  E  S  A  K  L  M  D  P  K  I  A  K  S  L  P  D  R  S  H  N  V  Y  I  M  A  D  K  Q  R  N  G

Residue # 321 322 323 324 325 326 327 328 329 330 331 332 333 334 335 336 337 338 339 340 341 342 343 344 345 346 347 348 349 350 351 352 353 354 355 356 357 358 359 360
Atu4243     -  -  -  -  -  -  -  -  -  -  -  -  -  -  -  -  -  -  -  -  -  -  -  -  -  -  -  -  -  -  -  -  -  -  -  -  -  -  -  -
cpGFP       I  K  A  N  F  K  I  R  H  N  I  E  D  G  G  V  Q  L  A  Y  H  Y  Q  Q  N  T  P  I  G  D  G  P  V  L  L  P  D  N  H  Y
GABA-G      I  K  A  N  F  K  I  R  H  N  I  E  D  G  G  V  Q  L  A  Y  H  Y  Q  Q  N  T  P  I  G  D  G  P  V  L  L  P  D  N  H  Y

Residue # 361 362 363 364 365 366 367 368 369 370 371 372 373 374 375 376 377 378 379 380 381 382 383 384 385 386 387 388 389 390 391 392 393 394 395 396 397 398 399 400
Atu4243     -  -  -  -  -  -  -  -  -  -  -  -  -  -  -  -  -  -  -  -  -  -  -  -  -  -  -  -  -  -  -  -  -  -  -  -  -  -  -  -
cpGFP       L  S  T  Q  S  K  L  S  K  D  P  N  E  K  R  D  H  M  V  L  L  E  F  V  T  A  A  G  I  T  L  G  M  D  E  L  Y  K  G  G
GABA-G      L  S  T  Q  S  K  L  S  K  D  P  N  E  K  R  D  H  M  V  L  L  E  F  V  T  A  A  G  I  T  L  G  M  D  E  L  H  K  G  G

Residue # 401 402 403 404 405 406 407 408 409 410 411 412 413 414 415 416 417 418 419 420 421 422 423 424 425 426 427 428 429 430 431 432 433 434 435 436 437 438 439 440
Atu4243     -  -  -  -  -  -  -  -  -  -  -  -  -  -  -  -  -  -  -  -  -  -  -  -  -  -  -  -  -  -  -  -  -  -  -  -  -  -  -  -
cpGFP       T  G  G  S  M  V  S  K  G  E  E  L  F  T  G  V  V  P  I  L  V  E  L  D  G  D  V  N  G  H  K  F  S  V  S  G  E  G  E  G
GABA-G      T  G  G  S  M  V  S  K  G  T  E  L  F  T  G  V  V  P  I  L  V  E  L  D  G  D  V  N  G  H  K  F  S  V  S  G  E  G  E  G

Residue # 441 442 443 444 445 446 447 448 449 450 451 452 453 454 455 456 457 458 459 460 461 462 463 464 465 466 467 468 469 470 471 472 473 474 475 476 477 478 479 480
Atu4243     -  -  -  -  -  -  -  -  -  -  -  -  -  -  -  -  -  -  -  -  -  -  -  -  -  -  -  -  -  -  -  -  -  -  -  -  -  -  -  -
cpGFP       D  A [T  Y  G] K  L  T  L  K  F  I  C  T  T  G  K  L  P  V  P  W  P  T  L  V  T  T  L  T  Y  G  V  Q  C  F  S  R  Y  P
GABA-G      D  A  T  Y  G  K  L  T  L  K  F  I  C  T  T  G  K  L  P  V  P  W  P  T  L  V  T  T  L  T  Y  G  V  Q  C  F  S  R  Y  P

Residue # 481 482 483 484 485 486 487 488 489 490 491 492 493 494 495 496 497 498 499 500 501 502 503 504 505 506 507 508 509 510 511 512 513 514 515 516 517 518 519 520
Atu4243     -  -  -  -  -  -  -  -  -  -  -  -  -  -  -  -  -  -  -  -  -  -  -  -  -  -  -  -  -  -  -  -  -  -  -  -  -  -  -  -
cpGFP       D  H  M  K  Q  H  D  F  F  K  S  A  M  P  E  G  Y  I  Q  E  R  T  I  F  F  K  D  D  G  N  Y  K  T  R  A  E  V  K  F  E
GABA-G      D  H  M  K  Q  H  D  F  F  K  S  A  M  P  E  G  Y  I  Q  E  R  P  I  F  F  K  D  D  G  N  Y  K  T  R  A  E  V  K  F  E

Residue # 521 522 523 524 525 526 527 528 529 530 531 532 533 534 535 536 537 538 539 540 541 542 543 544 545 546 547 548 549 550 551 552 553 554 555 556 557 558 559 560
Atu4243                                                                                                            T  E  S  Q  V  N  A  D  M
cpGFP       G  D  T  L  V  N  R  I  E  L  K  G  I  D  F  K  E  D  G  N  I  L  G  H  K  L  E  Y  N  F  N  -  -  -  -  -  -  -  -  -
GABA-G      G  D  T  L  V  N  R  I  E  L  K  G  I  G  F  K  E  D  G  N  I  L  G  H  K  L  E  Y  N  F  N  Q  T  S  Q  V  N  A  D  M

Residue # 561 562 563 564 565 566 567 568 569 570 571 572 573 574 575 576 577 578 579 580
Atu4243     N  Y  W  A  Q  H  R  D  E  I  G  E  R  W  Y  A  W  Q  A  K
cpGFP       N  Y  W  A  Q  H  R  D  E  I  G  E  R  W  Y  A  W  Q  A  K
GABA-G      -  -  -  -  -  -  -  -  -  -  -  -  -  -  -  -  -  -  -  -
```
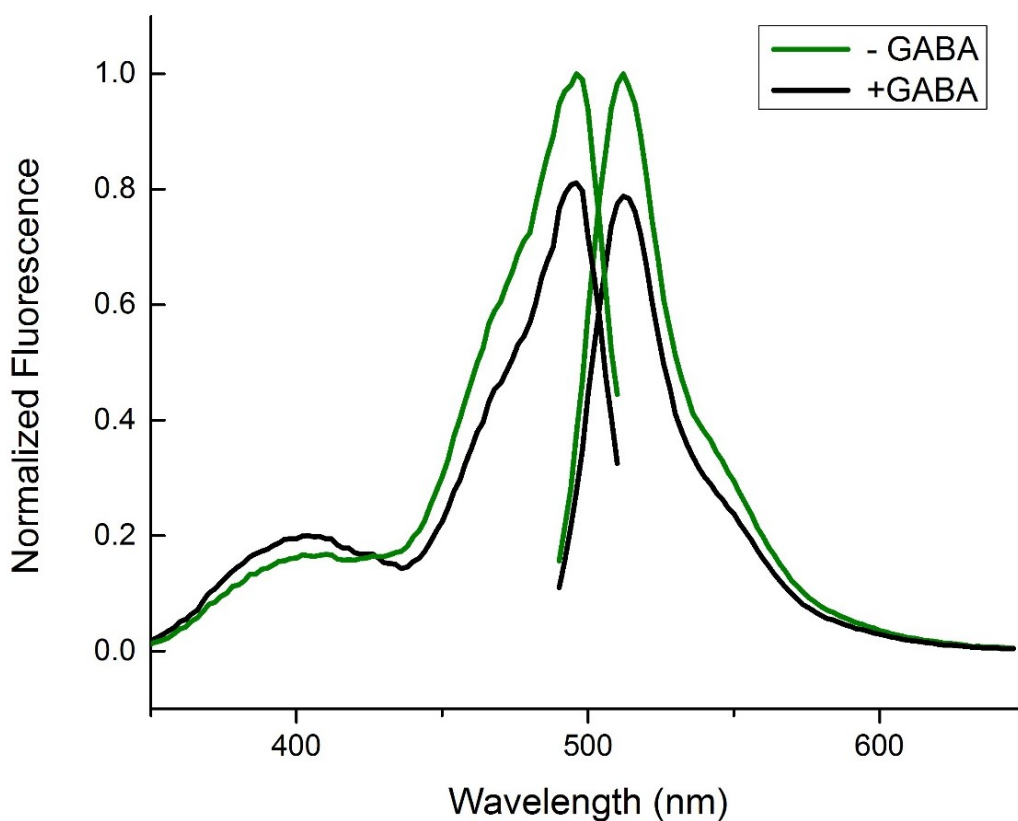
Figure 5-3 Sequence alignment of GABA-G1. Alignment of GABA-G1 gene with Atu4243 protein (top) and cpGFP from iGluSnFr (*16*) (middle). Green highlighted residues are amino acid mutations with respect to the starting template. Residues TYG in the box correspond to the GFP chromophore.

5.2.3 Directed evolution of GABA-G0.1

In an effort to improve the brightness and fluorescence response to GABA, we performed five rounds of directed evolution with selection for variants with bright green fluorescence and large fluorescence response to GABA. Specifically, we used error-prone PCR on the GABA-G0.1 gene cloned in the pBAD/His B vector, followed by a colony-based screen to select for variants that exhibit the brightest green fluorescence intensity. Bright variants were picked up and cultured. Proteins were then extracted from bacterial cultures and tested for their fluorescence response to GABA. For each round, approximately three to six variants that exhibited the brightest green fluorescence and the largest fluorescence response to GABA were used as templates for the next round of directed evolution.

These efforts led to the identification of GABA-G1 (derived from GABA-G0.1) with brighter basal fluorescence, a ~50% decrease of fluorescence intensity (~1-fold dynamic range) upon binding to GABA (Figure 5-4), and a K_d of 660 µM for GABA (Figure 5-5). GABA-G1 had 10 mutations relative to the initial template: four mutations in the GABA-binding domain, four mutations in the cpGFP, and two mutations in the linker joining the two domains (Figure 5-3).
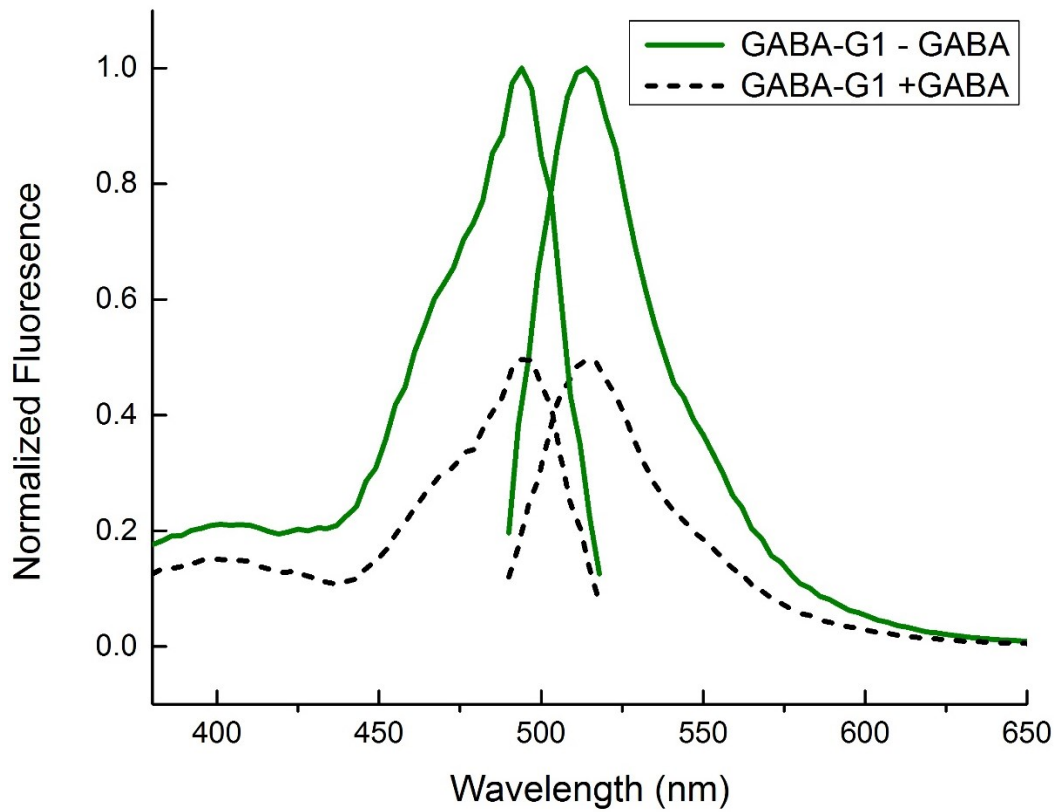
Figure 5-4 Normalized excitation and emission spectra of GABA-G1 with or without 10 mM GABA. GABA-free spectra are shown as solid green lines. GABA-bound spectra are shown as dotted black lines.
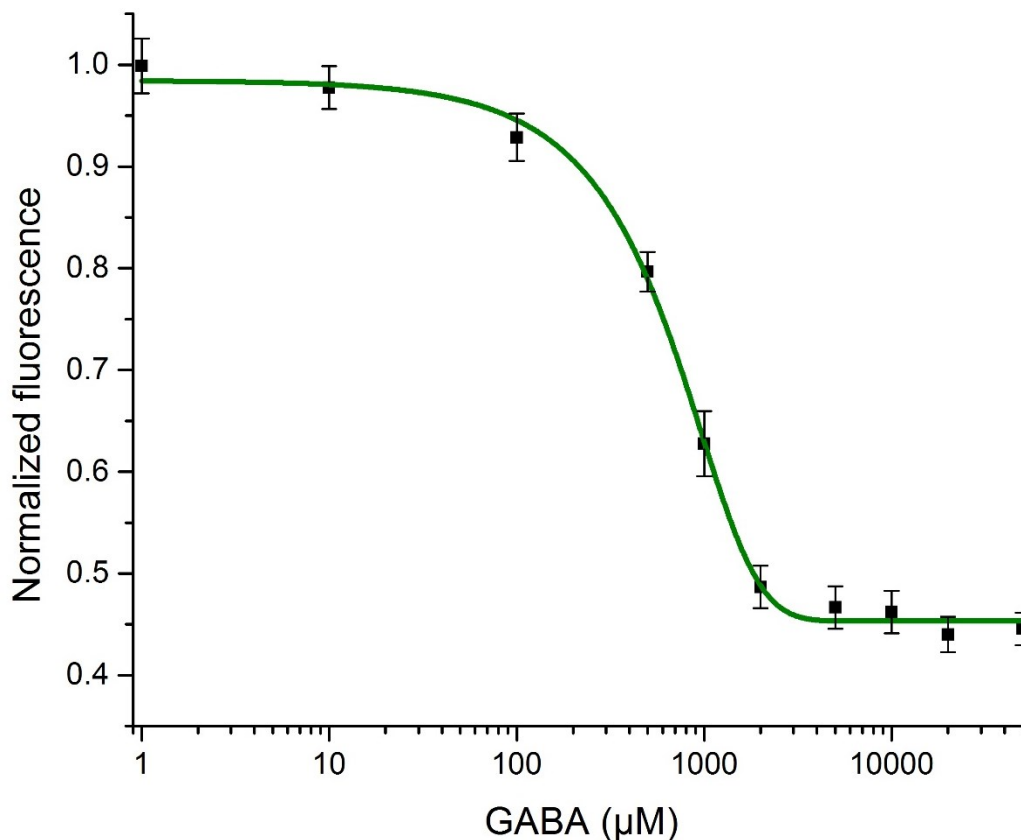
Figure 5-5 Normalized fluorescence emission of GABA-G1 as a function of varying GABA concentrations.

5.2.4 Live cell imaging using GABA-G1

Before proceeding further with more directed evolution to improve GABA-G1 fluorescence sensitivity to GABA and tune its K_d, we explored whether GABA-G1 could successfully report GABA concentrations when targeted to the surface of mammalian cells. We cloned GABA-G1 into a pDisplay vector under the control of a CMV promoter and transfected cultured HeLa and HEK cells. Although GABA-G1 was bright and could be imaged easily, it did not traffic properly to the plasma membrane and

instead appeared to be trapped in the endoplasmic reticulum of the cells (Figure 5-6).
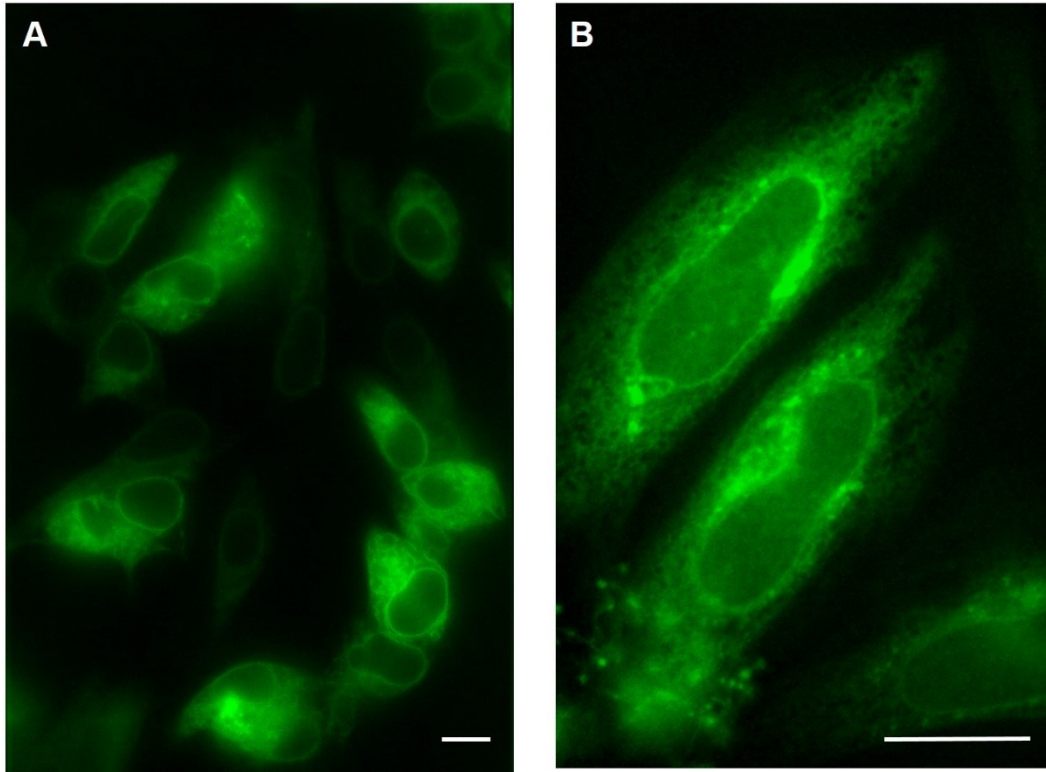
Figure 5-6 Live cell imaging of GABA-G1. (A) Image of HEK 293 cells expressing GABA-G1. Scale bar 10 μm. (B) Image of HeLa cells expressing GABA-G1. Scale bar 10 μm.

We attempted several strategies to export GABA-G1 to the plasma membrane of mammalian cells. First, we tried using several well-established signalling peptides. We fused one, two, or three tandem copies of an ER export sequence (FCEYENEV) (*240*) to the C- terminus of GABA-G1. We also added a Golgi export sequence (RSRFVKKDGHCNVQFINV) (*240*) to the N-terminus of GABA-G1.

Unfortunately, addition of these signalling peptides was not successful for exporting GABA-G1 from the ER. Second, we searched for possible signal peptide sequences (i.e., endoplasmic reticulum retention sequences) within the Atu4243 sequence and truncated the protein from the N-terminus up to residue 34 to avoid any N-terminal bacterial targeting sequences. Unfortunately, these modifications also did not change the protein trafficking in mammalian cells. Next we turned to changing the location of the protein termini by circularly permutating GABA-G1, in an effort to encompass the Atu4243 protein within the GFP scaffold. We used a twenty amino acid long flexible linker composed of glycine and serine to genetically fuse the N- and C-termini of Atu4243 and created new N- and C-termini between positions 398 and 405 (Figure 5-3). As with the other modifications attempted, this strategy did not change the trafficking of GABA-G1 when expressed in mammalian cells. We also tried fusing GABA-G1 between the S3 and S4 helices of GgVSD that is known to export cpGFP to the outer surface of the cell (*15*). Once again, this approach did not change GABA-G1's trafficking in mammalian cells. We later learned that other groups were also attempting to use Atu4243 and experiencing similar problems. In a personal communication, Lin Tian (University of California, Davis) said, "Though it (Atu4243) worked in purified protein as you experienced, we couldn't display it on the surface of (HEK) 293 cells no matter how hard we have tried."

5.3 Conclusion

By utilizing rational design and directed evolution, we developed a green FP-based indicator, designated GABA-G1, for the neurotransmitter GABA. We used the GABA-binding PBP from *Agrobacterium tumefaciens* and cpGFP to construct GABA-G1. By exploring backbone conformational changes of Atu4243 upon binding to GABA, we were able to identify four promising positions for inserting a cpGFP in the Atu4343 sequence. Insertion of cpGFP at position 307, followed by several rounds of directed evolution, ultimately led to GABA-G1 which exhibits a decrease in green fluorescence upon binding to GABA and has a 1-fold dynamic range *in vitro*. Although we tried several strategies to express GABA-G1 on the surface of mammalian cells, it remained trapped in the endoplasmic reticulum.

5.4 Materials and methods

Molecular biology to construct GABA-G variants. The gene for Atu4243 was synthesized based on GenBank entry AE007870.2 (gBlocks, Integrated DNA Technologies). Polymerase chain reaction (PCR) amplification of the gBlock Atu4343 gene was used to construct the DNA template for GABA-G0.1. Synthetic oligonucleotides (Integrated DNA Technologies) were used as primers for amplification and Pfu polymerase (Thermo Fisher Scientific) was used to maintain high fidelity DNA replication. Overlap PCR was used to link cpGFP from iGluSnFr

(Addgene: 41732) to Atu4243 gene at four insertion sites. DNA encoding the first 88, 235, 295 and 306 amino acids from Atu4243 was generated by PCR amplification of the Atu4243 gene. DNA encoding the cpGFP barrel was generated by PCR amplification of the gene encoding iGluSnFr. DNA encoding the remainder of Atu4243 90-336, 237-336, 297-336 and 308-336 was generated by PCR amplification of the Atu4243 gene. Overlap PCR was used to join the three fragments together. Error-prone PCR together with DNA shuffling were used to construct libraries in the following rounds of directed evolution on GABA-G templates. Random mutagenesis was performed with error-prone PCR amplification using Taq polymerase (New England Biolabs) in the presence of $MnCl_2$ (0.1 mM) and 800 μM excess dTTP and dCTP. Randomization of targeted codons was performed with QuikChange Lightning kits (Agilent Technologies). Restriction endonucleases (Thermo Fisher Scientific) were used to digest PCR products and expression vectors. Agarose gel electrophoresis was used to purify DNA products from PCR and restriction digestion reactions. The DNA was extracted from the gels using the GeneJET gel extraction kit (Thermo Fisher Scientific). Ligations were performed using T4 DNA ligase (Thermo Fisher Scientific). Plasmids used were pBAD/His B vector (Life Technologies) and pDisplay vector (Thermo Fisher Scientific).

Screening of GABA-G library variants in *E. coli*. Gene libraries of GABA-G variants were transformed into electro-competent *E. coli* strain DH10B (Invitrogen). *E. coli* cells were then plated and cultured at 37 °C on

LB agar plates supplemented with ampicillin (400 µg/ml) and 0.02% (wt/vol) L-arabinose (Alfa Aesar) to obtain 500-1000 colonies per plate. Colonies were then imaged using a custom imaging setup described previously (*200*). To screen for GABA-G mutant brightness, plate images were acquired using a 470/40 nm excitation filter. For each round of random mutagenesis, ~10,000 colonies (10 - 20 plates) were screened. For each library generated by codon randomization, ~3 times more colonies than the expected randomization library size were screened. Colonies that showed the highest 0.1% brightness were then picked and cultured in 4 ml liquid LB with 100 µg/ml ampicillin and 0.02% (wt/vol) L-arabinose at 37 °C overnight. *E. coli* cells were lysed and the proteins were extracted from the liquid LB culture using B-PER™ bacterial protein extraction reagent (Thermo Fisher Scientific). Protein variants were then subjected to a secondary test for fluorescence response to GABA using a Safire2 fluorescence microplate reader (Tecan). Plasmids of the variants with highest brightness and response to GABA were then extracted using GeneJET plasmid miniprep kit (Thermo Fisher Scientific).

Protein purification and characterization. *E. coli* strain DH10B (Invitrogen) was transformed by electroporation with a pBAD/His B containing GABA-G1. A single colony was used to inoculate a 4 ml culture that was grown overnight at 37 °C before being used to inoculate 100 ml of LB medium supplemented with ampicillin. This culture was grown at 37 °C to an optical density of 0.6, after which protein expression was induced

with 0.02% L-arabinose, and cultured for 48 h at 30 °C. Cells were then pelleted and lysed by a cell disruptor. GABA-G1 was then purified using Ni-NTA beads (Amersham). Fluorescence was recorded using a Safire2 fluorescence microplate reader (Tecan).

Cell culture. HeLa cells (ATCC, CCL-2) or HEK cells (CRL-11268) were cultured in Dulbecco's modified Eagle's medium (DMEM) (supplemented with 10% fetal bovine serum (FBS) (Sigma), 2 mM GlutaMax (Invitrogen), penicillin-G potassium salt (50 units/ml), and streptomycin sulfate (50 μg/ml)) and the cells were incubated for 48 h at 37 °C, 5% CO_2. Cells were split and cultured on collagen-coated 35 mm glass bottom dishes (Matsunami) to ~50% confluency. Transfection was performed by incubating HeLa cells with the mixture of 1 μg of plasmid DNA and 2 μL of Turbofect (Thermo Fisher Scientific) for 2 h following the manufacturer's instructions. Imaging was performed 24-48 hours after transfection.

Live cell imaging of GABA-G1 in HeLa and HEK cells. For imaging in mammalian cells, GABA-G1 was cloned into a p-Display vector (Thermo Fisher Scientific). This fuses the GABA-G1 protein to a platelet derived growth factor receptor transmembrane domain at the C-terminus that would anchor a protein cloned in p-Display to the plasma membrane. Imaging was carried out in HEPES (25 mM) buffered Hanks' Balanced Salt Solution (HBSS). HeLa and HEK cells were imaged using an Axiovert 200M (Zeiss) microscope (Zeiss) equipped with a 75 W xenon-arc lamp,

40× objective lens (NA = 1.3, oil) and a 14-bit CoolSnap HQ2 cooled CCD camera (Photometrics). An open source software; Micro-Manager, was used to control the microscope and camera. A FITC/Cy2 filter set (470/40 nm (excitation), 525/50 nm (emission), and a 495LP dichroic mirror (set number 49002, Chroma)) was used to image GABA-G1.

Chapter 6 Conclusions and future directions

The ability to visualize the spatiotemporal activity of populations of neurons has opened new avenues to understand complex brain functions in modern neuroscience. Fluorescence microscopy is currently the most powerful imaging technique for interrogation of neural circuits. Accordingly, tremendous efforts have been invested in engineering FPs to act as indicators for various biochemical processes in neural circuits, resulting in a plethora of genetically encoded FP-based indicators for neural imaging.

Biochemical changes relevant to neural activity for which indicators have been developed include Ca^{2+} ion concentration (*11–13*), membrane potential (*14*, *15*), and the neurotransmitter glutamate (*16*, *17*, *123*). Although Ca^{2+} ion concentration is a proxy for neural activity, out of the three classes of indicators, Ca^{2+} indicators have so far been the most widely used due to their finely tuned properties that have been refined by well over a decade of directed evolution and protein engineering. These efforts have produced Ca^{2+} indicators with very large fluorescence responses and correspondingly high signal to noise ratios that are suitable for *in vivo* imaging. Indicators for membrane potential have lagged far behind Ca^{2+} indicators in terms of utility and real-world application. However, they hold the promise of providing a direct measure of neural

activity that could be used to unravel neuronal signaling dynamics with millisecond temporal resolution.

6.1 Summary of the thesis

The current repertoire of robust high fidelity voltage indicators includes green FP-based (*14*, *15*) and far-red Arch-based (*190*) voltage indicators. Despite these recent developments, voltage indicators with bright red-shifted fluorescence are still in great demand by neuroscientists. In Chapter 2 we reported the successful development of a bright FP-based red voltage indicator, FlicR1, with properties that are comparable to the best available green indicators. FlicR1 faithfully reported single action potentials (~3% $\Delta F/F$) and tracked electrically driven voltage oscillations at 100 Hz in hippocampal neurons in single trial recordings. Moreover, FlicR1 could be easily imaged with widefield fluorescence microscopy. We also demonstrated that FlicR1 can be used in conjunction with a blue-shifted channelrhodopsin for all-optical electrophysiology, although some precautions for photoactivation need to be considered. FlicR1 is the first example of an FP-based voltage indicator with a red-shifted excitation spectrum and enough sensitivity to detect optically driven single action potentials.

During our development of FlicR1, crystal structures of the voltage sensitive domain used in FlicR1 (and other recent voltage indicators) revealed that it forms a homodimer (*199*). This finding prompted us to design voltage indicators based on a tandem dimer topology where a

161

cpFP would link both voltage sensitive domains. In Chapter 3 we described the development of a red voltage indicator based on a tandem dimer VSD design (tdFlicR Δ110AR). Using widefield fluorescence imaging, tdFlicR Δ110AR was able to report spontaneous activity in cultured neurons and showed comparable voltage sensitivity to FlicR1 in HeLa cell ITV tests. We also report a ratiometric green/red voltage indicator based on a tandem dimer VSD design (tdFlicR-VK-ASAP). Upon membrane depolarization, tdFlicR-VK-ASAP green fluorescence decreases and red fluorescence increases. It was able to report 100 mV membrane potential fluctuations in HEK cells with a ratiometric fluorescence change of ~25% ΔR/R. Unfortunately, tdFlicR-VK-ASAP was unable to report ratiometric changes for spontaneous activity in neurons using widefield fluorescence imaging.

With the engineering of FlicR1, the toolbox of voltage indicators now provides some choice with respect to indicator colour. However, the current toolbox does not include tools that enable optical highlighting of specific cells for repetitive imaging over long periods of time. In Chapter 4, we described the engineering of FlicGR0.7, which is the first example of a highlightable voltage indicator. FlicGR0.7 can be photoconverted from green to red fluorescent using blue light illumination. Both the green and red fluorescent forms of FlicGR0.7 were sensitive to membrane potential changes in mammalian cells. Unfortunately, as with our tandem dimer

designs, it was unable to report fast events in neurons using widefield imaging.

In addition to membrane potential measurements, indicators for specific neurotransmitters would be highly useful for attributing neural activity or inhibition to the release of a specific neurotransmitter. Indicators for the major excitatory neurotransmitter, glutamate, have been successfully engineered (*16*, *17*, *123*). Although GABA is the main inhibitory neurotransmitter, no genetically encoded indicator is available for it. In Chapter 5, we described the development of a green FP-based GABA indicator; GABA-G1. Upon binding to GABA, GABA-G1 decreased in green fluorescence. Through rational design and directed protein evolution we engineered GABA-G1 to have a 1-fold dynamic range *in vitro*. Although we attempted several strategies to express GABA-G1 on the surface of mammalian cells, it remained trapped in the endoplasmic reticulum. The insurmountable roadblock of poor membrane trafficking in mammalian cells was an unforeseeable, and unpredictable, shortcoming of GABA-G1.

6.2 Perspective and Future directions

In this thesis, we expanded the current repertoire of available voltage indicators by using protein engineering and directed evolution approaches. Despite this progress, further improvements are still needed to evolve them into robust voltage indicators that are suitable for *in vivo* imaging. Specifically, there are two main issues with FlicR and its tandem dimer

163

variants. The first issue is that a fraction of the protein forms intracellular protein aggregates in neuronal cells. The disadvantages of this are two-fold: First, these puncta represent a large pool of protein that does not contribute to the voltage sensitive response, and thus dilutes the fluorescence response of membrane bound functional indicator molecules. Second, it limits the use of the indicators *in vivo* because protein aggregation would likely be toxic to a transgenic animal expressing FlicR1. From our work with the tandem dimer green/red voltage indicators, we observed that only the red channel showed intracellular puncta in neurons and therefore we hypothesize that the cause of these puncta is the remarkable stability of the mApple FP barrel.

The second issue for FlicR variants is the photoactivation of their chromophore with blue light. We were unable to shine high intensities of blue light on FlicR1 and had to resort to spectrally isolating optogenetic excitation light to different parts of a neuron in all-optical electrophysiology experiments. In neurons co-expressing FlicR1 and a blue-light excitable channelrhodopsin, blue light was spatially targeted to neuronal processes while avoiding the soma. The whole cell was then illuminated with yellow light and collected FlicR1 fluorescence only from the soma to image neuronal activity.

Both of these phenomena, aggregation and photoactivation, seem to be ultimately attributable to the Anthozoa-derived mApple FP barrel used in FlicR variants, because related Anthozoa-derived FPs behave similarly

(*78*). Elimination of the aggregation and photoactivation of FlicR variants would make them more robust red voltage indicators suitable for use *in vivo*. One avenue to pursue is swapping out the mApple FP barrel with alternative red FP barrels like mKate (*241*) and its variants (*242, 243*) from the sea anemone *Entacmaea quadricolor*.

Our attempts to engineer a highlightable voltage indicator resulted in FlicGR0.7. Although it serves as a functional prototype, it was unable to report fast events in neurons. Further directed evolution and exploration of different FP barrels would probably lead to improved variants with brighter fluorescence enabling them to report neural activity with short exposure times necessary for fast imaging. In addition, we tested FlicGR0.7 (and other constructs based on photoconvertible FPs) as possible voltage integrators. However, we were unable to generate a successful prototype using our current screening approach. A more streamlined and higher throughput mammalian screen would certainly be helpful in future efforts to generate a voltage integrator and improved voltage indicators.

Protein engineering of genetically encoded indicators for live cell imaging is a challenging endeavour due to limited information on the behaviour of protein domains in mammalian cells. Our development of an FP-based GABA indicator dramatically illustrates this point. Our substantial efforts ultimately resulted in a construct that is adequate for detecting GABA *in vitro*, but when expressed in cells it did not properly traffic to the plasma membrane. Future efforts to engineer GABA

165

indicators might explore different, less selective GABA binding domains like Atu2422 (*244*) or engineer the GABA binding pocket into homologous PBPs that are known to properly traffic in mammalian cells. An alternative approach would be to use a GABA sensitive G-protein coupled receptor as the GABA sensitive domain.

Bibliography

1. S. Herculano-Houzel, The remarkable, yet not extraordinary, human brain as a scaled-up primate brain and its associated cost. *Proc. Natl. Acad. Sci. USA*. **109 Suppl**, 10661–10668 (2012).

2. B. Pesaran, M. J. Nelson, R. A. Andersen, Free choice activates a decision circuit between frontal and parietal cortex. *Nature*. **453**, 406–409 (2008).

3. M. R. Cohen, J. H. R. Maunsell, Attention improves performance primarily by reducing interneuronal correlations. *Nat. Neurosci.* **12**, 1594–1600 (2009).

4. H. V. Davila, B. M. Salzberg, L. B. Cohen, A. S. Waggoner, A large change in axon fluorescence that provides a promising method for measuring membrane potential. *Nat. New Biol.* **241**, 159–160 (1973).

5. J. E. Brown *et al.*, Rapid changes in intracellular free calcium concentration. Detection by metallochromic indicator dyes in squid giant axon. *Biophys. J.* **15**, 1155–1160 (1975).

6. R. Y. Tsien, New calcium indicators and buffers with high selectivity against magnesium and protons: design, synthesis, and properties of prototype structures. *Biochemistry*. **19**, 2396–2404 (1980).

7. V. I. Chefer, A. C. Thompson, A. Zapata, T. S. Shippenberg, Overview of Brain Microdialysis. *Curr. Protoc. Neurosci.*, 1–35 (2009).

8. R. G. Ding, H. Asada, K. Obata, Changes in extracellular glutamate and GABA levels in the hippocampal Ca3 and Ca1 areas and the induction of glutamic acid decarboxylase-67 in dentate granule cells of rats treated with kainic acid. *Brain Res.* **800**, 105–113 (1998).

9. T. Falkenberg *et al.*, GABA release and GAD67 mRNA expression in rat hippocampus following entorhinal cortex activation. *Mol. Brain Res.*, 413–416 (1997).

10. H. Benveniste, J. Drejer, A. Schousboe, N. H. Diemer, Elevation of the extracellular concentrations of glutamate and aspartate in rat hippocampus during transient cerebral ischemia monitored by intracerebral microdialysis. *J. Neurochem.* **43**, 1369–1374 (1984).

11. T. Nagai, A. Sawano, E. S. Park, A. Miyawaki, Circularly permuted green fluorescent proteins engineered to sense Ca2+. *Proc. Natl. Acad. Sci. USA*. **98**, 3197–3202 (2001).

12. A. Miyawaki *et al.*, Fluorescent indicators for Ca2+ based on green fluorescent proteins and calmodulin. *Nature*. **388**, 882–887 (1997).

13. J. Nakai, M. Ohkura, K. Imoto, A high signal-to-noise Ca(2+) probe composed of a single green fluorescent protein. *Nat. Biotechnol.* **19**, 137–141 (2001).

14. L. Jin *et al.*, Single action potentials and subthreshold electrical events imaged in neurons with a fluorescent protein voltage probe. *Neuron*. **75**, 779–785 (2012).

15. F. St-Pierre *et al.*, High-fidelity optical reporting of neuronal electrical activity with an ultrafast fluorescent voltage sensor. *Nat. Neurosci.* **17**, 884–889 (2014).

16. J. S. Marvin *et al.*, An optimized fluorescent probe for visualizing glutamate neurotransmission. *Nat. Methods*. **10**, 162–170 (2013).

17. S. Okumoto *et al.*, Detection of glutamate release from neurons by genetically encoded surface-displayed FRET nanosensors. *Proc. Natl. Acad. Sci. U. S. A.* **102**, 8740–5 (2005).

18. O. Shimomura, F. H. Johnson, Y. Saiga, Extraction, Purification and Properties of Aequorin, a Bioluminescent Protein from the Luminous

Hydromedusan,Aequorea. *J. Cell. Comp. Physiol.* **59**, 223–239 (1962).

19. D. C. Prasher, V. K. Eckenrode, W. W. Ward, F. G. Prendergast, M. J. Cormier, Primary structure of the Aequorea victoria green-fluorescent protein. *Gene.* **111**, 229–233 (1992).

20. M. Chalfie, Y. Tu, G. Euskirchen, W. W. Ward, D. C. Prasher, Green fluorescent protein as a marker for gene expression. *Science.* **263**, 802–805 (1994).

21. R. Heim, D. C. Prasher, R. Y. Tsien, Wavelength mutations and posttranslational autoxidation of green fluorescent protein. *Proc. Natl. Acad. Sci.* **91**, 12501–12504 (1994).

22. M. V. Matz *et al.*, Fluorescent proteins from nonbioluminescent Anthozoa species. *Nat. Biotechnol.* **17**, 969–973 (1999).

23. T. D. Craggs, Green fluorescent protein: structure, folding and chromophore maturation. *Chem. Soc. Rev.* **38**, 2865–75 (2009).

24. R. Y. Tsien, The green fluorescent protein. *Annu. Rev. Biochem.* **67**, 509–544 (1998).

25. S. Delagrave, R. E. Hawtin, C. M. Silva, M. M. Yang, D. C. Youvan, Red-shifted excitation mutants of the green fluorescent protein. *Biotechnology. (N. Y).* **13**, 151–154 (1995).

26. F. Sievers *et al.*, Fast, scalable generation of high-quality protein multiple sequence alignments using Clustal Omega. *Mol. Syst. Biol.* **7**, 539 (2011).

27. M. Goujon *et al.*, A new bioinformatics analysis tools framework at EMBL-EBI. *Nucleic Acids Res.* **38**, W695–W699 (2010).

28. M. Ormö *et al.*, Crystal structure of the Aequorea victoria green fluorescent protein. *Science.* **273**, 1392–1395 (1996).

29. F. Yang, L. G. Moss, G. N. Phillips Jr., The molecular structure of green fluorescent protein. *Nat. Biotechnol.* **14**, 1246–1251 (1996).

30. D. Yarbrough, R. M. Wachter, K. Kallio, M. V. Matz, S. J. Remington, Refined crystal structure of DsRed, a red fluorescent protein from coral, at 2.0-A resolution. *Proc. Natl. Acad. Sci. U. S. A.* **98**, 462–467 (2001).

31. L. Schrödinger, The PyMOL Molecular Graphics System, Version 1.3 r1; Schrödinger, LLC: New York, 2010.

32. V. V. Verkhusha, K. A. Lukyanov, The molecular properties and applications of Anthozoa fluorescent proteins and chromoproteins. *Nat. Biotechnol.* **22**, 289–96 (2004).

33. N. C. Shaner, P. A. Steinbach, R. Y. Tsien, A guide to choosing fluorescent proteins. *Nat. Methods.* **2**, 905–909 (2005).

34. D. M. Chudakov, S. Lukyanov, K. A. Lukyanov, Fluorescent proteins as a toolkit for in vivo imaging. *Trends Biotechnol.* **23**, 605–613 (2005).

35. B. R. Branchini, A. R. Nemser, M. Zimmer, A computational analysis of the unique protein-induced tight turn that results in posttranslational chromophore formation in green fluorescent protein. *J. Am. Chem. Soc.* **120**, 1–6 (1998).

36. A. Miyawaki, T. Nagai, H. Mizuno, Mechanisms of protein fluorophore formation and engineering. *Curr. Opin. Chem. Biol.* **7**, 557–562 (2003).

37. A. B. Cubitt *et al.*, Understanding, improving and using green fluorescent proteins. *Trends Biochem. Sci.* **20**, 448–55 (1995).

38. D. P. Barondeau, J. A. Tainer, E. D. Getzoff, Structural evidence for an enolate intermediate in GFP fluorophore biosynthesis. *J. Am. Chem. Soc.* **128**, 3166–3168 (2006).

39. L. Zhang, H. N. Patel, J. W. Lappe, R. M. Wachter, Reaction progress of chromophore biogenesis in green fluorescent protein. *J. Am. Chem. Soc.* **128**, 4766–4772 (2006).

40. M. A. Rosenow, H. A. Huffman, M. E. Phail, R. M. Wachter, The Crystal Structure of the Y66L Variant of Green Fluorescent Protein Supports a Cyclization-Oxidation-Dehydration Mechanism for Chromophore Maturation. *Biochemistry*. **43**, 4464–4472 (2004).

41. M. A. Rosenow, H. N. Patel, R. M. Wachter, Oxidative chemistry in the GFP active site leads to covalent cross-linking of a modified leucine side chain with a histidine imidazole: Implications for the mechanism of chromophore formation. *Biochemistry*. **44**, 8303–8311 (2005).

42. R. L. Strack, D. E. Strongin, L. Mets, B. S. Glick, R. J. Keenan, Chromophore formation in DsRed occurs by a branched pathway. *J. Am. Chem. Soc.* **132**, 8496–8505 (2010).

43. L. J. Pouwels, L. Zhang, N. H. Chan, P. C. Dorrestein, R. M. Wachter, Kinetic Isotope Effect Studies on the de Novo Rate of Chromophore Formation in Slow-maturing GFP Variants. *Biochemistry*, 10111–10122 (2008).

44. D. P. Barondeau, C. D. Putnam, C. J. Kassmann, J. A. Tainer, E. D. Getzoff, Mechanism and energetics of green fluorescent protein chromophore synthesis revealed by trapped intermediate structures. *Proc. Natl. Acad. Sci. U. S. A.* **100**, 12111–12116 (2003).

45. G. S. Baird, D. A. Zacharias, R. Y. Tsien, Biochemistry, mutagenesis, and oligomerization of DsRed, a red fluorescent protein from coral. *Proc. Natl. Acad. Sci. U. S. A.* **97**, 11984–9 (2000).

46. A. A. Pakhomov, V. I. Martynov, GFP Family: Structural Insights into Spectral Tuning. *Chem. Biol.* **15**, 755–764 (2008).

47. S. J. Remington, Fluorescent proteins: maturation, photochemistry and photophysics. *Curr. Opin. Struct. Biol.* **16**, 714–721 (2006).

48. V. V. Verkhusha, D. M. Chudakov, N. G. Gurskaya, S. Lukyanov, K. A. Lukyanov, Common Pathway for the Red Chromophore Formation in Fluorescent Proteins and Chromoproteins. *Chem. Biol.* **11**, 845–854 (2004).

49. S. Pletnev, F. V. Subach, Z. Dauter, A. Wlodawer, V. V. Verkhusha, Understanding blue-to-red conversion in monomeric fluorescent timers and hydrolytic degradation of their chromophores. *J. Am. Chem. Soc.* **132**, 2243–2253 (2010).

50. H. Mizuno *et al.*, Photo-induced peptide cleavage in the green-to-red conversion of a fluorescent protein. *Mol. Cell.* **12**, 1051–1058 (2003).

51. R. Ando, H. Hama, M. Yamamoto-Hino, H. Mizuno, A. Miyawaki, An optical marker based on the UV-induced green-to-red photoconversion of a fluorescent protein. *Proc. Natl. Acad. Sci. U. S. A.* **99**, 12651–12656 (2002).

52. J. Wiedenmann *et al.*, EosFP, a fluorescent marker protein with UV-inducible green-to-red fluorescence conversion. *Proc. Natl. Acad. Sci. U. S. A.* **101**, 15905–15910 (2004).

53. A. A. Pakhomov, N. Y. Martynova, N. G. Gurskaya, T. A. Balashova, V. I. Martynov, Photoconversion of the chromophore of a fluorescent protein from Dendronephthya sp. *Biochem.* **69**, 901–908 (2004).

54. Y. A. Labas *et al.*, Diversity and evolution of the green fluorescent protein family. *Proc. Natl. Acad. Sci. U. S. A.* **99**, 4256–61 (2002).

55. R. Heim, A. B. Cubitt, R. Y. Tsien, Improved green fluorescence. *Nature.* **373**, 663–664 (1995).

56. K. Brejc *et al.*, Structural basis for dual excitation and

photoisomerization of the Aequorea victoria green fluorescent protein. *Proc. Natl. Acad. Sci. U. S. A.* **94**, 2306–2311 (1997).

57. X. Shu *et al.*, Ultrafast excited-state dynamics in the green fluorescent protein variant S65T/H148D. 1. Mutagenesis and structural studies. *Biochemistry*. **46**, 12005–12013 (2007).

58. W. Tomosugi *et al.*, An ultramarine fluorescent protein with increased photostability and pH insensitivity. *Nat. Methods*. **6**, 351–353 (2009).

59. H. W. Ai, N. C. Shaner, Z. Cheng, R. Y. Tsien, R. E. Campbell, Exploration of new chromophore structures leads to the identification of improved blue fluorescent proteins. *Biochemistry*. **46**, 5904–5910 (2007).

60. M. A. Rizzo, G. H. Springer, B. Granada, D. W. Piston, An improved cyan fluorescent protein variant useful for FRET. *Nat. Biotechnol.* **22**, 445–449 (2004).

61. A. W. Nguyen, P. S. Daugherty, Evolutionary optimization of fluorescent proteins for intracellular FRET. *Nat. Biotechnol.* **23**, 355–360 (2005).

62. N. C. Shaner *et al.*, Improved monomeric red, orange and yellow fluorescent proteins derived from Discosoma sp. red fluorescent protein. *Nat. Biotechnol.* **22**, 1567–72 (2004).

63. H. Tsutsui, S. Karasawa, H. Shimizu, N. Nukina, A. Miyawaki, Semi-rational engineering of a coral fluorescent protein into an efficient highlighter. *EMBO Rep.* **6**, 233–238 (2005).

64. B. P. Cormack, R. H. Valdivia, S. Falkow, FACS-optimized mutants of the green fluorescent protein (GFP). *Gene*. **173**, 33–38 (1996).

65. T. T. Yang, L. Cheng, S. R. Kain, Optimized codon usage and chromophore mutations provide enhanced sensitivity with the green

fluorescent protein. *Nucleic Acids Res.* **24**, 4592–4593 (1996).

66.   S. Jakobs, V. Subramaniam, A. Schonle, T. M. Jovin, S. W. Hell, EFGP and DsRed expressing cultures of *Escherichia coli* imaged by confocal, two-photon and fluorescence lifetime microscopy. *FEBS Lett*. **479**, 131–135 (2000).

67.   B. J. Bevis, B. S. Glick, Rapidly maturing variants of the Discosoma red fluorescent protein (DsRed). *Nat. Biotechnol.* **20**, 83–87 (2002).

68.   A. T. Pandelieva *et al.*, Brighter Red Fluorescent Proteins by Rational Design of Triple-Decker Motif. *ACS Chem. Biol.* **11**, 508–517 (2016).

69.   R. A. Chica, M. M. Moore, B. D. Allen, S. L. Mayo, Generation of longer emission wavelength red fluorescent proteins using computationally designed libraries. *Proc. Natl. Acad. Sci. U. S. A.* **107**, 20257–62 (2010).

70.   D. A. Zacharias, J. D. Violin, A. C. Newton, R. Y. Tsien, Partitioning of lipid-modified monomeric GFPs into membrane microdomains of live cells. *Science*. **296**, 913–6 (2002).

71.   W. Zeng *et al.*, Resonance energy transfer between green fluorescent protein variants: Complexities revealed with myosin fusion proteins. *Biochemistry*. **45**, 10482–10491 (2006).

72.   G. N. Phillips, Structure and dynamics of green fluorescent protein. *Curr. Opin. Struct. Biol.* **7**, 821–827 (1997).

73.   L. A. Gross, G. S. Baird, R. C. Hoffman, K. K. Baldridge, R. Y. Tsien, The structure of the chromophore within DsRed, a red fluorescent protein from coral. *Proc. Natl. Acad. Sci.* **97**, 11990–11995 (2000).

74.   J. Wiehler, J. Von Hummel, B. Steipe, Mutants of Discosoma red fluorescent protein with a GFP-like chromophore. *FEBS Lett.* **487**,

384–389 (2001).

75. M. A. Wall, M. Socolich, R. Ranganathan, The structural basis for red fluorescence in the tetrameric GFP homolog DsRed. *Nat. Struct. Biol.* **7**, 1133–1138 (2000).

76. R. E. Campbell *et al.*, A monomeric red fluorescent protein. *Proc. Natl. Acad. Sci. U. S. A.* **99**, 7877–82 (2002).

77. H. Ai, J. N. Henderson, S. J. Remington, R. E. Campbell, Directed evolution of a monomeric, bright and photostable version of Clavularia cyan fluorescent protein: structural characterization and applications in fluorescence imaging. *Biochem. J.* **400**, 531–40 (2006).

78. D. Cai, K. B. Cohen, T. Luo, J. W. Lichtman, J. R. Sanes, Improved tools for the Brainbow toolbox. *Nat. Methods.* **10**, 540–547 (2013).

79. J. Livet *et al.*, Transgenic strategies for combinatorial expression of fluorescent proteins in the nervous system. *Nature.* **450**, 56–62 (2007).

80. C. S. Branda, S. M. Dymecki, Talking about a revolution: The impact of site-specific recombinases on genetic analyses in mice. *Dev. Cell.* **6**, 7–28 (2004).

81. R. D. Palmiter, R. L. Brinster, Germ-line transformation of mice. *Annu. Rev. Genet.* **20**, 465–99 (1986).

82. I. Tabansky *et al.*, Developmental bias in cleavage-stage mouse blastomeres. *Curr. Biol.* **23**, 21–31 (2013).

83. S. Hampel *et al.*, Drosophila Brainbow: a recombinase-based fluorescence labeling technique to subdivide neural expression patterns. *Nat. Methods.* **8**, 253–9 (2011).

84. K. Red-Horse, H. Ueno, I. L. Weissman, M. A. Krasnow, Coronary arteries form by developmental reprogramming of venous cells.

Nature. **464**, 549–553 (2010).

85. J. A. Lehoczky, B. Robert, C. J. Tabin, Mouse digit tip regeneration is mediated by fate-restricted progenitor cells. *Proc. Natl. Acad. Sci.* **108**, 20609–20614 (2011).

86. H. J. Snippert *et al.*, Intestinal crypt homeostasis results from neutral competition between symmetrically dividing Lgr5 stem cells. *Cell*. **143**, 134–144 (2010).

87. A. G. Schepers *et al.*, Lineage tracing reveals Lgr5+ stem cell activity in mouse intestinal adenomas. *Science*. **337**, 730–5 (2012).

88. Y. A. Pan *et al.*, Zebrabow: multispectral cell labeling for cell tracing and lineage analysis in zebrafish. *Development*. **140**, 2835–46 (2013).

89. D. Hadjieconomou *et al.*, Flybow: genetic multicolor cell labeling for neural circuit analysis in Drosophila melanogaster. *Nat Methods*. **8**, 260–266 (2011).

90. V. Gupta, K. D. Poss, Clonally dominant cardiomyocytes direct heart morphogenesis. *Nature*. **484**, 479–84 (2012).

91. M. Mavrakis, R. Rikhy, J. Lippincott-Schwartz, Plasma Membrane Polarity and Compartmentalization Are Established before Cellularization in the Fly Embryo. *Dev. Cell*. **16**, 93–104 (2009).

92. K.-M. Leung *et al.*, Asymmetrical beta-actin mRNA translation in growth cones mediates attractive turning to netrin-1. *Nat. Neurosci.* **9**, 1247–56 (2006).

93. S. A. Wacker, F. Oswald, J. Wiedenmann, W. Knöchel, A green to red photoconvertible protein as an analyzing tool for early vertebrate development. *Dev. Dyn.* **236**, 473–480 (2007).

94. G. Çolakoğlu, A. Brown, Intermediate filaments exchange subunits along their length and elongate by end-to-end annealing. *J. Cell*

Biol. **185**, 769–777 (2009).

95. D. Chen *et al.*, Multiple pathways differentially regulate global oxidative stress responses in fission yeast. *Mol. Biol. Cell*. **19**, 308–317 (2008).

96. D. W. Hailey, J. Lippincott-Schwartz, in *Methods in Enzymology* (Elsevier Inc., ed. 1, 2009), vol. 452, pp. 25–45.

97. N. M. Christensen, C. Faulkner, K. Oparka, Evidence for unidirectional flow through plasmodesmata. *Plant Physiol.* **150**, 96–104 (2009).

98. P. K. Kim, R. T. Mullen, U. Schumann, J. Lippincott-Schwartz, The origin and maintenance of mammalian peroxisomes involves a de novo PEX16-dependent pathway from the ER. *J. Cell Biol.* **173**, 521–532 (2006).

99. G. H. Patterson *et al.*, A photoactivatable GFP for selective photolabeling of proteins and cells. *Science*. **297**, 1873–1877 (2002).

100. B. Schmierer, C. S. Hill, Kinetic Analysis of Smad Nucleocytoplasmic Shuttling Reveals a Mechanism for Transforming Growth Factor β-Dependent Nuclear Accumulation of Smads. *Mol. Cell. Biol.* **25**, 9845–9858 (2005).

101. S. Deryusheva, J. G. Gall, Dynamics of coilin in Cajal bodies of the Xenopus germinal vesicle. *Proc. Natl. Acad. Sci. U. S. A*. **101**, 4810–4 (2004).

102. T. Bergeland, L. Haugen, O. J. B. Landsverk, H. Stenmark, O. Bakke, Cell-cycle-dependent binding kinetics for the early endosomal tethering factor EEA1. *EMBO Rep.* **9**, 171–178 (2008).

103. A. Egner *et al.*, Fluorescence nanoscopy in whole cells by asynchronous localization of photoswitching emitters. *Biophys. J.*

93, 3285–3290 (2007).

104. E. Betzig *et al.*, Imaging intracellular fluorescent proteins at nanometer resolution. *Science*. **313**, 1642–1645 (2006).

105. S. T. Hess, T. P. K. Girirajan, M. D. Mason, Ultra-high resolution imaging by fluorescence photoactivation localization microscopy. *Biophys. J.* **91**, 4258–72 (2006).

106. R. Heim, R. Y. Tsien, Engineering green fluorescent protein for improved brightness, longer wavelengths and fluorescence resonance energy transfer. *Curr. Biol.* **6**, 178–182 (1996).

107. T. Förster, Transfer Mechanisms of Electronic Excitation. *Discuss. Faraday Soc.*, 7–17 (1959).

108. B. Valeur, in *Molecular Fluorescence: Principles and Applications* (Wiley-VCH Verlag GmbH, ed. 1, 2001), vol. 8, pp. 113–122.

109. H. Ai, K. L. Hazelwood, M. W. Davidson, R. E. Campbell, Fluorescent protein FRET pairs for ratiometric imaging of dual biosensors. *Nat. Methods*. **5**, 401–403 (2008).

110. H. Kawai *et al.*, Simultaneous real-time detection of initiator- and effector-caspase activation by double fluorescence resonance energy transfer analysis. *J. Pharmacol. Sci.* **97**, 361–368 (2005).

111. R. A. Figueroa *et al.*, Anchored FRET sensors detect local caspase activation prior to neuronal degeneration. *Mol. Neurodegener.* **6**, 35 (2011).

112. K. Kominami *et al.*, In Vivo Imaging of Hierarchical Spatiotemporal Activation of Caspase-8 during Apoptosis. *PLoS One*. **7**, e50218 (2012).

113. R. Sabariegos *et al.*, Fluorescence resonance energy transfer-based assay for characterization of hepatitis C virus NS3-4A protease activity in live cells. *Antimicrob. Agents Chemother.* **53**,

728–734 (2009).

114. Y. C. Hwang, J. J. H. Chu, P. L. Yang, W. Chen, M. V. Yates, Rapid identification of inhibitors that interfere with poliovirus replication using a cell-based assay. *Antiviral Res.* **77**, 232–236 (2008).

115. M. T. Tsai *et al.*, Real-time monitoring of human enterovirus (HEV)-infected cells and anti-HEV 3C protease potency by fluorescence resonance energy transfer. *Antimicrob. Agents Chemother.* **53**, 748–755 (2009).

116. A. Miyawaki, O. Griesbeck, R. Heim, R. Y. Tsien, Dynamic and quantitative Ca2+ measurements using improved cameleons. *Proc. Natl. Acad. Sci. U. S. A.* **96**, 2135–2140 (1999).

117. A. E. Palmer *et al.*, Ca2+ Indicators Based on Computationally Redesigned Calmodulin-Peptide Pairs. *Chem. Biol.* **13**, 521–530 (2006).

118. K. Truong *et al.*, FRET-based in vivo Ca2+ imaging by a new calmodulin-GFP fusion molecule. *Nat. Struct. Biol.* **8**, 1069–1073 (2001).

119. V. A. Romoser, P. M. Hinkle, A. Persechini, Detection in living cells of Ca2+-dependent changes in the fluorescence emission of an indicator composed of two green fluorescent protein variants linked by a calmodulin-binding sequence. *Biochemistry*. **272**, 13270–13274 (1997).

120. H. Takanaga, B. Chaudhuri, W. B. Frommer, GLUT1 and GLUT9 as major contributors to glucose influx in HepG2 cells identified by a high sensitivity intramolecular FRET glucose sensor. *Biochim. Biophys. Acta - Biomembr.* **1778**, 1091–1099 (2008).

121. J. S. Ha *et al.*, Design and application of highly responsive fluorescence resonance energy transfer biosensors for detection of

sugar in living Saccharomyces cerevisiae cells. *Appl. Environ. Microbiol.* **73**, 7408–7414 (2007).

122. J. S. Marvin, E. R. Schreiter, I. M. Echevarría, L. L. Looger, A genetically encoded, high-signal-to-noise maltose sensor. *Proteins Struct. Funct. Bioinforma.* **79**, 3025–3036 (2011).

123. S. A. Hires, Y. Zhu, R. Y. Tsien, Optical measurement of synaptic glutamate spillover and reuptake by linker optimized glutamate-sensitive fluorescent reporters. *Proc. Natl. Acad. Sci. U. S. A.* **105**, 4411–4416 (2008).

124. P. J. Dittmer, J. G. Miranda, J. A. Gorski, A. E. Palmer, Genetically encoded sensors to elucidate spatial distribution of cellular zinc. *J. Biol. Chem.* **284**, 16289–16297 (2009).

125. P. Vincent, N. Gervasi, J. Zhang, Real-time monitoring of cyclic nucleotide signaling in neurons using genetically encoded FRET probes. *Brain Cell Biol.* **36**, 3–17 (2008).

126. J. Zhang, C. J. Hupfeld, S. S. Taylor, J. M. Olefsky, R. Y. Tsien, Insulin disrupts beta-adrenergic signalling to protein kinase A in adipocytes. *Nature.* **437**, 569–573 (2005).

127. M. T. Kunkel, Q. Ni, R. Y. Tsien, J. Zhang, A. C. Newton, Spatio-temporal dynamics of protein kinase B/Akt signaling revealed by a genetically encoded fluorescent reporter. *J. Biol. Chem.* **280**, 5581–5587 (2005).

128. M. D. Allen, J. Zhang, Subcellular dynamics of protein kinase A activity visualized by FRET-based reporters. *Biochem. Biophys. Res. Commun.* **348**, 716–721 (2006).

129. J. Zhang, Y. Ma, S. S. Taylor, R. Y. Tsien, Genetically encoded reporters of protein kinase A activity reveal impact of substrate tethering. *Proc. Natl. Acad. Sci. U. S. A.* **98**, 14997–15002 (2001).

130. Y. Wang *et al.*, Visualizing the mechanical activation of Src. *Nature.* **434**, 1040–5 (2005).

131. C. D. Hu, Y. Chinenov, T. K. Kerppola, Visualization of interactions among bZIP and Rel family proteins in living cells using bimolecular fluorescence complementation. *Mol. Cell*. **9**, 789–798 (2002).

132. I. Ghosh, A. D. Hamilton, L. Regan, Antiparallel leucine zipper-directed protein reassembly: Application to the green fluorescent protein [12]. *J. Am. Chem. Soc.* **122**, 5658–5659 (2000).

133. C.-D. D. Hu, T. K. Kerppola, Simultaneous visualization of multiple protein interactions in living cells using multicolor fluorescence complementation analysis. *Nat Biotechnol*. **21**, 539–545 (2003).

134. Y. Takahashi *et al.*, Loss of Bif-1 Suppresses Bax / Bak Conformational Change and Mitochondrial Apoptosis. *Mol. Cell. Biol.* **25**, 9369–9382 (2005).

135. B. Nyfeler, S. W. Michnick, H.-P. Hauri, Capturing protein interactions in the secretory pathway of living cells. *Proc. Natl. Acad. Sci. U. S. A.* **102**, 6350–6355 (2005).

136. H. N. Higgs, K. J. Peterson, Phylogenetic analysis of the formin homology 2 domain. *Mol. Biol. Cell*. **16**, 1–13 (2005).

137. H. Ye, H. J. Choi, J. Poe, T. E. Smithgall, Oligomerization is required for HIV-1 Nef-induced activation of the Src family protein-tyrosine kinase, Hck. *Biochemistry*. **43**, 15775–15784 (2004).

138. D. Fang, T. K. Kerppola, Ubiquitin-mediated fluorescence complementation reveals that Jun ubiquitinated by Itch/AIP4 is localized to lysosomes. *Proc. Natl. Acad. Sci. U. S. A*. **101**, 14782–7 (2004).

139. P. De Bie *et al.*, Characterization of COMMD protein–protein interactions in NF-κB signalling. *Biochem. J.* **398**, 63–71 (2006).

140. M. De Virgilio, W. B. Kiosses, S. J. Shattil, Proximal, selective, and dynamic interactions between integrin αIIbβ3 and protein tyrosine kinases in living cells. *J. Cell Biol.* **165**, 305–311 (2004).

141. D. Adolph, N. Flach, K. Mueller, D. H. Ostareck, A. Ostareck-Lederer, Deciphering the cross talk between hnRNP K and c-Src: the c-Src activation domain in hnRNP K is distinct from a second interaction site. *Mol. Cell. Biol.* **27**, 1758–70 (2007).

142. C. Schmidt *et al.*, Mechanisms of Proinflammatory Cytokine-Induced Biphasic NF- κB Activation. *Mol. Cell*. **12**, 1287–1300 (2003).

143. I. Remy, A. Montmarquette, S. W. Michnick, PKB/Akt modulates TGF-beta signalling through a direct interaction with Smad3. *Nat. Cell Biol.* **6**, 358–365 (2004).

144. M. L. MacDonald *et al.*, Identifying off-target effects and hidden phenotypes of drugs in human cells. *Nat. Chem. Biol.* **2**, 329–337 (2006).

145. Z. Ding *et al.*, A retrovirus-based protein complementation assay screen reveals functional AKT1-binding partners. *Proc. Natl. Acad. Sci. U. S. A.* **103**, 15014–15019 (2006).

146. I. Remy, S. W. Michnick, Regulation of apoptosis by the Ft1 protein , a new modulator of protein kinase B/Akt. *Mol. Cell. Biol.* **24**, 1493–1504 (2004).

147. C. G. M. Wilson, T. J. Magliery, L. Regan, Detecting protein-protein interactions with GFP-fragment reassembly. *Nat. Methods*. **1**, 255–262 (2004).

148. S. C. Alford, A. S. Abdelfattah, Y. Ding, R. E. Campbell, A fluorogenic red fluorescent protein heterodimer. *Chem. Biol.* **19**, 353–360 (2012).

149. S. C. Alford, Y. Ding, T. Simmen, R. E. Campbell, Dimerization-dependent green and yellow fluorescent proteins. *ACS Synth. Biol.* **1**, 569–575 (2012).

150. Y. Ding *et al.*, Ratiometric biosensors based on dimerization-dependent fluorescent protein exchange. *Nat. Methods*. **12**, 195–198 (2015).

151. M. Kneen, J. Farinas, Y. Li, A. S. Verkman, Green fluorescent protein as a noninvasive intracellular pH indicator. *Biophys. J.* **74**, 1591–9 (1998).

152. R. M. Wachter, S. J. Remington, Sensitivity of the yellow variant of green fluorescent protein to halides and nitrate. *Curr. Biol.* **9**, 628–629 (1999).

153. Y. Shen, M. Rosendale, R. E. Campbell, D. Perrais, pHuji, a pH-sensitive red fluorescent protein for imaging of exo- and endocytosis. *J. Cell Biol.* **207**, 419–432 (2014).

154. G. Miesenböck, D. a De Angelis, J. E. Rothman, Visualizing secretion and synaptic transmission with pH-sensitive green fluorescent proteins. *Nature*. **394**, 192–5 (1998).

155. J. Llopis, J. M. McCaffery, A. Miyawaki, M. G. Farquhar, R. Y. Tsien, Measurement of cytosolic, mitochondrial, and Golgi pH in single living cells with green fluorescent proteins. *Proc. Natl. Acad. Sci. U. S. A.* **95**, 6803–8 (1998).

156. B. Granseth, B. Odermatt, S. Royle, L. Lagnado, Clathrin-Mediated Endocytosis Is the Dominant Mechanism of Vesicle Retrieval at Hippocampal Synapses. *Neuron*. **51**, 773–786 (2006).

157. K. J. Rhoden, S. Cianchetta, S. Duchi, G. Romeo, Fluorescence quantitation of thyrocyte iodide accumulation with the yellow fluorescent protein variant YFP-H148Q/I152L. *Anal. Biochem.* **373**,

239–246 (2008).

158. L. J. V Galietta, P. M. Haggie, A. S. Verkman, Green fluorescent protein-based halide indicators with improved chloride and iodide affinities. *FEBS Lett.* **499**, 220–224 (2001).

159. H. Østergaard *et al.*, Shedding light on disul de bond formation: engineering a redox switch in green uorescent protein. *Embo J.* **20**, 5853–5862 (2001).

160. G. T. Hanson *et al.*, Investigating Mitochondrial Redox Potential with Redox-sensitive Green Fluorescent Protein Indicators. *J. Biol. Chem.* **279**, 13044–13053 (2004).

161. C. T. Dooley *et al.*, Imaging dynamic redox changes in mammalian cells with green fluorescent protein indicators. *J. Biol. Chem.* **279**, 22284–22293 (2004).

162. G. S. Baird, D. A. Zacharias, R. Y. Tsien, Circular permutation and receptor insertion within green fluorescent proteins. *Proc. Natl. Acad. Sci. USA.* **96**, 11241–11246 (1999).

163. J. Akerboom *et al.*, Crystal structures of the GCaMP calcium sensor reveal the mechanism of fluorescence signal change and aid rational design. *J. Biol. Chem.* **284**, 6455–6464 (2009).

164. Q. Wang, B. Shui, M. I. Kotlikoff, H. Sondermann, Structural basis for calcium sensing by GCaMP2. *Structure.* **16**, 1817–1827 (2008).

165. T.-W. Chen *et al.*, Ultrasensitive fluorescent proteins for imaging neuronal activity. *Nature.* **499**, 295–300 (2013).

166. J. Akerboom *et al.*, Optimization of a GCaMP Calcium Indicator for Neural Activity Imaging. *J. Neurosci.* **32**, 13819–13840 (2012).

167. Y. Zhao *et al.*, An expanded palette of genetically encoded Ca^{2+} indicators. *Science.* **333**, 1888–1891 (2011).

168. J. Wu *et al.*, A long Stokes shift red fluorescent Ca2+ indicator protein for two-photon and ratiometric imaging. *Nat. Commun.* **5**, 5262 (2014).

169. Y. Zhao *et al.*, Microfluidic cell sorter-aided directed evolution of a protein-based calcium ion indicator with an inverted fluorescent response. *Integr. Biol. (Camb).* **6**, 714–25 (2014).

170. J. Akerboom *et al.*, Genetically encoded calcium indicators for multi-color neural activity imaging and combination with optogenetics. *Front. Mol. Neurosci.* **6**, 2 (2013).

171. H. Dana *et al.*, Sensitive red protein calcium indicators for imaging neural activity. *Elife*. **5**, e12727 (2016).

172. V. V. Belousov *et al.*, Genetically encoded fluorescent indicator for intracellular hydrogen peroxide. *Nat. Methods*. **3**, 281–286 (2006).

173. A. Nimmerjahn, D. E. Bergles, Large-scale recording of astrocyte activity. *Curr. Opin. Neurobiol.* **32**, 95–106 (2015).

174. A. Molleman, *Patch Clamping: An Introductory Guide to Patch Clamp Electrophysiology* (John Wiley & Sons, 2003).

175. B. Sakmann, E. Neher, Patch clamp techniques for studying ionic channels in excitable membranes. *Annu. Rev. Physiol.* **46**, 455–72 (1984).

176. G. Buzsáki, Large-scale recording of neuronal ensembles. *Nat. Neurosci.* **7**, 446–51 (2004).

177. L. M. Loew, M. Canepari, D. Zecevic, Eds. (Springer, New York, 2011), pp. 13 – 23.

178. B. J. Baker *et al.*, Imaging brain activity with voltage- and calcium-sensitive dyes. *Cell. Mol. Neurobiol.* **25**, 245–82 (2005).

179. M. S. Siegel, E. Y. Isacoff, A genetically encoded optical probe of

membrane voltage. *Neuron*. **19**, 735–741 (1997).

180. K. Ataka, V. A. Pieribone, A genetically targetable fluorescent probe of channel gating with rapid kinetics. *Biophys. J.* **82**, 509–516 (2002).

181. L. Barnett, J. Platisa, M. Popovic, V. A. Pieribone, T. Hughes, A fluorescent, genetically-encoded voltage probe capable of resolving action potentials. *PLoS One*. **7**, e43454 (2012).

182. S. G. Gautam, A. Perron, H. Mutoh, T. Knöpfel, Exploration of fluorescent protein voltage probes based on circularly permuted fluorescent proteins. *Front. Neuroeng.* **2**, 14 (2009).

183. A. Lundby, H. Mutoh, D. Dimitrov, W. Akemann, T. Knöpfel, Engineering of a genetically encodable fluorescent voltage sensor exploiting fast Ci-VSP voltage-sensing movements. *PLoS One*. **3**, e2514 (2008).

184. A. Perron, H. Mutoh, T. Launey, T. Knöpfel, Red-shifted voltage-sensitive fluorescent proteins. *Chem. Biol.* **16**, 1268–1277 (2009).

185. Z. Han *et al.*, Fluorescent protein voltage probes derived from ArcLight that respond to membrane voltage changes with fast kinetics. *PLoS One*. **8**, e81295 (2013).

186. W. Akemann *et al.*, Imaging neural circuit dynamics with a voltage-sensitive fluorescent protein. *J. Neurophysiol.* **108**, 2323–2337 (2012).

187. A. J. Lam *et al.*, Improving FRET dynamic range with bright green and red fluorescent proteins. *Nat. Methods*. **9**, 1005–1012 (2012).

188. J. M. Kralj, D. R. Hochbaum, A. D. Douglass, A. E. Cohen, Electrical spiking in Escherichia coli probed with a fluorescent voltage-indicating protein. *Science*. **333**, 345–348 (2011).

189. J. M. Kralj, A. D. Douglass, D. R. Hochbaum, D. Maclaurin, A. E.

Cohen, Optical recording of action potentials in mammalian neurons using a microbial rhodopsin. *Nat. Methods*. **9**, 90–95 (2012).

190. D. R. Hochbaum *et al.*, All-optical electrophysiology in mammalian neurons using engineered microbial rhodopsins. *Nat. Methods*. **11**, 825–833 (2014).

191. Y. Gong, J. Z. Li, M. J. Schnitzer, Enhanced Archaerhodopsin Fluorescent Protein Voltage Indicators. *PLoS One*. **8**, e66959 (2013).

192. P. Zou *et al.*, Bright and fast multicoloured voltage reporters via electrochromic FRET. *Nat. Commun.* **5**, 4625 (2014).

193. Y. Gong, M. J. Wagner, J. Zhong Li, M. J. Schnitzer, Imaging neural spiking in brain tissue using FRET-opsin protein voltage sensors. *Nat. Commun.* **5**, 3674 (2014).

194. X. Shu *et al.*, Mammalian expression of infrared fluorescent proteins engineered from a bacterial phytochrome. *Science*. **324**, 804–807 (2009).

195. S. C. Alford, J. Wu, Y. Zhao, R. E. Campbell, T. Knöpfel, Optogenetic reporters. *Biol. Cell*. **105**, 14–29 (2013).

196. Y. Murata, H. Iwasaki, M. Sasaki, K. Inaba, Y. Okamura, Phosphoinositide phosphatase activity coupled to an intrinsic voltage sensor. *Nature*. **435**, 1239–1243 (2005).

197. E. G. Govorunova, O. A. Sineshchekov, H. Li, R. Janz, J. L. Spudich, Characterization of a highly efficient blue-shifted channelrhodopsin from the marine alga Platymonas subcordiformis. *J. Biol. Chem.* **288**, 29911–29922 (2013).

198. J. Wu *et al.*, Improved orange and red Ca^{2+} indicators and photophysical considerations for optogenetic applications. *ACS Chem. Neurosci.* **4**, 963–72 (2013).

199. Q. Li *et al.*, Structural mechanism of voltage-dependent gating in an isolated voltage-sensing domain. *Nat. Struct. Mol. Biol.* **21**, 244–252 (2014).

200. Z. Cheng, R. E. Campbell, Assessing the structural stability of designed beta-hairpin peptides in the cytoplasm of live cells. *Chembiochem.* **7**, 1147–50 (2006).

201. R. D. Kirkton, N. Bursac, Engineering biosynthetic excitable tissues from unexcitable cells for electrophysiological and cell therapy studies. *Nat. Commun.* **2**, 300 (2011).

202. D. Brinks, A. J. Klein, A. E. Cohen, Two-Photon Lifetime Imaging of Voltage Indicating Proteins as a Probe of Absolute Membrane Voltage. *Biophys. J.* **109**, 914–21 (2015).

203. A. De Simoni, C. B. Griesinger, F. A. Edwards, Development of rat CA1 neurones in acute versus organotypic slices: role of experience in synaptic morphology and activity. *J. Physiol.* **550**, 135–147 (2003).

204. B. Panaitescu *et al.*, Methylxanthines do not affect rhythmogenic preBötC inspiratory network activity but impair bursting of preBötC-driven motoneurons. *Neuroscience.* **255**, 158–176 (2013).

205. J. Y. Lin, M. Z. Lin, P. Steinbach, R. Y. Tsien, Characterization of engineered channelrhodopsin variants with improved properties and kinetics. *Biophys. J.* **96**, 1803–1814 (2009).

206. J. Mattis *et al.*, Principles for applying optogenetic tools derived from direct comparative analysis of microbial opsins. *Nat. Methods.* **9**, 159–72 (2012).

207. N. C. Klapoetke *et al.*, Independent optical excitation of distinct neural populations. *Nat. Methods.* **11**, 338–346 (2014).

208. A. Lewin, M. Mayer, J. Chusainow, D. Jacob, B. Appel, Viral

promoters can initiate expression of toxin genes introduced into Escherichia coli. *BMC Biotechnol.* **5**, 19 (2005).

209. R. L. Mullinax, D. T. Wong, H. A. Davis, K. A. Padgett, J. A. Sorge, in *E. coli Gene Expression Protocols*, P. E. Vaillancourt, Ed. (Humana Press, New Jersey, 2002), vol. 205, pp. 19–30.

210. K. D. McCarthy, J. de Vellis, Preparation of separate astroglial and oligodendroglial cell cultures from rat cerebral tissue. *J. Cell Biol.* **85**, 890–902 (1980).

211. G. Banker, K. Goslin, *Culturing Nerve Cells* (MIT Press, Cambridge, MA, ed. 2, 1998).

212. M. Jiang, G. Chen, High Ca2+-phosphate transfection efficiency in low-density neuronal cultures. *Nat. Protoc.* **1**, 695–700 (2006).

213. H. Katayama, A. Yamamoto, N. Mizushima, T. Yoshimori, A. Miyawaki, GFP-like proteins stably accumulate in lysosomes. *Cell Struct. Funct.* **33**, 1–12 (2008).

214. S. Chemla, F. Chavane, Voltage-sensitive dye imaging: Technique review and models. *J. Physiol. Paris*. **104**, 40–50 (2010).

215. H. Mutoh, W. Akemann, T. Knöpfel, Genetically engineered fluorescent voltage reporters. *ACS Chem. Neurosci.* **3**, 585–592 (2012).

216. F. St-Pierre, M. Chavarha, M. Z. Lin, Designs and sensing mechanisms of genetically encoded fluorescent voltage indicators. *Curr. Opin. Chem. Biol.* **27**, 31–8 (2015).

217. B. J. Baker *et al.*, Genetically encoded fluorescent sensors of membrane potential. *Brain Cell Biol.* **36**, 53–67 (2008).

218. J.-D. Pédelacq, S. Cabantous, T. Tran, T. C. Terwilliger, G. S. Waldo, Engineering and characterization of a superfolder green fluorescent protein. *Nat. Biotechnol.* **24**, 79–88 (2006).

219. A. S. Abdelfattah *et al.*, A Bright and Fast Red Fluorescent Protein Voltage Indicator That Reports Neuronal Activity in Organotypic Brain Slices. *J. Neurosci.* **36**, 2458–2472 (2016).

220. B. F. Fosque *et al.*, Neural circuits. Labeling of active neural circuits in vivo with designed calcium integrators. *Science*. **347**, 755–60 (2015).

221. H. Hoi, T. Matsuda, T. Nagai, R. E. Campbell, Highlightable Ca2+ indicators for live cell imaging. *J. Am. Chem. Soc.* **135**, 46–49 (2013).

222. F. V Subach *et al.*, Photoactivation mechanism of PAmCherry based on crystal structures of the protein in the dark and fluorescent states. *Proc. Natl. Acad. Sci. U. S. A.* **106**, 21097–21102 (2009).

223. L. Sivilotti, A. Nistri, GABA receptor mechanisms in the central nervous system. *Prog. Neurobiol.* **36**, 35–92 (1991).

224. F. M. Benes, S. Berretta, GABAergic interneurons: Implications for understanding schizophrenia and bipolar disorder. *Neuropsychopharmacol.* **25**, 1–27 (2001).

225. D. M. Treiman, GABAergic mechanisms in epilepsy. *Epilepsia*. **42**, 8–12 (2001).

226. D. F. Owens, A. R. Kriegstein, Is there more to GABA than synaptic inhibition? *Nat. Rev. Neurosci.* **3**, 715–727 (2002).

227. G. Deidda, I. F. Bozarth, L. Cancedda, Modulation of GABAergic transmission in development and neurodevelopmental disorders: investigating physiology and pathology to gain therapeutic perspectives. *Front. Cell. Neurosci.* **8**, 119 (2014).

228. K. Buck, P. Voehringer, B. Ferger, Rapid analysis of GABA and glutamate in microdialysis samples using high performance liquid chromatography and tandem mass spectrometry. *J. Neurosci.*

Methods. **182**, 78–84 (2009).

229. J. Kehr, Determination of γ-aminobutyric acid in microdialysis samples by microbore column liquid chromatography and fluorescence. *J. Chromatogr. B*. **708**, 49–54 (1998).

230. A. Masharina, L. Reymond, D. Maurel, K. Umezawa, K. Johnsson, A fluorescent sensor for GABA and synthetic GABA(B) receptor ligands. *J. Am. Chem. Soc.* **134**, 19026–34 (2012).

231. A. Keppler *et al.*, A general method for the covalent labeling of fusion proteins with small molecules in vivo. *Nat. Biotechnol.* **21**, 86–9 (2003).

232. A. Gautier *et al.*, An Engineered Protein Tag for Multiprotein Labeling in Living Cells. *Chem. Biol.* **15**, 128–136 (2008).

233. G. F. L. Ames, Bacterial Periplasmic Transport Systems: Structure, Mechanism, and Evolution. *Annu. Rev. Biochem.* **55**, 397–425 (1986).

234. F. A. Quiocho, Atomic structures of periplasmic binding proteins and the high-affinity active transport systems in bacteria. *Philos. Trans. R. Soc. Lond. B. Biol. Sci.* **326**, 341–352 (1990).

235. R. M. de Lorimier *et al.*, Construction of a fluorescent biosensor family. *Protein Sci.* **11**, 2655–2675 (2002).

236. M. A. Dwyer, H. W. Hellinga, Periplasmic binding proteins: A versatile superfamily for protein engineering. *Curr. Opin. Struct. Biol.* **14**, 495–504 (2004).

237. R. Chevrot *et al.*, GABA controls the level of quorum-sensing signal in Agrobacterium tumefaciens. *Proc. Natl. Acad. Sci. U. S. A.* **103**, 7460–4 (2006).

238. S. Planamente *et al.*, Structural basis for selective GABA binding in bacterial pathogens. *Mol. Microbiol.* **86**, 1085–99 (2012).

239. M. M. Flocco, S. L. Mowbray, Cα-based torsion angles: a simple tool to analyze protein conformational changes. *Protein Sci.* **4**, 2118–2122 (1995).

240. V. Gradinaru *et al.*, Molecular and Cellular Approaches for Diversifying and Extending Optogenetics. *Cell*. **141**, 154–165 (2010).

241. D. Shcherbo *et al.*, Bright far-red fluorescent protein for whole-body imaging. *Nat. Methods*. **4**, 741–746 (2007).

242. D. Shcherbo *et al.*, Far-red fluorescent tags for protein imaging in living tissues. *Biochem. J.* **418**, 567–574 (2009).

243. I. I. Shemiakina *et al.*, A monomeric red fluorescent protein with low cytotoxicity. *Nat. Commun.* **3**, 1204 (2012).

244. S. Planamente *et al.*, A conserved mechanism of GABA binding and antagonism is revealed by structure-function analysis of the periplasmic binding protein Atu2422 in Agrobacterium tumefaciens. *J. Biol. Chem.* **285**, 30294–30303 (2010).